Construction, Deployment and Data Analysis of the E and B EXperiment: A Cosmic Microwave Background Polarimeter

Joy Didier

Submitted in partial fulfillment of the

requirements for the degree of

Doctor of Philosophy

in the Graduate School of Arts and Sciences

COLUMBIA UNIVERSITY

2016

ABSTRACT

Construction, Deployment and Data Analysis of the E and B EXperiment: A Cosmic Microwave Background Polarimeter

by

Joy Didier

The E and B EXperiment (EBEX) is a pointed balloon-borne telescope designed to measure the polarization of the cosmic microwave background (CMB) as well as that from Galactic dust. The instrument is equipped with a 1.5 meter aperture Gregorian-Dragone telescope, providing an 8′ beam at three frequency bands centered on 150, 250 and 410 GHz. The telescope is designed to measure or place an upper limit on inflationary B-mode signals and to probe B-modes originating from gravitationnal lensing of the CMB. The higher EBEX frequencies are designed to enable the measurement and removal of polarized Galactic dust foregrounds which currently limit the measurement of inflationary B-modes [1]. Polarimetry is achieved by rotating an achromatic half-wave plate (HWP) on a superconducting magnetic bearing. In January 2013, EBEX completed 11 days of observations in a flight over Antarctica covering 6,000 square degrees of the southern sky. This marks the first time that kilo-pixel TES bolometer arrays have made science observations on a balloon-borne platform.

In this thesis we report on the construction, deployment and data analysis of EBEX. We review the development of the pointing sensors and software used for real-time attitude determination and control, including pre-flight testing and calibration. We then report on the 2013 long duration flight (LD2013) and review all the major stages of the analysis pipeline used to transform the $\sim$1 TB of raw data into polarized sky maps. We review "LEAP", the software framework developed to support the analysis pipeline. We discuss in detail the novel program developed to reconstruct the attitude post-flight and estimate the effect of attitude errors on measured B-mode signals. We describe the bolometer time-stream cleaning procedure including removing the HWP-synchronous signal, and we detail the map

making procedure. Finally we present a novel method to measure and subtract instrumental polarization, after which we show Galaxy and CMB maps.

Contents

List of Figures

xvi

xvii

List of Tables

Acknowledgements

I am so grateful to have worked with the team at the Miller Lab and in the EBEX collaboration as a whole. You have made my graduate school years really fun and exciting.

Amber, you have been such a wonderful advisor. I have come out of every single meeting with you feeling energized and with a renewed enthusiasm and set of ideas to solve whichever problem I am working on at that time. It is thanks to you that I decided to go to graduate school. Thank you for always making time for us, creating a very positive atmosphere within our group and enduring our geeky computer oriented conversations and arguments.

Chappy, Britt, Michele, Seth – what a bear family. Thank you for teaching me everything I know about hardware and software, for making Nevis and field trips so enjoyable, for sharing coffee and chocolate multiple times a day and talking as much about food as a French girl needs, and for making me laugh so hard with your inappropriate jokes. I would like to also thank all the EBEX graduate students at UMN, McGill, Berkeley and Brown for making field trips fun in addition to being insane. Shaul, thank you for leading EBEX and for teaching me to stand my ground in our countless arguments. Derek, the analysis for EBEX was a long and difficult process and I am really happy you were around to exchange ideas and share the load. Delphine, thank you for being my support system and my local family during those long graduate school years. You really made NY my home.

Maman, I cannot thank you enough for passing on to me your curiosity, your love of learning and knowledge, and for always encouraging me to pursue my interests. I know it must have been hard to give me your blessing to go spend so many years so far away. Wherever your are, I hope you are proud. Dad, thanks for not actually locking me in the cellar to stop me from leaving France during my short visits. Eloise, Arthur – thank you for enduring a little sister who always wants to be right, and for always making time for me when I visit such that I don't feel like we are drifting apart.

Chappy, I don't think I could have gone through graduate school and working those long hours if you hadn't been supporting me. I learned so much from you and how you approach

problems, and I just generally loved working with you, even though you are right way too often for my taste. We worked such long hours in high bays at night, in the cold, developing the star cameras. I think it is a testimony to our relationship that we survived working together and being around each other non-stop for nearly four years. I hope we will get to work together again someday.

Chapter 1

Science

1.1 The Standard Cosmological Model

The observation that the universe is expanding [2], and the assumption that the universe is isotropic and homogeneous on large scales, leads to the construction of the Friedmann-Lemaitre-Robertson-Walker metric:

$$\mathrm{d}s^2 = -\mathrm{d}t^2 + a^2(t)\left[\frac{\mathrm{d}x^2}{1 - kx^2} + x^2(\mathrm{d}\theta^2 + \sin \mathrm{d}\phi^2)\right] \tag{1.1}$$

where s is the co-moving spacetime metric, k is the curvature of the universe, t is the proper time and $a(t)$, the scale factor of the universe, encodes the scaling of the physical distance between objects at time t. Using this metric to solve the Einstein field equations yields the Friedmann equation describing the time-evolution of the size of the universe as a function of its content and geometry:

$$\left(\frac{\dot{a}}{a}\right)^2 = \frac{8\pi G}{3}\rho - \frac{k}{a^2} \tag{1.2}$$

where G is the gravitational constant, and ρ is the total energy density of the universe ($c = \hbar = 1$ in this chapter) including contributions from ordinary matter, dark matter and

1

dark energy. Since the 1960's, experiments measuring a multitude of different phenomena like the Hubble constant [3], the size of CMB anisotropies [4], or the accelerating expansion of the universe [5, 6] have led to the most widely accepted cosmological model, called ΛCDM, describing the contents of ρ and the evolution of $a(t)$. In this model, the universe expanded from a hot and compact plasma to the state we observe it in today. The current measurements hold that universe is spatially flat ($k = 0$) and the energy density of the universe is constituted at 68% by dark energy (the cosmological constant Λ), 27% by cold dark matter (CDM) and only 5% by ordinary matter [7]. The ΛCDM model is defined by only six parameters. Three of them are the energy densities of dark energy, dark matter and baryonic (ordinary) matter, and the other three are the curvature of the universe k, the optical depth τ at re-ionization, and the scalar spectral index n_s. With only six parameters, the ΛCDM model has successfully accounted for a wide range of observations from a host of experiments like the baryon acoustic oscillation (BAO) [8], the abundance of light element [9] and properties of the Cosmic Microwave Background [7].

1.2 The Cosmic Microwave Background Temperature

The early hot universe was fully ionized and contained a photon-baryon plasma in which photons were tightly coupled to free electrons through Thomson scattering. As the universe expanded and cooled, around 380,000 years after the Big Bang, the electrons became bound to nuclei, a process referred to as recombination. The photons then free-streamed from all locations and in all directions, creating the Cosmic Microwave Background (CMB) still observable today. This background radiation has an almost perfect black body spectrum and the expansion of the universe has red-shifted its present day temperature to 2.725 K [10]. The "surface of last scattering" refers to the set of points located at the correct distance from Earth such that we are now receiving the photons emitted from those points at recombination.

The CMB is found to be a black body, with the temperature varying as a function of direction to 1 part in 10^5 [11]. The sky map of CMB anisotropies, as measured by the Planck instrument, is plotted in Figure 1.1. The temperature anisotropies are caused by density inhomogeneities in the photon-baryon fluid [12]. Prior to recombination, these inhomogeneities evolved over time. Denser regions get denser under the effect of Gravity, which increases temperature and photon pressure, providing a restoring force and producing acoustic oscillations in the fluid. After recombination, the free-streaming photons carry the imprint of the state of the fluid before decoupling. Photons escaping from dense regions are hotter, but get red-shifted from escaping a gravitational well and appear as cold spots in the CMB. Photons escaping sparser regions appear as hot spots.
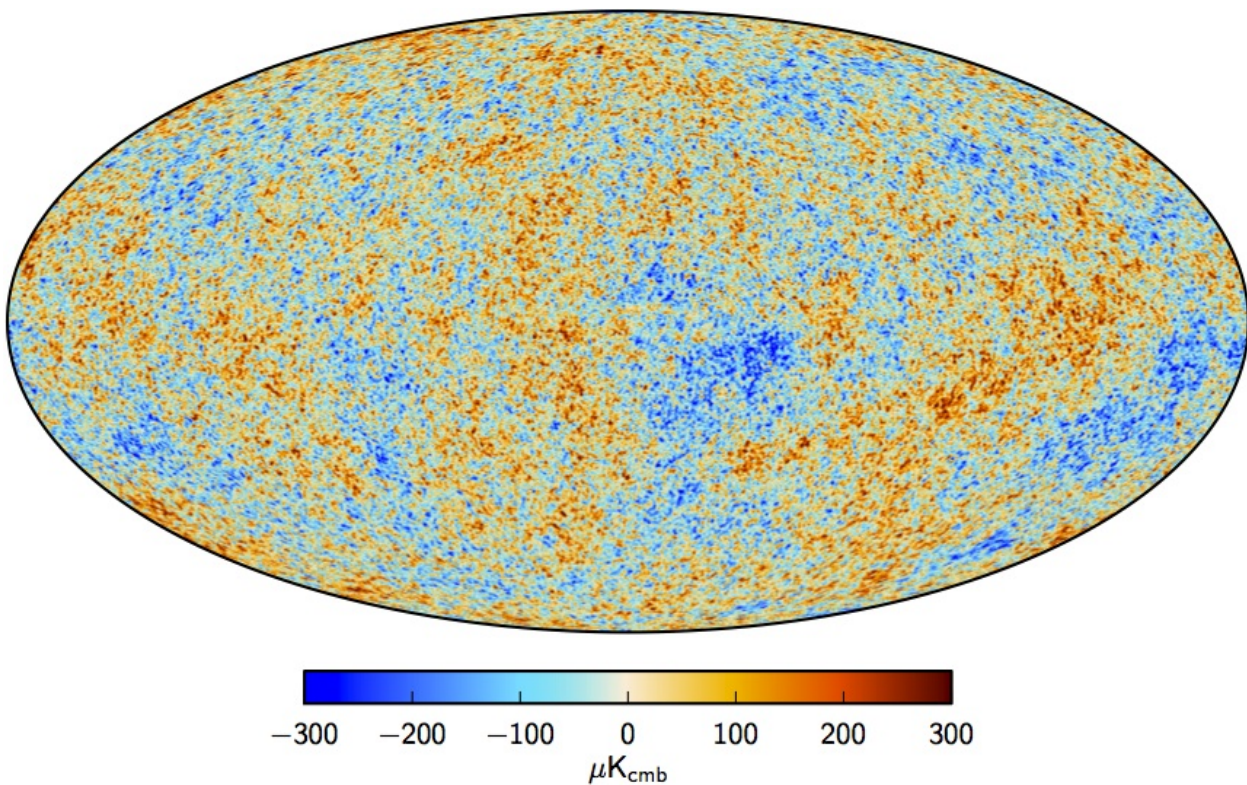
Figure 1.1: Map of the CMB temperature anisotropies measured by the Planck instrument. The monopole and dipole have been subtracted. Multiple frequency bands are used to reconstruct the CMB. Figure from [13].

To quantify CMB temperature anisotropies as a function of angular scale, we decompose

3

the temperature pattern in spherical harmonics:

$$\frac{\Delta T}{T} = \sum_{\ell,m} a_{\ell m} Y(\theta, \phi) \tag{1.3}$$

where (θ, ϕ) describe the orientation on the sky. If the universe is isotropic, we can average the a_{lm} at a given ℓ to get the fluctuations of the temperature as a function of the angular scale, also known as the power spectrum C_ℓ^{TT}:

$$C_\ell^{TT} = \frac{1}{2\ell + 1} \sum_m \langle a_{\ell m}^* a_{\ell m} \rangle \tag{1.4}$$

In Figure 1.2 we plot the power spectrum of the CMB temperature measured by the Planck experiment [7]. The six parameters of the ΛCDM model are fit with the shape of this power spectrum.

CMB temperature anisotropies were first discovered by COBE in 1992 [14] and their measurement have since then been refined by many experiments including WMAP [15] and Planck [7].

1.3 Cosmological Inflation

Several observed properties of the universe remain unexplained by the ΛCDM model and require further theories. Cosmological inflation is a widely studied extension to ΛCDM, proposed to solve the remaining problems. Inflation represents a variety of theories sharing the core idea that during the first fraction of a second after the Big Bang ($\sim 10^{-34}$ seconds), the universe underwent exponential expansion, being stretched by a factor of $\sim 10^{26}$ [16]. The problems that inflation addresses are listed here:

- **Horizon Problem:** Observation of the CMB shows remarkable uniformity across the sky and suggests the universe was in thermal equilibrium at the time of its emission, $\sim$380,000 years after the Big Bang. However given the history of the expansion rate in
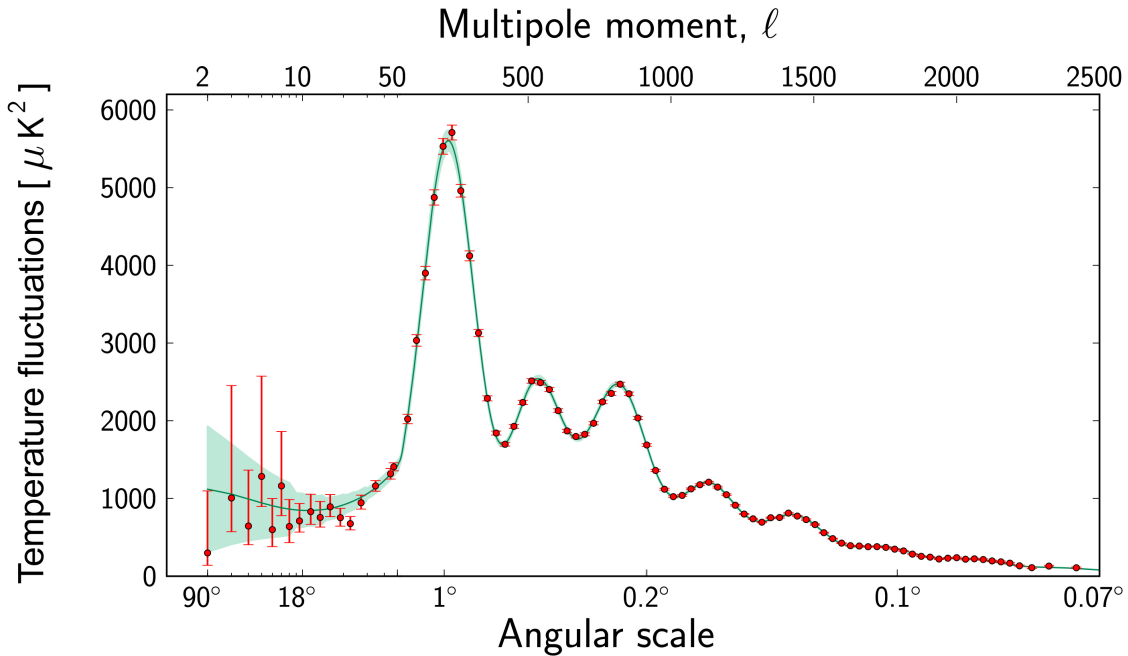
Figure 1.2: Measurement of the power spectrum of the CMB temperature (TT) by Planck and best-fit model. Figure from [13].

ΛCDM and the age of the universe 13.8 billion years, only small parts of the universe should have had time to be in causal contact (causal regions at t = 380,000 years span a ∼2° angle on the sky today). Inflation solves that problem with the initial exponential expansion, bringing the observable universe together in the first fraction of a second after the Big Bang.

- **Flatness Problem:** Measurements to date [17] show that the universe is flat to less than 1%. This implies that the curvature of space at the Big Bang must have been many orders of magnitudes closer to zero, which requires fine-tuning of the initial conditions. Inflation solves that problems because the exponential expansion dilutes the curvature of space, effectively removing the dependence on the initial conditions.

- **Relic Problem:** The existence of "relic" particles such as magnetic monopoles are predicted by Grand Unification Theories at the high temperatures occurring in the

5

very early universe. Experiments to date have failed to measure any such relic particle. Inflation solves that problem by diluting the density of such relics, formed only at the very beginning of the universe, to the point where detection is unlikely [16].

Inflation requires the creation of a new field ϕ called the inflaton with an associated potential $V(\phi)$ driving the inflation. In the simplest inflation models (called "slow roll"), the inflaton is a scalar field with a large potential energy (of order of the Planck energy) that dominates the Friedmann Equation 1.2. The field slowly rolls down a potential slope during inflation, and finally reaches the potential minimum at which point inflation stops. The shape of the potential is motivated by requiring exponential expansion at the beginning of the universe and an insignificant field today.

Inflation provides an explanation for the fluctuations in the CMB and the large scale structures we observe today. Quantum mechanics predicts the existence of microscopic fluctuations in the inflaton, and those fluctuations are stretched to astronomical scales during inflation. These fluctuations can be separated into scalar, vector and tensor perturbations. Scalar perturbations produce density fluctuations in the early plasma which source the temperature anisotropies in the CMB and provides the seeds of growth for large scale structure. Tensor perturbations source gravity waves that propagate from the inflationary era to the present day. As we will show in the next section, those gravity waves imprint a polarization signature on the CMB. The search for this signature has been a priority for the CMB community as it would be a strong evidence for inflation and would provide a probe of fundamental physics at energy scales inaccessible to any terrestrial laboratory. The ratio of tensor to scalar perturbations, often call "tensor to scalar ratio" or just "r", constrains in simple inflation models the energy scale at which inflation took place [15]:

$$V^{1/4} \propto 10^{16} r^{1/4} \ \text{GeV} \tag{1.5}$$

1.4   The Cosmic Microwave Background Polarization

1.4.1   Mechanism for Polarizing the CMB

The CMB gets linearly polarized through Thomson scattering off electrons seeing in their rest frame quadrupolar perturbations of the surrounding photons. Before recombination, photons are coupled to electrons in the plasma fluid such that quadrupolar perturbations of the photons is generated from perturbations in the fluid temperature. Figure 1.3 shows a diagram of how such perturbations create linear polarization.
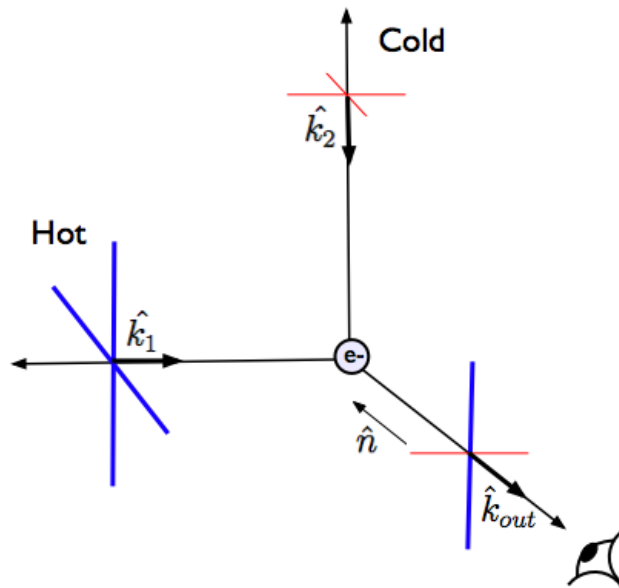
Figure 1.3: In Thomson scattering, electrons oscillate in a direction parallel to the electric field of incoming radiation. Electrons then re-emit photons through dipole radiation, which is strongest in the direction perpendicular to that of their oscillating motion and is polarized parallel to the direction of motion. In the diagram, hotter unpolarized photons are incident on an electron from left and right, producing in the direction $\hat{n}$ of the viewer (coming out of the page) radiation polarized along the blue line. Colder unpolarized photons, incident on the electron from top and bottom, produce along $\hat{n}$ radiation polarized along the red line, producing a total net polarization. Figure based on [18].

Temperature perturbations in the plasma fluid originate from fluctuations in the inflaton field and have three distinct geometrical sources: scalar (corresponding to density fluctuations in the fluid), vector (corresponding to vortices in the fluid) and tensor (corresponding

to gravitational waves in the fluid). In the spherical harmonic decomposition of a quadrupole moment, these different modes correspond to $\ell = 2$ and $m = (0, 1, 2)$. Since vortices decay as the universe expands and are negligible by the time of recombination, they are not addressed below.

The above decomposition is useful because it can be shown that after integration over all possible wavevectors $\vec{k}$, the non-local polarization pattern on the sky resulting from each mode has distinct properties [18]. Scalar perturbations, the dominant source of CMB polarization, produce only curl-free patterns called "E-modes". Tensor perturbations, a much weaker source of CMB polarization, produce an equal amount of E-modes and a divergence-free pattern termed "B-modes". The polarization patterns of E and B-modes around cold or hot spots is shown in Figure 1.4.
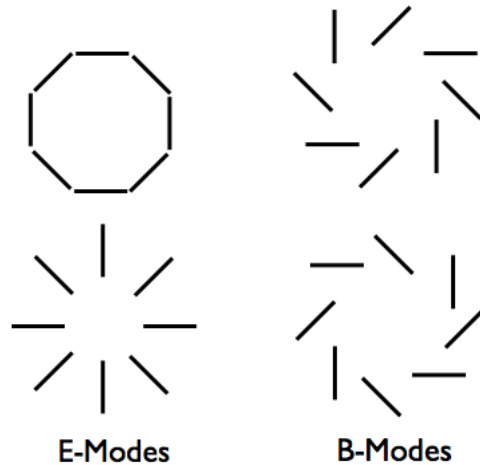
Figure 1.4: Patterns of linear polarization observed in the CMB. *Left:* Curl-free E-mode patterns formed around hot (top) and cold (bottom) regions. *Left:* Divergence-free B-mode patterns formed around hot (top) and cold (bottom) regions.

The first detection of E-mode polarization anisotropies in the CMB was made by DASI in 2002 [19]. To date, E-modes have been measured by multiple experiments [20][21][22][23][24][25][26]. The search for gravitational wave B-modes is still ongoing and is an important focus of the CMB community as it would probe fundamental physics and be a strong argument confirm-

ing inflationary scenarios. Figure 1.5 shows simulated angular power spectrum for E-modes and predicted B-modes for $r = 0.05$ and $r = 0.01$. Measurements from a host of experiments are also included in the Figure. The current best constraint on r from CMB polarization experiments is $r < 0.11$ at 95% [1].

Two other sources in the sky can generate B-modes. Gravitational lensing of the CMB by intervening galaxies mixes CMB E-modes and B-modes together [27]. This mixing contributes significantly to the expected B-mode power spectrum, but only at small angular scales (high ℓ in Figure 1.5). To date three experiments have detected lensing B-modes [28, 29, 30]. Their measurements and the best-fit lensing B-mode contribution to the power spectrum is shown on Figure 1.5. Polarized emissions from our Galaxy, termed 'Galactic dust', contributes B-mode patterns at the same angular scales as gravitational wave B-modes. Emissions from Galactic dust have a different frequency power spectrum than the CMB, and Galactic foregrounds can be characterized and subtracted by using measurements at different frequencies. In 2014, BICEP2 announced a discovery of gravitational waves B-modes [31], but a later joint analysis between BICEP2 and Planck [1] concluded the B-modes observed by BICEP2 originated from Galactic dust. As shown in [1], Galactic foregrounds are currently the most significant obstacle to measuring inflationary B-modes. EBEX was specifically designed to simultaneously observe CMB and Galactic dust, using high frequencies available at balloon altitudes to characterize and remove dust.

1.4.2 Stokes Parameters

Electromagnetic radiation propagating along some $\hat{e}_z$ axis has historically been described using the electric field $\vec{E}$:

$$\vec{E}(t) = E_x \cos(kz - \omega t - \phi_x)\hat{e}_x + E_y \cos(kz - \omega t - \phi_y)\hat{e}_y \qquad (1.6)$$

where k is the wavenumber, ω is the radiation frequency and ϕ_i is the phase of the wave

along each axis. The CMB community usually works with an alternative parametrisation, called the Stokes parameters. The Stokes parameters are convenient and natural to measure because they are linear in intensity. They are defined by:

$$I \equiv E_x^2 + E_y^2 \tag{1.7}$$

$$Q \equiv E_x^2 - E_y^2 \tag{1.8}$$

$$U \equiv 2E_x E_y cos(\phi_y - \phi_x) \tag{1.9}$$

$$V \equiv 2E_x E_y sin(\phi_y - \phi_x) \tag{1.10}$$

For linearly polarized light, $\phi_x = \phi_y$ and $V = 0$. Stokes I represents the total intensity of the radiation. Stokes Q and U represent linear polarization along two axis rotated by 45°, as shown in Figure 1.6. A frame of reference must be defined when measuring Stokes parameters. Throughout this thesis, we use two frames of reference:

- **Sky frame:** The reference frame for the Stokes parameters is fixed with the Galactic reference frame. We use WMAP conventions [11]: the polarization that is parallel to the Galactic meridian is Q > 0 and U = 0.
- **Instrument frame:** The reference frame for the Stokes parameters is fixed with the instrument. Positive Q axis is defined as the axis of symmetry of the telescope. See Chapter 8 for more details.

The conversion from Q and U power spectra to E and B power spectra is given at the end of Chapter 8 by Equations 8.9.6 and 8.9.6.

$$*$$

$$* \quad *$$

As we will detail in the next chapter, this thesis describes the construction, deployment and data analysis of EBEX. EBEX is a balloon-borne experiment designed to measure the polarization of the CMB at 150, 250 and 410 GHz. The lower frequencies are intended to

measure or put an upper limit on both the gravitational waves and lensing B-modes, with the higher frequency intended to measure and subtract Galactic dust foreground B-modes.
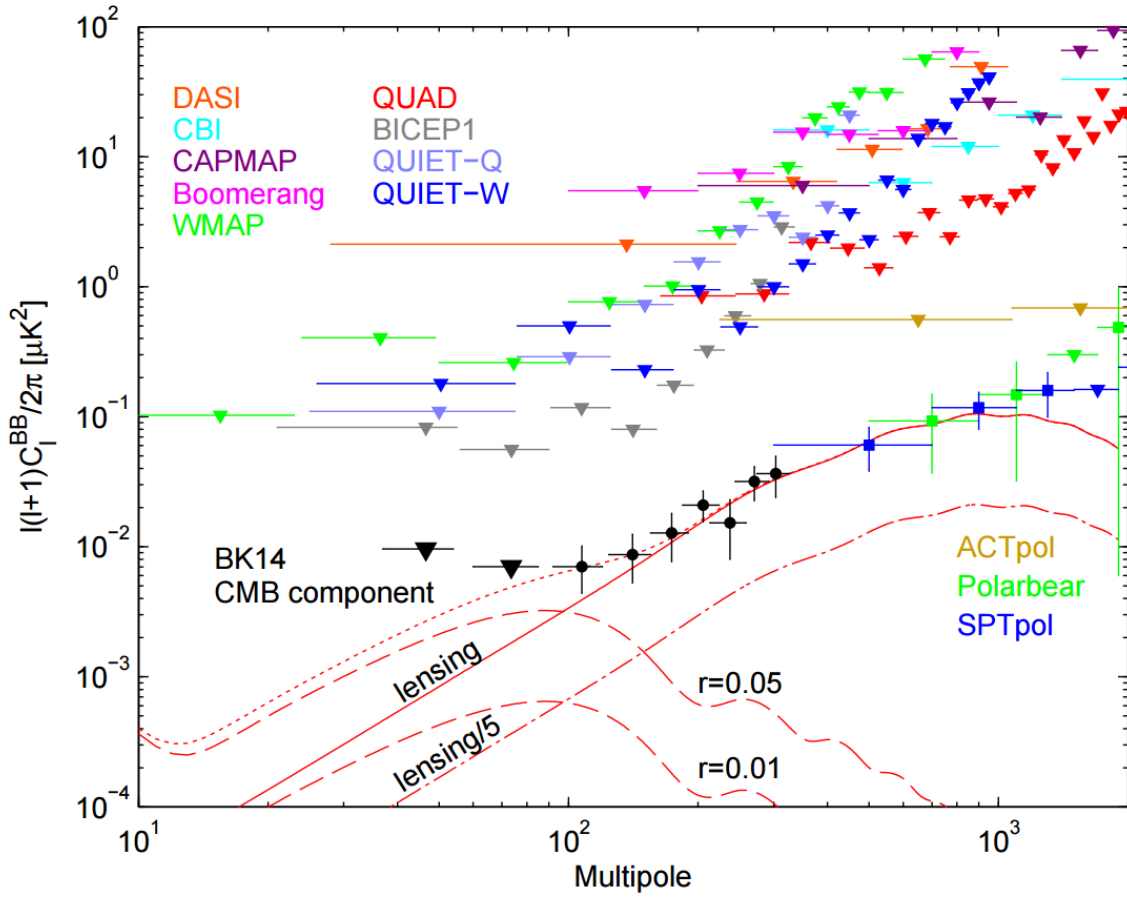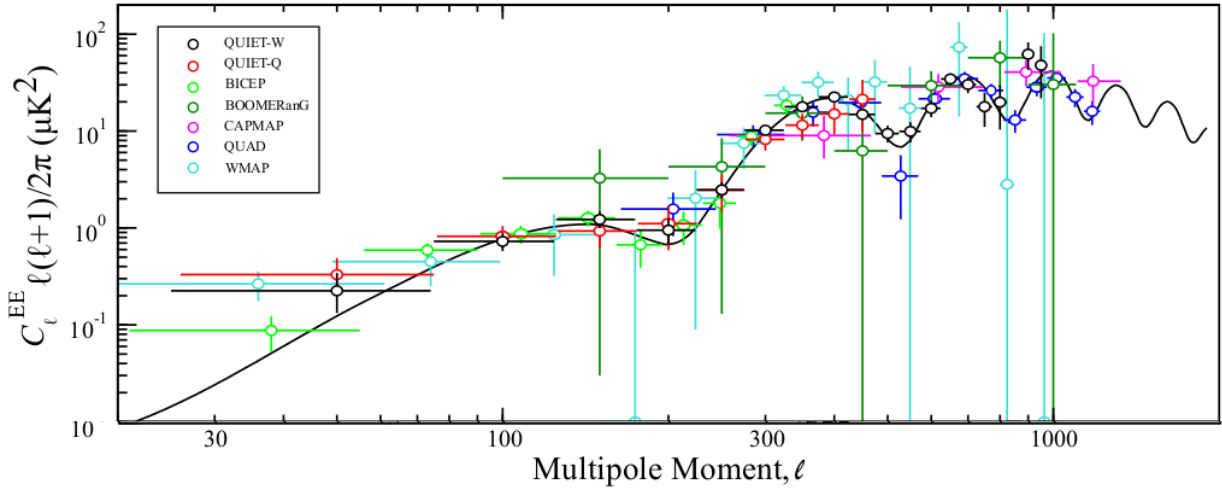
Figure 1.5: *Top*: Measurements and best-fit model of the CMB E-mode power spectrum. Figure adapted from [28]. *Bottom*: B-mode power spectrum. Colored data points show measurements to date (with the exception of ACTPol who has published improved measurements in [29]). Red dashed lines show expected gravitational waves B-modes for $r=0.05$ and $r=0.01$. Solid red line shows the best fit lensing B-mode power spectrum. Figure from [32].
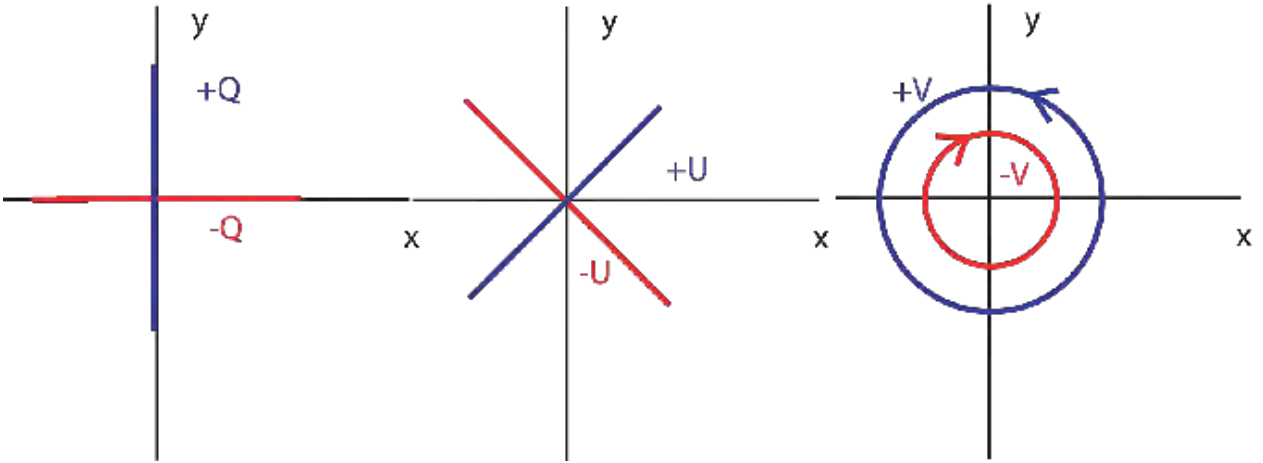
Figure 1.6: Patterns of polarization represented by the Q, U and V Stokes parameters with a defined $\hat{e}_x$, $\hat{e}_y$ frame of reference. Q and U represent linear polarizations. Positive and negative Q represent polarization along axes rotated by 90°. U linear polarization is rotated by 45° from Q. V represents circular polarization.

Chapter 2

Instrument Overview

2.1 Summary

The E and B experiment (EBEX) [33] is a balloon-borne microwave polarimeter. It is designed to achieve three primary science goals:

- Detect or put an upper limit on the B-mode power spectrum of the CMB.
- Measure the E and B-mode power spectra of Galactic foregrounds, particularly of dust emission.
- Measure the B-mode power spectrum from lensing of the CMB.

The ~6,000 lbs instrument consists of a gondola with a telescope, detectors, pointing sensors and telemetry. Figure 2.1 shows a model and a picture of the whole telescope. It measures the polarization of the CMB with 8' resolution at 150, 250 and 410 GHz. The payload collects data while suspended from a 10^6 m^3 stratospheric balloon at an altitude of ~35 km that circumnavigates Antarctica. In January 2013, EBEX completed 11 days of observations in a flight over Antarctica.
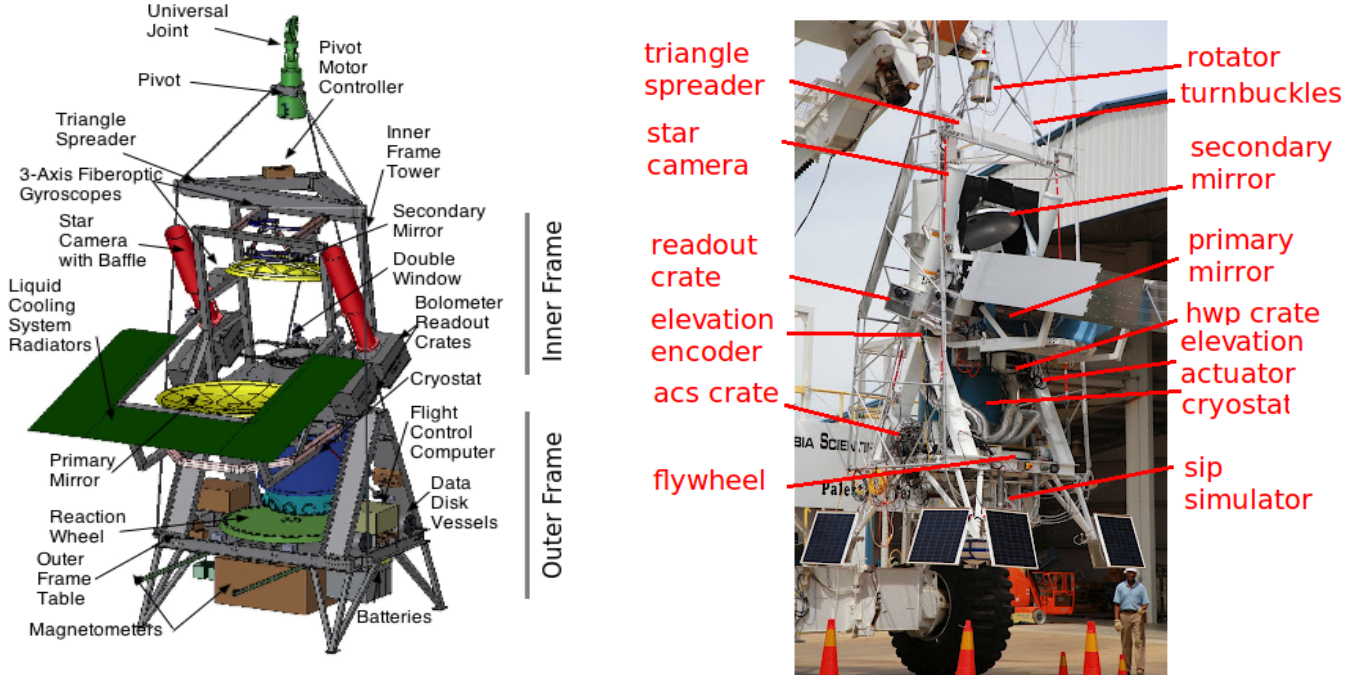
Figure 2.1: *Left*: Gondola model. *Right*: Picture of the gondola during the 2012 Palestine integration campaign. The gondola is being suspended from 'Tiny Tim' truck.

2.2　Advantages of Using a Balloon-borne Telescope

At 35 km altitude only ∼10% of the atmosphere remains. The reduced atmospheric loading enables a higher sensitivity detector array, and provides access to frequencies inaccessible to ground-based instruments. With access to higher frequencies, an experiment can be designed that is sensitive to only a single Galactic foreground, dust. The Antarctic polar summer provides the telescope with constant daylight to charge the solar panels and ensures a relatively constant altitude (since there is no diurnal changes in temperature) which in turn minimizes variability in detector loading.

2.3 Gondola, Attitude Control System and Telemetry

2.3.1 Gondola

The telescope is mounted in an aluminum structure called the gondola. It consists of a cable-suspended outer frame that moves the whole structure in azimuth, and an inner frame holding the telescope that moves in elevation. The inner and outer frames connect at a pivot point, the trunnion bearing assembly. The gondola holds the receiver, the optics, the pointing sensors and motors, the electronic crates, and the power and telemetry systems, as shown in Figure 2.1. The outer frame hangs from an aluminum triangle spreader bar through four synthetic ropes. The triangle hangs from a rotator motor (the pivot) and a universal joint, which at float connects to the flight train and balloon. The azimuth motion is powered through the pivot motor. A motorized reaction wheel on the gondola provides fine control of the azimuth motion. The inner frame can move in the elevation direction through the elevation actuator connecting the outer and inner frames and powered by a brushed DC motor. To shield the instrument from the sun, aluminized polyester covered baffles are mounted on the inner and outer frames of the telescope. The instrument is powered by a set of lithium-ion batteries, recharged at float by 30 solar panels mounted on the gondola and covering a total of 17.2 m^2. It consumes 1858 W at float. An in-depth review of the gondola's design is available in [34].

2.3.2 Attitude Control System

The Attitude Control System (ACS) of the gondola was inherited from BLAST [35] and adapted for EBEX. It performs two tasks: collecting attitude information and orienting the telescope. Pointing sensors mounted on the gondola collect attitude information which is transmitted to the flight control program (FCP) running at 100.16 Hz. FCP uses sensor information to estimate the gondola's attitude, which is then used by the ACS electronics to send currents to the azimuth and elevation motors to orient the telescope according to

a scan strategy. The pointing sensors' information is also recorded and used post-flight to make sky maps from the detectors' timestreams. I was responsible for developing the ACS, and describe the system in more detail in Chapter 3.

2.3.3 Telemetry

During flight, low bandwidth communication with the payload from ground is possible through telemetry provided by CSBF. This enables commands to be sent to the telescope, and downlink of some detector data and system health channels. EBEX produces ~ 5.2 Mpbs of data. During the first 12 hours of the flight, the telescope is in line of sight and a 1 Mbps link is available. After this we have to use a network of TDRSS communication satellites providing between 6.0 kbps and 70 kbps. The on-board data thus needs to be saved to disk and recovered after the flight. Furthermore, algorithms to compress and prioritize downlink data were developed for EBEX. Details can be found in [36].

2.4 Optics and Receiver

2.4.1 Light Path

The EBEX optics consist of two warm mirrors positioned in an off-axis Gregorian Mizuguchi-Dragone configuration, followed by a series of re-imaging cold lenses situated inside of the receiver. The challenge in designing the telescope is providing a high quality image (Strehl ratio ≥ 0.85 for the ~ 1000 detectors) on a 6 degree focal plane, while still minimizing cross-polarization effects (mixing of one polarization into the other). Figure 2.2 shows the optics and a ray tracing of the incoming light. Sky radiation is first reflected on the warm 1.5 m primary mirror and on the secondary mirror before entering the cryostat through a 0.02 in thick vacuum window made of ultra-high molecular weight polyethylene (UHMWPE). The sky image forms at the entry of the cryostat on the field lens, as is shown in Figure 2.2, and is then re-formed on the focal plane by a series of UHMWPE lenses inside the cryostat. The
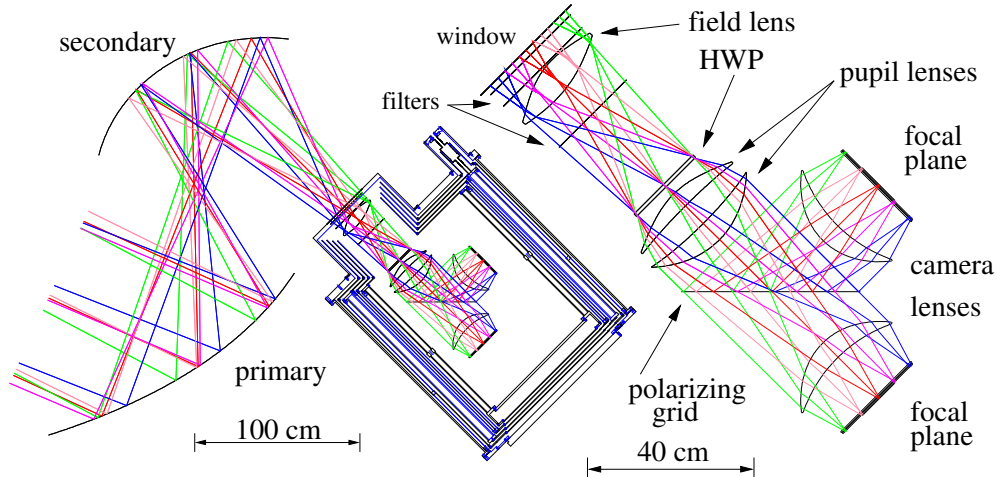
Figure 2.2: Simulation of the ray tracing in the EBEX telescope, including on the right a zoom of the cold optics inside the cryostat. Figure courtesy of Huan Tran.

CMB photons also go through a half-wave plate (HWP) and a polarizing grid oriented 45 degrees with respect to the beam which splits the radiation towards the two identical focal planes. Atop each wafer on the focal plane sits a band-defining low-pass copper metal-mesh filter in polypropylene. Radiation is then coupled to the detectors with conical feed-horns and cylindrical wave guides, as show in Figure 2.5.

The frequency band of each wafer is primarily defined on the high edge by the low-pass metal-mesh filter and on the low edge by the wave guide. The bands are centered around 150, 250 and 410 GHz, with a ~13 % band-pass. The beam size is 8 ′ at all frequencies. Details on the optics can be found in [37].

2.4.2 Receiver

The receiver is encased in a cryostat, which is cooled with liquid nitrogen and helium. The cryostat is separated in different temperature stages, going from 300 K at the window to 270 mK at the focal plane. The liquid cryogens are used to cool to 4 K, and two closed-cycle helium adsorption fridges cool the focal planes to 270 mK. Figure 2.3 shows a picture of the inside of the receiver, and a cutaway of the cryostat model. The receiver is described in
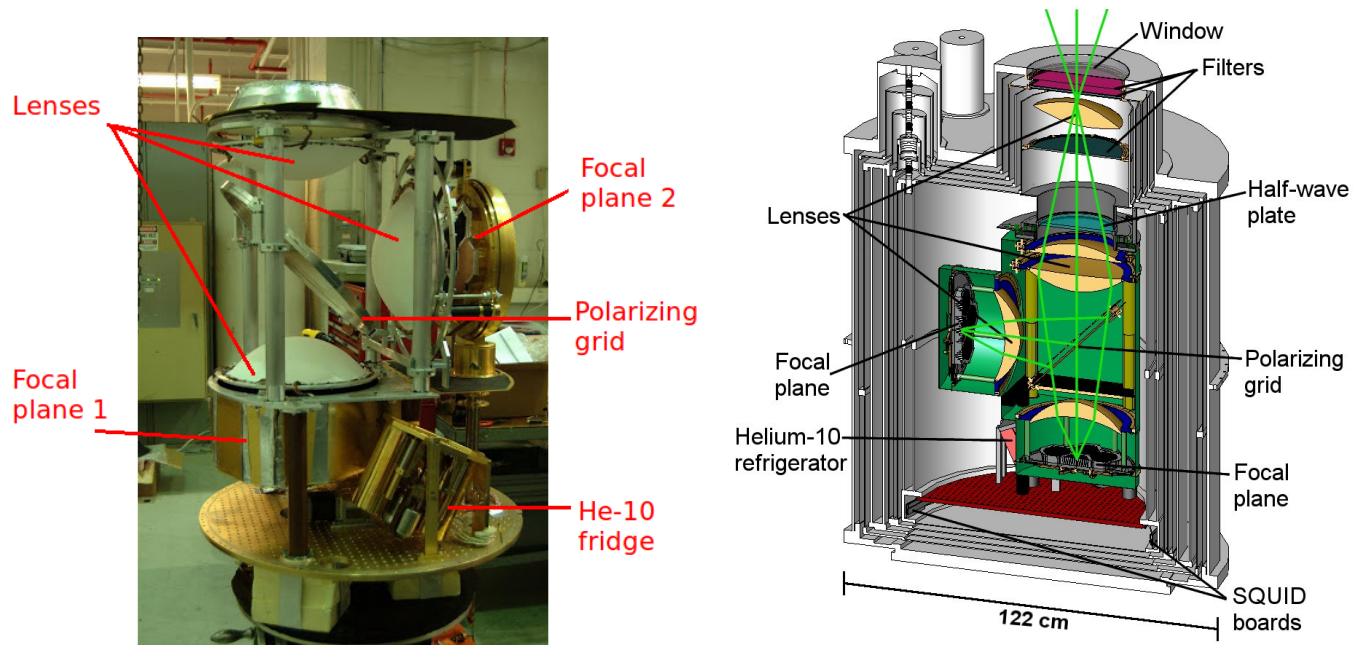
Figure 2.3: *Left*: Picture of the receiver's inside during the 2011 Palestine integration campaign. Picture from Asad Aboobaker *Right*: Cut of the cryostat showing all the optical elements inside the receiver.

more details in [38].

2.5   Polarimetry

The polarimetry in EBEX uses a HWP modulator and a wire grid analyzer. In the 2013 LDB flight, the HWP rotated at frequency $f_{hwp} = 1.23$ Hz. The electric field vector of incoming linearly polarized light gets rotated by the HWP at $2f_{hwp}$, and the polarization rod at $4f_{hwp}$ (see Figure 2.4). The wire grid analyzer transmits the projection of the polarizing rod along the analyzer's axis. The power transmitted through the analyzer varies sinusoidally at frequency $4f_{hwp}$. The detectors are sensitive to total power absorbed. The amplitude and angle of the incoming linear polarization is measured by the sine wave's amplitude and phase.

Using a HWP modulator mitigates systematic effects. Any polarized emission from the receiver components downstream of the HWP will not be modulated at $4f_{hwp}$ and do not
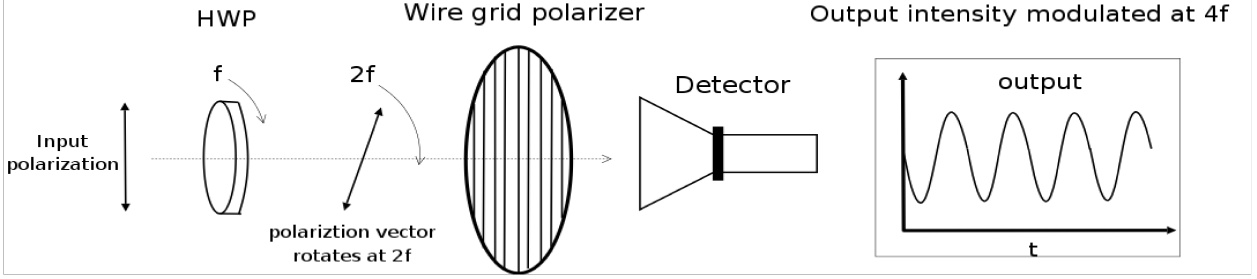
Figure 2.4: Diagram of the polarimetry on EBEX. The incoming polarized radiation is modulated by a HWP rotating at frequency f_{hwp}, and analyzed by a wire grid. Linearly polarized radiation appears as a sine wave with frequency $4f_{hwp}$ in the detector timestream. Figure courtesy of Johannes Hubmayr.

contribute systematic errors in the signal bandwidth. It also enables single detectors to measure both components of the polarization at every time sample, discarding the need to difference the signal from two detectors and systematic effects associated with different gains and beams between detectors. Finally, the modulation pushes the polarization signal to a higher bandwidth (around $4f_{hwp}$), away from the 1/f noise of the detectors. To enable the HWP to work at our three observing frequencies, we use an achromatic HWP (AHWP) made of 5 layers of birefringent sapphire crystals, with their optical axis rotated one from another. This gives the EBEX AHWP a 98 % modulation efficiency from 120 GHz to 450 GHz.

The AHWP is placed at the 22 cm aperture stop of the telescope, and is cooled to 4 K. To minimize the power dissipated at this cold stage, the AHWP is rotated using a superconducting magnetic bearing (SMB). The AHWP is glued to a strong permanent ring magnet with a rotationally invariant magnetic field. It levitates above a ring of superconducting ceramic tiles. The field of the ring magnet is effectively frozen inside the ceramic tiles at low temperatures, and the system resists any movement of the magnet except rotations. The AHWP is rotated with a Kevlar belt and a pulley system coupled to a brush-less motor located outside of the cryostat. Details on the design of the AHWP and on the SMB can be found in [39].
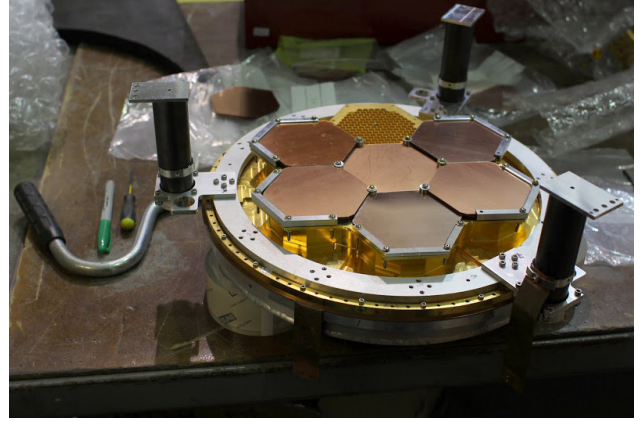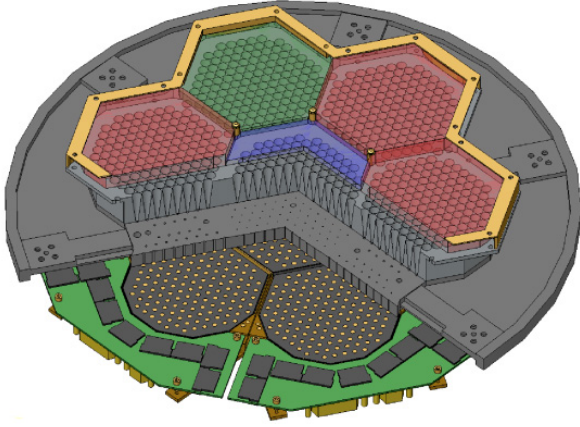
Figure 2.5: *Left:* Model of the focal plane, showing the filters, the feed-horns and the wave guides above the detectors. *Right*: Picture of one of the focal planes.

2.6 Detectors and Readout

The detectors in EBEX are Transition Edge Sensors (TES) bolometers. The detectors are packed on hexagonal wafers, and 7 wafers next to each other form a focal plane, as shown in Figure 2.5. Figure 2.6 shows a zoom on the focal plane from left to right: the entire focal plane, a wafer on which are laid 140 bolometers, and an individual bolometer. A total of 1107 detectors were in operation during the LD2012 flight.

A TES bolometer consists of an absorber, coupled to a superconductor (acting as a thermometer), linked to a thermal bath through a weak thermal link. When incoming radiation hits the low heat capacity absorber (the spider web structure in Figure 2.6), it heats it up very slightly. The absorber is thermally linked to a superconducting Al/Ti material, kept at its superconducting transition point through a voltage bias. In this regime, a small change in temperature corresponds to a relatively large change in resistance, which in turn corresponds to a measurable change in the current through the superconducting material (since the voltage bias is kept constant).

The current in the superconductors is amplified by low noise current amplifiers: super-conducting quantum interference device (SQUID) arrays. The readout electronics provide the AC voltage bias to hold each superconductor in its transition state. The signal from
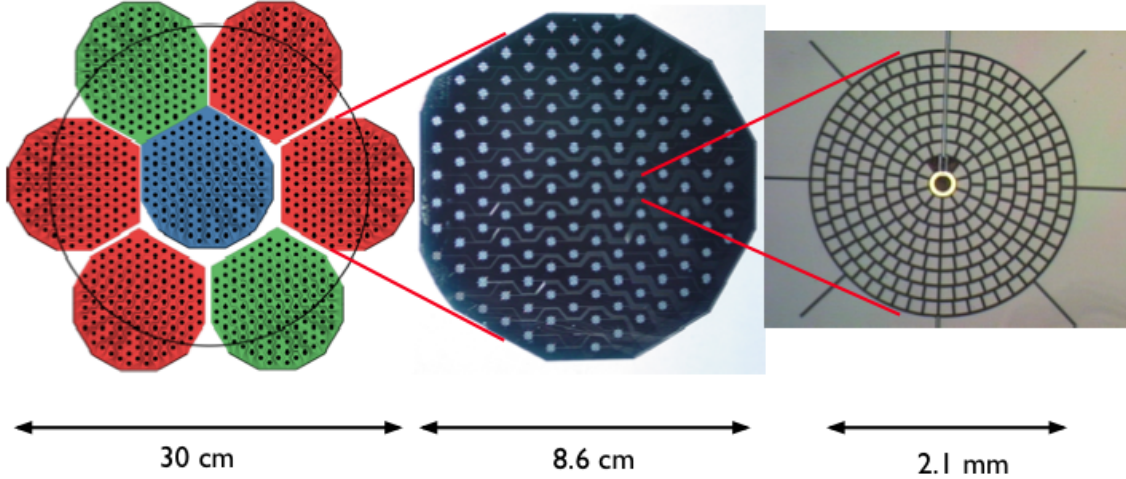
Figure 2.6: *Left:* Drawing of an EBEX focal plane, made of six wafers. Four wafers are at 150 GHz (red), two are at 250 GHz (green), and the center wafer is at 410 GHz (blue). *Center:* A single wafer, containing 140 bolometers. *Right:* A single bolometer. The spiderweb structure is the absorber. The superconducting material is in the center. Figure courtesy Clayton Hogen-Chin.

16 detectors is frequency multiplexed on two wires in order to reduce the number of wires and thus the thermal load on the cryogens and the power consumption of the telescope while at float. The detectors' current readout, voltage biasing and frequency multiplexing are done by processors located on 28 boards outside the cryostat. We call those boards the digital frequency multiplexing (DfMUX) boards. They are equipped with digital-to-analog and analog-to-digital converters to produce the AC voltage bias and record the detectors' currents. Details on the detectors and the readout system can be found in [40] and [41].

Chapter 3

In-flight Attitude Determination and Control

3.1   Overview

The ACS is responsible for acquiring attitude data, determining where the telescope should be pointing, and orienting the telescope accordingly. This chapter reviews the sensors used to measure attitude, the real-time code used to determine the attitude given sensor readings, the scanning code used determine where the gondola should be pointing, and the low-level control loops sending currents to the motors to orient the gondola. We also discuss the tests and analysis performed pre-flight to calibrate the sensors and to test the scan patterns.

The sensors and motors are mounted at various locations on the gondola. They communicate their data to four custom built electronic boards called the "Attitude Control System (ACS) cards" located inside the "ACS crate". Each card is equipped with analog to digital converters (ADC) and a Digital Signal Processor[1] (DSP). The DSPs run the low-level control loops. Two redundant flight computers collect the sensor information from the ACS cards and run the attitude determination loop and the scanning code. The sensor and motor

---

[1]ADSP 21062 from SHARC

data is written to redundant hard drives held at atmospheric pressure in cylindrical pressure vessels.

We first review the different coordinate systems used to describe attitude, after which we discuss the sensors and the various control algorithms.

3.2 Coordinates

3.2.1 Definition

Three spherical coordinate systems are used throughout this thesis: horizontal, equatorial and galactic. In each of them, a unit celestial sphere centered around the system's origin is used, as shown in Figure 3.1. The systems differ by the choice of the fundamental plane which divides the celestial sphere in two equal hemispheres, and the reference point in that plane which orients the x-axis. The z-axis is perpendicular to the plane, and the y-axis is inferred from the x and z axis to form an orthogonal basis. Table 3.1 lists the plane and the reference point used for each of these system.

Coordinate System	Reference Plane	Reference point	Origin[2]
Horizontal	Local Horizon	North Pole	Observer
Equatorial	Earth equator	Vernal equinox	Earth Center
Galactic	Galaxy	Galaxy Center	Sun Center

Table 3.1: Reference planes and points used in each coordinate system

To place a point P in a given spherical coordinate system, a radius ρ and two angles, ϕ and θ, are needed. In practice, we only need the direction of an object, and not its position, so ρ is never used. The angles are defined in the following manner:

- ϕ is a rotation around the z-axis. It is the angle that rotates the x-axis to intercept the great circle going through point P and the projection of the z-axis on the unit sphere.

---

[2]The origins of each coordinate system varies, but the distances between those origins is insignificant when computing ϕ and θ which reference points close to infinitively far away.
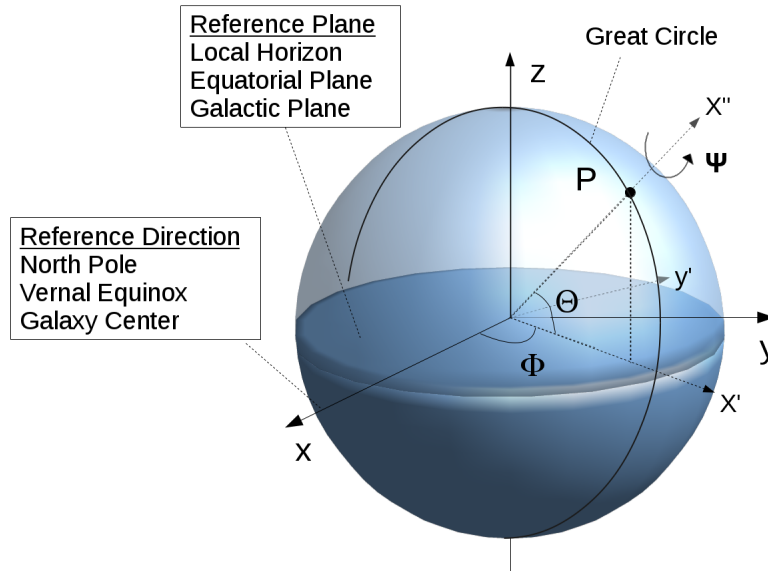
Figure 3.1: Diagram of a celestial coordinate system, showing the three Euler angles ϕ, θ and ψ describing the attitude. Note that θ in the diagram is negative.

The rotated x and y-axis are called x' and y'.

- θ is defined after the ϕ rotation as the rotation around the new y'-axis that rotates the new x'-axis to point towards P.

We often use the coordinate system not just to place a point in the sky, but to orient the direction in which the telescope is pointing. In this case, a third angle ψ is needed to describe the rotation around the final x"-axis, in order to fully constrain the telescope orientation. ψ is called the roll angle in all three coordinate systems. The angles ϕ, θ, and ψ correspond to three Euler angles needed to rotate one system into the telescope frame. The attitude of the telescope is the rotation of the telescope with respect to a given reference frame, and is fully determined by those three angles.

3.2.2 Naming Conventions

The angles ϕ and θ have different names in each of the coordinate systems mentioned. The names are listed in Table 3.2. Which names we use for ϕ and θ will tell the reader which

coordinate system we are using.

Coordinate System	ϕ	θ
Horizontal	azimuth (az)	elevation (el)
Equatorial	right ascension (RA)	declination (dec)
Galactic	longitude (lon)	latitude (lat)

Table 3.2: Names of the ϕ and θ angles in each coordinate system.

3.2.3 Angular Separation between Points

A note on computing angular separation between two points using the ϕ and θ angles. This is important throughout the thesis when attitude errors are calculated. Two points that have the same θ, but are separated by $\Delta\phi$, will have an angular separation that is dependant on θ. Their angular separation is $\delta = \Delta\phi \cos(\theta)$. For this reason, we often use the measure $co - \phi \equiv \phi \cos(\theta)$.

3.2.4 Transforming between Coordinate Systems

Most of the sensors on the instrument measure attitude in the horizontal reference frame. The star cameras operate in the equatorial reference frame. For post-flight analysis, it is convenient to make sky maps in the galactic coordinate system. A rotation will transform one system into the other. The orientation of the horizontal reference frame however is dependant on the observer's position on Earth and on the time (to determine the phase in the Earth's rotation). Therefore, GPS latitude and Local Sidereal Time (LST), are necessary to transform attitude in the horizontal reference frame to the equatorial or galactic reference frames.

3.3 Sensors

Balloon-borne instruments need reliable, redundant pointing systems both because minimal intervention is possible once the instrument is at float and because the temperature, pressure and radiation environment at float is very different from that on the ground, making end-to-end testing conditions difficult to reproduce before the flight. For this reason EBEX was equipped with redundant primary sensors (two star cameras and two sets of three orthogonal gyroscopes), but also with an array of less accurate but simpler, more reliable sensors: two magnetometers, sun sensors, differential GPS (dGPS), an elevation encoder and a clinometer. The coarse sensors do not have the accuracy required for post-flight attitude reconstruction, but provide real-time attitude both to give an attitude guess to the star cameras and in the eventuality that the star cameras cannot solve images in real-time. They are also the main sensors used during all the ground development and testing, when the gondola is indoors without access to stars. Figure 3.2 shows the location of most sensors.

When characterizing the sensors, we distinguish intrinsic precision and accuracy with their in-flight equivalents:

- Precision: The precision of a sensor in a laboratory experiment may be different than at float. For example, the magnetic fields on the gondola increase the noise in the magnetometer data, or the reflections of the GPS signal on the gondola will increase the noise in the dGPS measurements.
- Accuracy: Ultimately, the microwave beam attitude is what needs to be determined. Therefore all sensors must be calibrated to the beam, i.e. we find the angle offset between a given sensor and the beam. The intrinsic accuracy of the sensor will be calibrated away during this procedure. The in-flight accuracy of each sensor is determined by the quality of the calibration procedure. Practically, the sensors are calibrated to the star cameras, and then the star cameras to the beam.

In this section we list the sensors used and their intrinsic and in-flight precision. This is

27

summarized in Table 3.3. In Section 3.7 we describe the pre-flight calibration procedure, including the accuracy of the calibration. In flight, all the sensor offsets are re-computed with the first available star camera solution.

Sensor	Number	Attitude measured	Intrinsic Precision	On-board Precision	Update Rate
Star Camera	2	RA, dec	1.5 $''$	1.5 $''$	0.025-0.5 Hz
		& roll	48 $''$	48 $''$	0.025-0.5 Hz
Magnetometer	2	az	12 $'$	1.0 $°$	100.16 Hz
Sun Sensor	2	az	1 $'$	0.8 $°$	100.16 Hz
dGPS	2	az	0.5 $°$	0.8 $°$	5 Hz
Clinometer	1	el	1.2 $'$	0.5 $°$	100.16 Hz
Encoder	1	relative el	20 $''$	0.2 $°$	100.16 Hz

Table 3.3: List of EBEX attitude sensors and their specifications.

3.3.1 Star Cameras

EBEX has two star cameras, mounted on either side of the inner frame and roughly aligned with the telescope beam, as shown in Figures 2.1 and 3.2. They are the most accurate sensors in EBEX. They find their attitude by taking pictures of the stars and comparing the bright spots in the images to star catalogs. They are designed to do this at scan turnarounds, when the gondola changes azimuth direction, every ∼40 s, but they can solve multiple images per second. Each star camera consists of a telephoto lens, a CCD and a computer mounted in a rigid assembly inside a pressure vessel. The computer runs the Star Tracking Attitude Reconstruction Software (STARS) [42], a platform-independent software developed for EBEX in C++ that captures the images, finds the bright spots in the image, matches their pattern to a known catalog of stars and communicates with FCP. The images are saved on the star camera disks, and the attitude solution is communicated to FCP. The precision of the star cameras is mainly determined by the CCD and the lens. Each EBEX star camera contains a 200 mm f/1.8 lens[3] and a CCD[4] with 1536x1024 9 µm pixels. The camera has

---

[3]Canon EF 200 mm F/1.8 L USM Lens
[4]Kodak KAF-1603E image sensor
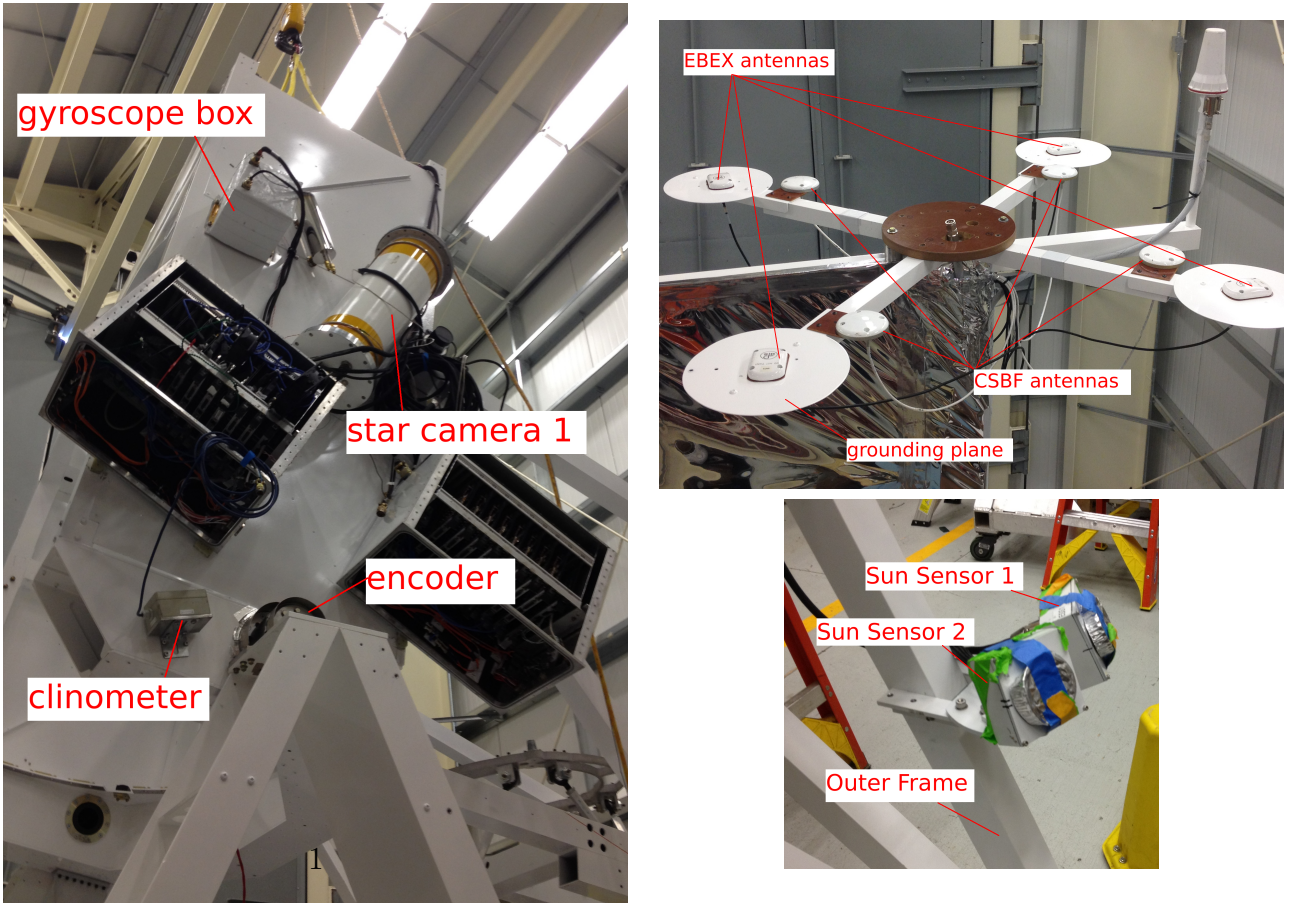
Figure 3.2: *Left:* Starboard side of the gondola showing star camera 1, gyroscope box A, the clinometer and the trunnion bearing assembly inside which the encoder is mounted. *Top Right:* EBEX and CSBF dGPS mounted on top of the gondola. *Bottom Right:* Sun sensors mounted on the outer frame, offset by ∼45 ° in azimuth. A protective cover is taped over the pinholes.

a FWHM of 9", which is also the approximate size of a pixel. The atmospheric brightness at 35 km altitude requires the star cameras to take 300 ms exposures in order to see stars. Given the necessary integration time, images must be taken at velocities under 2 $''$s^{-1} to avoid motion-blur. The pointing solutions have 1.5 $''$ accuracy in displacement angle on the sky, and 48 $''$ accuracy in rotation around the image center. A detailed review of the star cameras design and in-flight performance can be found in [43].

3.3.2 Gyroscopes

The attitude in between star camera solutions (or other sensors attitude updates) is integrated using gyroscope rates. EBEX has two redundant sets of three orthogonal fiber optic gyroscopes[5]. Each gyroscope measures the rate of angular rotation around its axis. The gyroscopes were chosen for their low rate white noise (40 $''$s^{-1}) and their 1/f noise properties: the timescale on which the 1/f noise varies is longer than the 40 s between star camera solutions. Each set of three gyroscopes is mounted inside an aluminium box precision machined to 5 mils such that they form a nearly orthogonal frame. Box A is mounted near star camera 1, as shown in figure 3.2. Box B is mounted near the secondary mirror on the inner frame. Each gyroscope outputs a digital signal at 1,000 Hz which is read out by the DSP. The data is de-spiked and passed through a stage 4 box-car IIR filter, and written to disk at 100.16 Hz.

3.3.3 Coarse sensors

Magnetometers   EBEX employs two 3-axis fluxgate magnetometers[6]. Each axis outputs a voltage corresponding to the magnetic field measured along that axis, which enables FCP to reconstruct the azimuth of the magnetometer compared to the local magnetic field (assuming zero roll). The GPS latitude, longitude and the World Magnetic Model is used to align the

---

[5]KVH-DSP 3000
[6]TFS100 from MEDA

local Earth magnetic field with geographical north. The magnetometers measure up to +/-
600 mG with 0.5% precision which corresponds to 12 ' precision on azimuth, but we will
show in Section 3.7 that they need to be calibrated to account for the gondola magnetic
field. Each magnetometer is mounted on a beam extending out of the gondola to minimize
the impact of the gondola magnetic field, and the magnetometer x axis is roughly aligned
with the telescope azimuth.

dGPS The EBEX dGPS[7], consists of four GPS antennas placed in a fix planar config-
uration on an aluminum mount as shown in Figure 3.2. The four antennas measure the
phases of the carrier of the GPS satellites signal, and the Thales processing unit deduces the
attitude of the dGPS mount by comparing the phase differences of the four antennas. The
unit first needs to be calibrated for several hours with Thales proprietary software, in order
for the relative positions of the antennas to be determined. The larger the distance between
the antennas, the more precise is the attitude solution. On EBEX the antennas were placed
~1 m apart, corresponding to ~0.5 ° precision. The dGPS is placed on top of the telescope
to avoid reflections of the satellite signal on the gondola before reaching the antennas. CSBF
also provided a dGPS, similarly placed on the gondola, which communicates with FCP. The
dGPS provide all three attitude angles but were placed on the outer frame and only used
for azimuth. For reasons still not understood the EBEX dGPS failed early in the flight, and
stopped providing any attitude, position or satellite information.

Sun Sensor EBEX has two custom built sun sensors, positioned at the back of the outer
frame so they face the sun when the gondola is scanning anti-sun. They are mounted at
45 ° from each other in order to maximize the total azimuthal coverage. They consist of
pinhole illuminated position sensitive devices (PSD)[8]. The pinhole focuses the incoming sun
light on one bright spot on the PSD, the position of which is dependant on the direction

---

[7]Thales ADU5
[8]Hamamatsu S5991-01

31

of the incoming light. Four electrodes placed on each side the PSD measure the current and transmit the measurements to FCP. The position of the bright spot on the PSD is reconstructed using those currents, and the azimuth and elevation of the outer frame is calculated using the known sun position in the sky and the position of the bright spot on the PSD. Roll is assumed to be zero. Each sensor has a $\sim$45 $^\circ$ field of view.

Encoder An optical rotary encoder[9] is used to measure the rotation of the inner frame with respect to the outer frame. It is located at the trunnion bearing assembly. The encoder is precise to 20 $''$, but it measures the elevation only with respect to the outer frame. We can use the encoder to measure absolute elevation by considering the oscillations of the outer frame a part the measurement uncertainty. For a given outer frame tilt, the encoder is calibrated to the star camera like other sensors. The encoder elevation is also the only measurement used in the elevation control loop (see Section 3.5) due to its reliability and to minimize elevation oscillations.

Clinometer EBEX is equipped with an analog biaxial clinometer used to measure elevation and roll. It consists of a liquid-filled electrolytic transducer. It is precise to 1.2 $'$, but exhibits 1 $^\circ$ of non-linearity over a 50 $^\circ$ elevation range. This response shape is fitted pre-flight to $\sim$6 $'$. The in-flight acceleration of the gondola sloshes the fluid which degrades its precision to $\sim$30 $'$.

3.4   Real-time Attitude Determination

3.4.1   Summary

The real-time attitude determination is a software loop that runs on the flight computers in FCP at 100.16 Hz and uses sensor and gyroscope data to compute the telescope azimuth and elevation at every time step. Horizontal roll is assumed to be zero in order to limit code

---

[9]Gurley Model A25S

complexity, computing time and increase robustness of the attitude solution. Flight data shows that the gondola roll pendulations have an average amplitude of 0.5 °. The code uses a 1D Kalman filter [44], detailed below, to estimate the azimuth $\phi(t)$ or elevation $\theta(t)$ of each sensor, and its associated uncertainty $\sigma(t)$. For simplicity in the rest of this section we only describe the equations for the elevation calculation. Each sensor also has an associated veto that tells the code if the sensor is considered healthy and should be included in the final telescope attitude. This veto is commanded from ground by the gondola operators. The code computes the telescope elevation $\theta_T(t)$ by doing a weighted average of each healthy sensor elevation:

$$\theta_T(t) = \frac{\sum\limits_{sensors} \frac{1}{\sigma^2(t)}(\theta(t) + \delta)}{\sum\limits_{sensors} \frac{1}{\sigma^2(t)}} \tag{3.1}$$

where δ is the sensor pointing offset to the beam mentioned at the beginning of Section 3.3. The sensor offset can be manually commanded from ground or automatically calculated using the star camera attitude. Note that computing each angle of the attitude independently is an approximation, and the full 3D equations will be used in the post-flight pointing reconstruction chapter. It is acceptable because the roll angles are small and because the co-azimuth ($\phi \cos(\theta)$) is used in the equations where necessary.

3.4.2 One Dimensional Kalman Filter

Each sensor provides an elevation θ_s measurement every $dt = 1.0/f_s$, where f_s is the sensor update rate listed in Table 3.3. In between sensor measurements, the gyroscope rotation rate ω around the elevation axis is integrated to estimate the sensor elevation $\theta(t)$. The gyroscope rate white noise σ_ω, and the uncertainty of each sensor measurement σ_s, are hard-coded into FCP. When integrating gyroscope rates, the sensor elevation $\theta(t)$ and its variance $\sigma(t)^2$ are propagated as follows:

$$\theta(t + \Delta t) = \theta(t) + \omega \Delta t \tag{3.2}$$

$$\sigma^2(t + \Delta t) = \sigma^2(t) + (\sigma_\omega \Delta t)^2 \tag{3.3}$$

When a new sensor measurement θ_s is available at time t, the same variables are updated as follows:

$$\theta(t) = \frac{\frac{1}{\sigma^2(t)}\theta(t) + \frac{1}{\sigma_s^2}\theta_s}{\frac{1}{\sigma^2(t)} + \frac{1}{\sigma_s^2}} \tag{3.4}$$

$$\frac{1}{\sigma^2(t)} = \frac{1}{\sigma^2(t)} + \frac{1}{\sigma_s^2} \tag{3.5}$$

3.4.3 Gyroscopes Bias

The gyroscopes exhibit slow varying 1/f noise in their rate measurements, called a bias. If not accounted for, this systematic error in the rate measurement integrates into a growing attitude error when integrating the gyroscope rate as in Equation 3.2. For this reason, the bias of the gyroscopes is calculated by each sensor, by comparing the difference in two consecutive sensor measurements $\Delta\theta_s$, to the gyroscope integrated attitude $\sum_t \omega(t)\Delta t$ in between those measurements. The final estimate on the gyroscope bias at every sample in time is obtained by low-passing the sensor consecutive bias measurements and averaging all the low-passed sensor bias measurements together. When evolving sensor attitude in-flight, the bias-corrected rate ω^C is used in Equation 3.2.

3.5 Actuators and Low Level Control Loops

Two DSPs run azimuth and elevation control loops to orient the telescope. The DSP code runs at $\sim$10,000 Hz. FCP provides the DSP with a requested elevation θ^R and a requested

azimuth velocity ω_ϕ^R. The DSPs use that information along with the encoder elevation θ, and the gyroscope azimuth velocity ω_ϕ to operate proportional-integral (PI) loops. No derivative term (D) is used because the system doesn't really need to be damped and overshooting is not an issue.

The elevation control loop works as follows: the DSP software computes the elevation error term $\delta(\theta)$:

$$\delta(\theta) = P(\theta^R - \theta) + PI \int_{t-t_0}^{t} (\theta^R - \theta)dt \tag{3.6}$$

where P, I and t_0 are parameters commandable from the ground. The error term is communicated to a field programmable array (FPGA), where it is turned into a pulse-width modulation voltage (PWM). The PWM is then sent to the elevation motor control box where it is converted to a current to the elevation motor.

The azimuth control loop is done in a similar though more elaborate manner to account for the two azimuthal motors. The current to the reaction wheel, and thus its velocity, is controlled by a similar PI loop on the azimuth velocity error. However the reaction wheel can only exchange angular momentum with the telescope, and as external torques are applied to the gondola the reaction wheel eventually reaches its maximum rotation rate and becomes unable to provide torque to orient the telescope. This is why we also use a pivot motor, which applies torque against the flight train. The goal of the pivot is to keep the reaction wheel rotating at a given requested low velocity, using a P loop. The pivot gives powerful but jerky accelerations, and only kicks in when the reaction wheel can't provide enough torque. A control mode using solely the pivot was also implemented as a safety precaution in case the reaction wheel failed in flight.

3.6 Scanning

3.6.1 Scan Strategy

EBEX is designed to scan a patch of sky roughly 20 °x 20 °, as shown in Figure 3.3. The size of the patch is chosen to be able to observe the CMB power spectrum down to multipole moment l = 20 and the location is chosen to optimize a low dust region and a region that is directed anti-sun during the flight period. To calibrate the instrument, the scan strategy is to observe RCW38, a bright point-like source in the galactic region, twice a day. The gondola raster scans the patch by taking azimuth throws of about 20 °, and stepping up in elevation 1/3 of a beam every two throws, covering a parallelogram area from top to bottom and back up again. The fastest desirable scanning velocity is limited by the ∼12 Hz bolometer time constant. Scanning at a velocity of $0.4\,°\,s^{-1}$, this ensures about 4 measurements of the bolometers per 8 ′ beam size. The scan strategy optimizes cross-linking and ensures uniform coverage of the sky, as shown in Figure 3.3. The entire patch is scanned twice a day, for a total of 22 times during our 11 day flight. As will be discussed in Chapter 4, an issue in the thermal design of the pivot motor control box led to a loss of azimuth control and a revised scan strategy. In the rest of this section, I describe the pre-flight work done to develop and test our scans. This was of limited use during the LD2013 flight because of the motor control box malfunction.

3.6.2 Hexsky

A software tool "Hexsky" was developed for EBEX in C to optimize the CMB and calibrator patches availability given the anti-sun constraints and the elevation constraints (the telescope has an elevation range of 30 ° < elevation < 60 °). For a given launch date and predicted flight trajectory, Hexsky produces a schedule file, which is a series of scan commands based on the time in LST and the telescope latitude, to be executed throughout the flight. All the simulations for our patch coverage, pixel revisit and cross-linking, are based on the
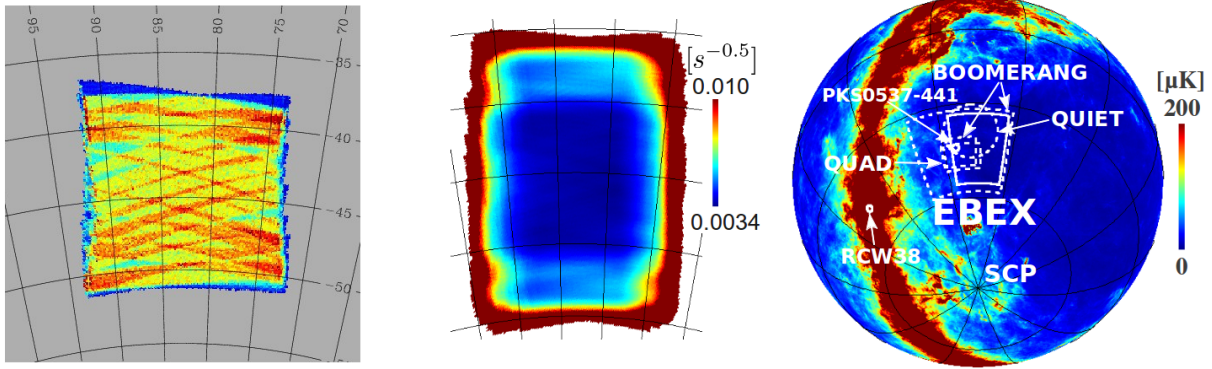
Figure 3.3: *Left*: Hexsky simulation of the coverage of the EBEX patch after 1 day of scanning. Notice the cross-linking. *Middle*: Hexsky simulation of the coverage of the EBEX patch after 11 days of scanning. *Right*: The EBEX scan area as designed pre-flight.

simulated scans by Hexsky. Before flight, several sets of schedule files were uploaded to the flight computer to account for different possible flight trajectories and hence different telescope latitudes.

3.6.3 Scan Implementation

Algorithms

We developed two main scanning commands in FCP to orient the telescope according to the Hexsky simulations. A scan command takes as input scan parameters such as the desired patch center and size, the azimuth scanning velocity, and the number of elevation steps. It outputs at every time step a required elevation position and azimuth velocity transmitted to the low-level control loops. When necessary, the required azimuth velocity is deduced from the required azimuth position through a user-defined P gain commandable from ground. For both scan commands, the scanning algorithm is a state machine consisting of three states:

- *throw*: The gondola moves in azimuth, at constant elevation, until a certain RA defined by the scan parameters is reached. The azimuth scan speed is constant and defined by the scan parameters. The required RA is translated to the corresponding azimuth

using GPS latitude and LST.

- *elevation step*: The telescope is taking an elevation step. The code first determines the desired RA and elevation to reach at the end of the step, given the number of steps already taken and the scan parameters. Once the desired attitude is reached within a user-specified tolerance, the scan goes into the next mode.

- *snap*: The gondola pauses at the end of a throw, in order for the star camera to take an image.

The two scan modes, named "calibrator scan" and "CMB scan", differ by the manner in which the elevation step is calculated. The goal of the calibrator scan is to ensure every detector scans RCW38 and the elevation steps are constant in size because the detectors are evenly spread in the horizontal reference frame. The CMB scans are used to scan the CMB patch and take constant declination steps, which correspond to different elevation step sizes as the two coordinate systems rotate from one another. Note that the scan throws happen at constant elevation and form tilted lines in the equatorial reference frame. This enables cross-linking of the CMB patch, since the tilt is a function of time.

Tuning

The efficiency of the gondola dynamics is determined by the parameters of the various PI loops: the P gain to transform requested azimuth position to requested azimuth velocity, the P and I values of the elevation control loop, and the two P and one I values of the two azimuth control loops. Too large P and I terms lead to overshoots and oscillations around the required destination. Some oscillation frequencies lead to a resonance in the whole system, and we have observed visible shaking of the gondola when improperly tuned. Too small P and I terms lead to delays in the gondola response time and steady-state errors in the desired attitude. In addition, the scan destination tolerances and star camera pause times must also be optimized to spend as little time as possible at scan turnarounds while still achieving the desired scan patterns and acquiring the necessary attitude solutions. Pre-flight testing and

tuning was performed to measure the realistic dynamic motion of the telescope and adapt the Hexsky simulations and flight schedule files accordingly. This is important because if Hexsky simulates scans faster than what the telescope can achieve, it will place new scan commands in the schedule file before the previous patch is entirely scanned, leading to incomplete coverage and patch size. Figure 3.4 shows the gondola measured motion compared to the Hexsky simulated scanning before and after tuning of the control parameters. It is interesting to note that the air density at float is less than 10% of what it is at sea level, making the dynamics of the gondola very different at float and requiring a re-tuning of all parameters once at float.

3.7   Pre-flight Coarse Sensor Calibration

The biggest source of error for real-time attitude determination comes from measuring the angle offset between each sensor and the microwave beam. In practice, this is done through a two step process: the offset between each coarse sensor and a star camera is measured, and separately the offset between the beam and the star camera is measured by scanning an area containing both a visible and a microwave source. In flight, each coarse sensor offset is computed as soon as a star camera solution is available. Before flight, it is necessary to get the best possible measurements of these offsets to ensure reliable pointing at float in the eventuality that the star cameras do not solve real-time, and to provide an attitude guess to the star cameras to obtain the first solution. In this section we discuss the pre-flight coarse sensor to star camera and star camera to beam calibrations, and evaluate the quality of the pre-flight calibrations using LD2013 flight data. The results are summarized in Table 3.4.

3.7.1   Coarse Sensor to Star Camera Offset

This measurement can only be performed once the instrument is in a flight configuration, and all the sensors are mounted in their final position. The telescope is taken to the launch pad
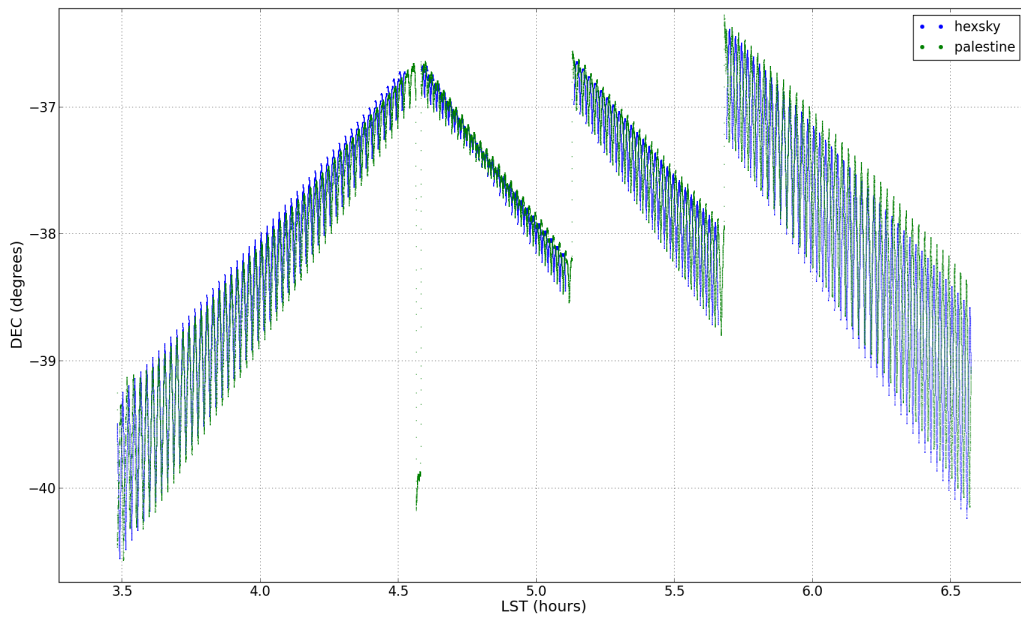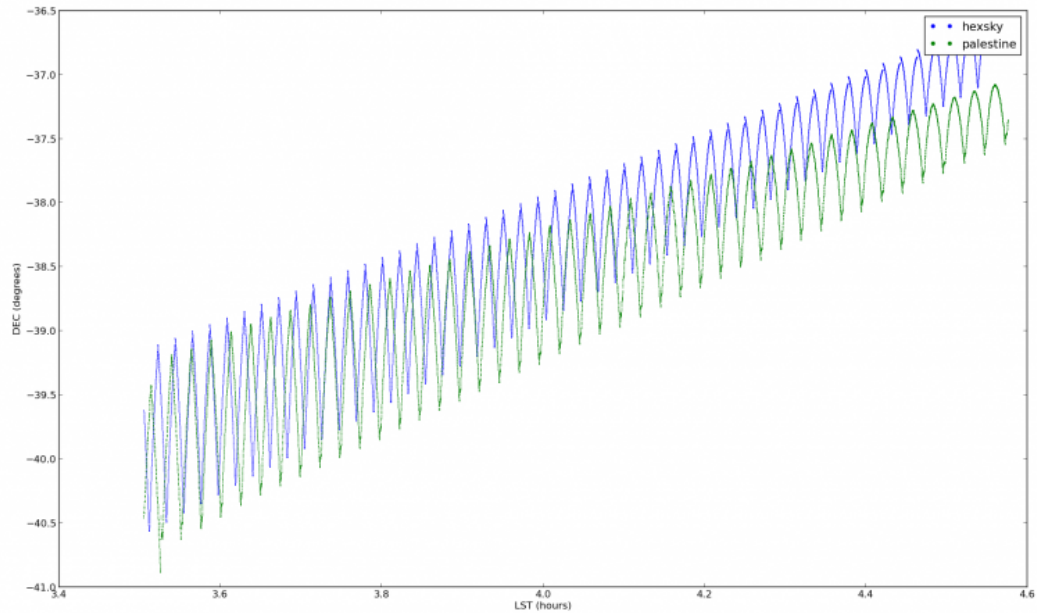
Figure 3.4: Comparison of the attitude (declination angle) from Hexsky simulations (blue) to actual gondola motion (green). The scanning tests were performed inside a high bay during the 2012 integration campaign in Palestine, TX. The top plot shows the comparison before tuning of the control gains. After only 1 hour, the gondola is 0.5 ° behind the simulated motion. The bottom plot shows the comparison after optimization of the control gains.

Sensor	Pre-flight offset (°)	True offset (°)	Difference(°)
magnetometer 0 cross-el	0.2	-1.7	1.9
magnetometer 1 cross-el	1.5	-0.1	1.6
sun sensor 0 cross-el	3.6	0.9	2.7
sun sensor 1 cross-el	-1.5	-1.8	0.3
CSBF dGPS cross-el	227.8	225.6	2.2
EBEX dGPS cross-el	137.9	nan	nan
clinometer el	1.3	1.8	-0.5
star camera 0 cross-el	0.83	0.31	0.5
star camera 0 el	2.51	2.83	-0.3
star camera 0 roll	0.0	0.21	-0.2
star camera 1 cross-el	0.72	0.40	0.3
star camera 1 el	-1.49	-1.10	-0.4
star camera 1 roll	0.0	-0.59	0.6

Table 3.4: Comparison of the angle offsets between each sensor and star camera 1 as computed from the pre-flight calibration and the post-flight reconstructed pointing. For the star cameras, the offset between the star camera and the beam is shown instead.

and aligned in azimuth and elevation such that Canopus (one of the few stars bright enough to be visible during the Antarctic summer) is located at the center of one of the star camera images. The offsets with the two dGPS azimuth, and the clinometer elevation are measured. Note that the encoder elevation offset must be measured when the telescope is hanging, to account for any imbalance of the outer frame. The sun sensors and the magnetometers are first self-calibrated, as described in the following subsections, before their azimuth offsets are computed. Table 3.4 shows that the angle offsets for the coarse sensors are found to better than 3 ° by this pre-flight procedure.

3.7.2 Magnetometer Calibration Procedure

The magnetometers measure the local magnetic field $\vec{M}$ in the horizontal plane and the flight code determines the angle ϕ_m between the field and the magnetometer using :

$$\phi_m = \arctan(\frac{M_y}{M_x}) \tag{3.7}$$

If the only magnetic field present is the Earth field $\vec{E}$, the angle ϕ_m measured is the angle between the magnetometer and the Earth magnetic field. To get the absolute azimuth of the magnetometer, the azimuth of the Earth magnetic field ψ_E at this location must be added. ψ_E is determined by the World Magnetic Model[10]. Magnetic fields $\vec{C}$ produced by the instrument (and fixed in the instrument frame), as well as differential gains G between the x and y-axis of the magnetometers, produce systematic errors in the azimuth measurements:

$$M_x = G_x(E\cos(\phi + \psi_E) + C_x) \qquad (3.8)$$

$$M_y = G_y(E\cos(\phi + \psi_E) + C_y) \qquad (3.9)$$

$$\phi_m \neq \phi + \psi_E \qquad (3.10)$$

Those effects can be calibrated without any external sensors by rotating the magnetometer 360 ° and fitting the ellipse:

$$(\frac{M_x}{EG_x} - C_x)^2 + (\frac{M_y}{EG_y} - C_y)^2 = 1 \qquad (3.11)$$

The center of the ellipse is a measure of the instrument field and the ratio of the major over the minor axis measures the differential gain. This is done pre-flight for the purpose of the pre-flight sensor offset calibration, and is re-done during ascent when the instrument is in its final configuration and no ground magnetic fields can perturb the measurement. Figure 3.5 shows 1.4 ° improvements in the accuracy of the magnetometer azimuth after this procedure is performed during LD2013.

3.7.3   Sun Sensor Calibration Procedure

Several parameters need to be measured to calibrate and use the sun sensors: the distance between the pinhole and the PSD (see section 3.3.3), the effective length of the PSD active

---

[10]https://www.ngdc.noaa.gov/geomag/WMM/DoDWMM.shtml
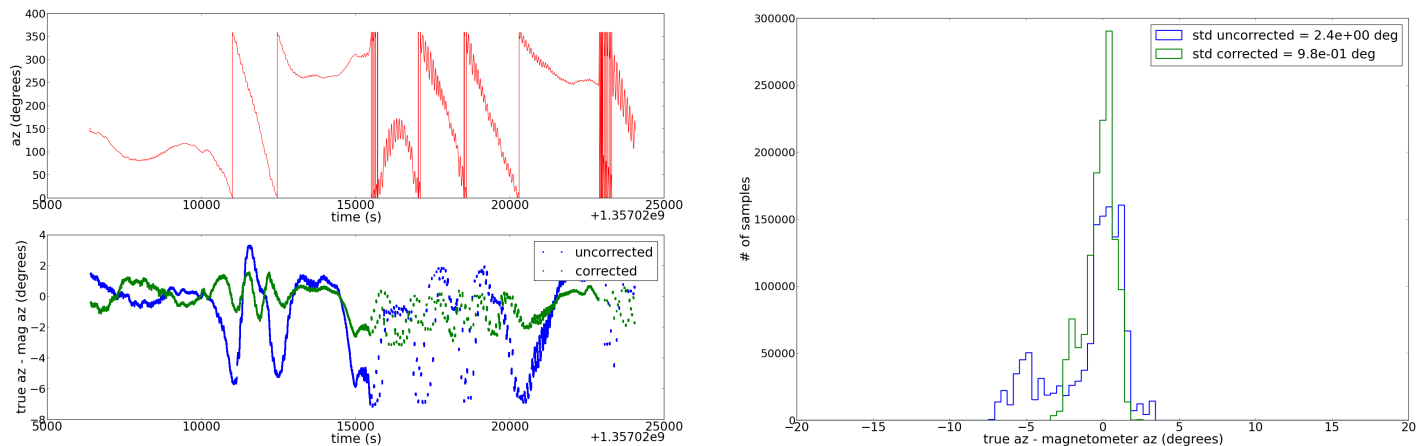
Figure 3.5: Comparison of the magnetometer azimuth with the post-flight reconstructed azimuth. *Left top:* Azimuth plotted against time for a typical 7 hour section of the flight. *Left bottom:* Difference between post-flight reconstructed azimuth and magnetometer azimuth before ("uncorrected", blue) and after ("corrected", green) the ellipse fitting. *Right:* Histogram of the difference between the magnetometer azimuth and the post-flight reconstructed azimuth for that same section. The magnetometer accuracy is improved from 2.4 ° to 0.98 °.

area and the voltage threshold value under which the signal to noise ratio of the measurement is too small and the computed azimuth should not be used . These parameters are computed by setting the gondola on the ground and taking data while letting the sun drift across the sensor. The voltage corresponding to no incoming light is also measured, by covering the sensors. Once these values are computed and uploaded in the sun sensor pointing software, the azimuth offset of the sun sensors to the star camera is computed using the previously calibrated dGPS azimuth (since it is not necessarily possible for the star camera to see Canopus while the sun sensor sees the sun, and the dGPS is the next most accurate azimuth sensor).

3.7.4 Star Camera to Beam Offsets

To estimate the rotation between the star camera and the beam from the ground, a light source and a microwave source need to be scanned simultaneously. Again, this procedure can only be done once the instrument is in its final configuration, in Antarctica. Because

EBEX detectors are optimized for float conditions they saturate when observing sky sources from the ground. As a result this star camera to beam calibration cannot be done on a celestial source. Instead, we place a microwave source alongside an LED, as far as possible from the instrument to minimize near-field effects, and both sources are scanned by the telescope. EBEX can observe at a minimum elevation of 15 °, limiting the options for the placement of the sources. The microwave source used was a Karsltrom source producing a narrow band signal at known frequencies in the EBEX observation bands. In Antarctica, we placed both sources on a cherry picker located $\sim$35 m away. The instrument scanned the sources while hanging from a crane. A map of the microwave source was made using star camera and gyroscope attitude, and the azimuth and elevation offsets between the star camera and the beam were computed. Roll is assumed to be zero. The near-field effects increase the uncertainty on the measured offset to $\sim$ +/-0.5 °.

Chapter 4

2012/2013 Long Duration Flight

4.1 Overview

EBEX launched from McMurdo, Antarctica on December 29th 2012. It circumnavigated the continent taking data during the first 11 days, at an altitude of ~35 km. As predicted, after 11 days the cryogens inside the cryostat were exhausted and the scientific portion of the flight ended. The payload continued its flight for 14 more days, with most systems powered off, until the flight was terminated on January 23rd 2013. Figure 4.1 shows the telescope flight trajectory. Shortly after termination, we recovered the hard drives with over 1 TB of data, along with the light and accessible hardware equipment. The rest of the instrument was recovered a year later.

Overall the flight was successful, and many subsystems performed well. The attitude sensors collected data throughout the flight. The star cameras consistently solved the images real time with minimal intervention. The two cameras combined took 41,262 images, ~80% of which solved. Most of the remaining images are either saturated from looking into the balloon or within 30 ° of the sun. The bolometers recorded data throughout flight, with 977 bolometers successfully tuned shortly after reaching float altitude. The cryo-coolers were cycled five times in flight and the detectors and cold optical elements were maintained at their
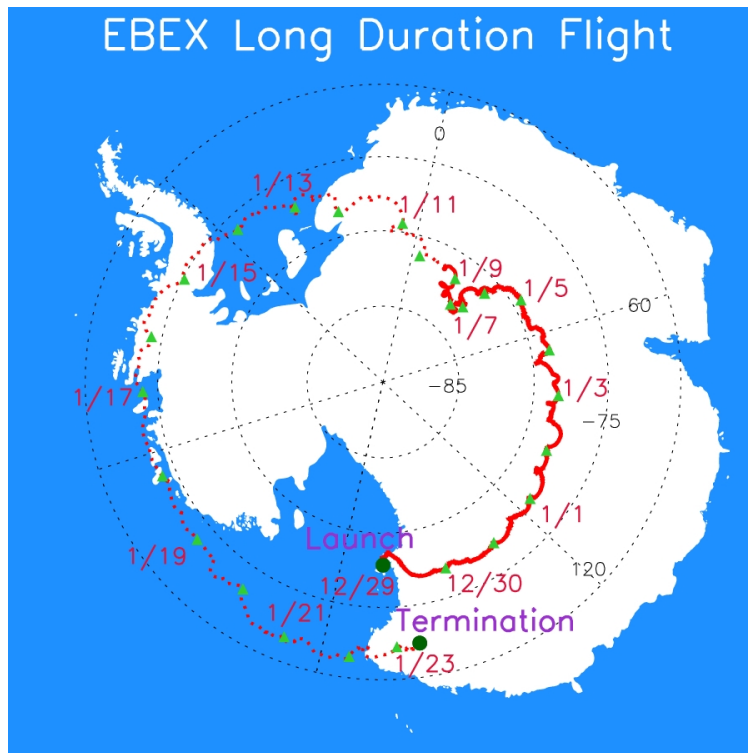
Figure 4.1: Trajectory of the payload during the LD2013 flight, plotted over a map of Antarctica. The solid red line corresponds to the first 11 days during which science data was collected. Circle of constant latitude are plotted in dashed black.

set temperatures. The AHWP worked well, with the SMB achieving over 645,000 rotations during flight. An issue with azimuth control, described in the next section, significantly affected the scan strategy and the total effective observing time.

4.2   Flight Motion

Shortly after launch we discovered that the azimuth motor controller was overheating and causing a motor controller shutdown. The problem was traced to an error in the thermal design of the motor controller mounting. Without active control, the azimuth of the gondola was determined by the rotation of the balloon and the rotational spring constant of the flight train. The resulting motion was composed of slow full rotations (approximately 20 min/rotation) and faster ~80 second period sinusoid motion with amplitude 50 ° - 100 ° peak-to-peak. Figure 4.2a shows typical short and long timescale behavior of the azimuth in flight. With this type of azimuth motion we decided to maintain the gondola at constant elevation of 54 °, chosen to maintain angular distance of ~15 ° from the balloon above, and from the sun at its maximum elevation below. A map of the number of detector samples per pixel (hit map), for all frequency bands, is shown in Figure 4.2b. EBEX scanned a strip of Dec between -67.9 ° and -38.9 °. The total scanned area is 5735 square degrees. By a fortunate coincidence, the natural oscillating frequency of the gondola, 80 seconds, matched the frequency of the design scan strategy: the gondola came to a stop every ~40 seconds, enabling the star cameras to take pictures. In this manner, all the pre-flight work assessing the accuracy of the attitude reconstruction was still relevant to the actual scan pattern of the LD2013 flight. Because of the loss of azimuth control, the telescope azimuth was not constantly kept anti-sun. As a result, the flight computers overheated and periodically needed to be shutdown to cool off. In addition batteries only charged periodically and as a result could not power all bolometers. These two effects significantly reduced the total observing time.
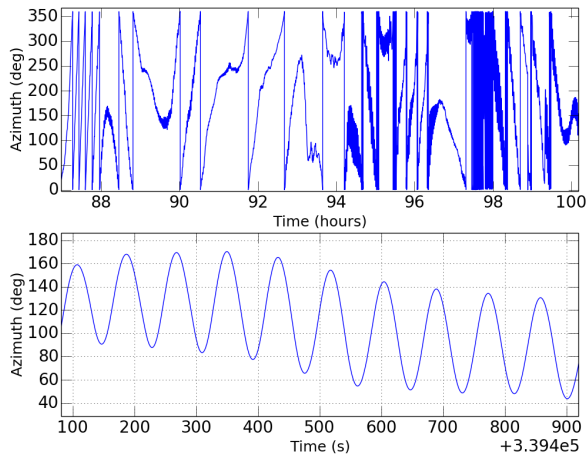
(a) Azimuth Motion
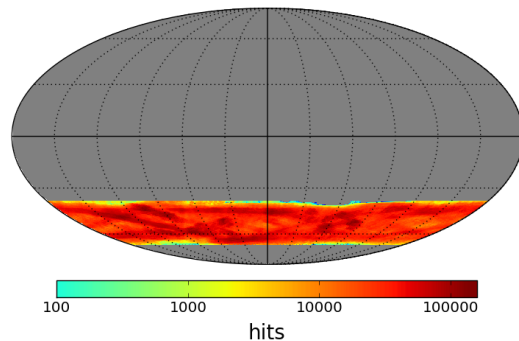
(b) Hit map

Figure 4.2: (a) Typical patterns in the azimuth motion during the LD2013 flight. The top panel shows the long term drifts over ∼12 hours. The bottom panel shows 13 minutes of data, where the 80 second oscillation on top of the long term drifts is visible. Star camera readings are taken every ∼40 seconds when the gondola changes azimuth direction. (b) A map in equatorial coordinates of the number of detector samples per pixel (hit map) for the LD2013 flight from all frequency bands. HEALPix [45] was used for the pixelization scheme and the pixels are approximately 6.9 ′ on a side. A single full rotation of the telescope boresight in azimuth gives a sine wave line bounded by the edges of the Dec strip. Full coverage of the strip is achieved because the phase of this sinusoid changes throughout the day as the Earth rotates and because the focal plane is about 6 ° across in both azimuth and elevation.

Chapter 5

Antarctica Sky Brightness

5.1 Introduction

One of the primary challenges in designing and testing the star cameras before flight is estimating the background noise in the camera images. The noise is dominated by atmospheric scattering of sunlight and is dependant on the payload altitude, attitude, and sun position. This background noise determines what integration time is needed to detect a star of given magnitude when capturing an image, and what integration time saturates the CCD. It therefore drives many of the design decisions for the camera specifications and the scan strategy. The MODTRAN[1] software can be used to simulate the atmospheric propagation of radiation and estimate the power transmitted by the atmosphere in a given direction and frequency band. However, previous ballooning experiments [46] have shown that though MODTRAN can be reliably used to *scale* the atmospheric brightness as a function of altitude, sun position, or telescope attitude, it does not accurately predict the absolute brightness.

In this chapter, we use star camera images taken during the LD2013 flight to estimate the atmospheric brightness for EBEX-like flight conditions. Using scaling factors from MODTRAN, we extrapolate those results and provide sky brightness for various telescope altitudes and elevations commonly encountered in balloon-borne experiments, such that those results

---

[1]http://www.modtran5.com

can be used as guidelines by future balloon-borne experiments. Finally we provide the tools to scale those measurements to other cameras and list the properties of the EBEX cameras. These measurements can be used by future balloon-borne experiments flying over Antarctica.

5.2 LD2013 EBEX Star Camera Measurements

We present here measurements from images taken during the LD2013 EBEX flight. To quantify the power received by the CCD, we define the brightness B of an image as the average number of electrons per second (e^-/s) received in the CCD. The star cameras record the number of counts per pixel N_{ADU}^{pix} and the gain G converts from ADU counts to electrons. The brightness B can be deduced from the image using the equation:

$$B = \frac{N_{ADU}}{t_{int}G} \tag{5.1}$$

where N_{ADU} is the average number of counts/pixel in the image, t_{int} is the integration time for the image and G is the gain of the camera. For the whole LD2013 flight, the gain was set to zero dB which corresponds to $G = 2^{12}/10^5 \, ADU/e^-$ for the EBEX CCD[2]. Note that if the aperture of the camera is changed between images, the brightness B will change. Therefore we define B', the brightness scaled to the open aperture (defined for EBEX by $f_{open} = 1.8$):

$$B' = B\frac{A_{open}}{A_{image}} = B\frac{\pi/4(F/f_{open})^2}{\pi/4(F/f_{image})^2} = B\frac{f_{image}^2}{f_{open}^2} \tag{5.2}$$

The brightness per open aperture B' of the two star cameras are plotted in Figure 5.1 versus the azimuth distance to the sun. The color bar represents different sun elevations. As a side note, most of EBEX images were taken with $t_{int} \sim 300$ ms and $f = 3.0$. In the next section we detail how we can scale those measurements to various telescope altitudes and elevations.

---

[2]Kodak KAF-1603E image sensor
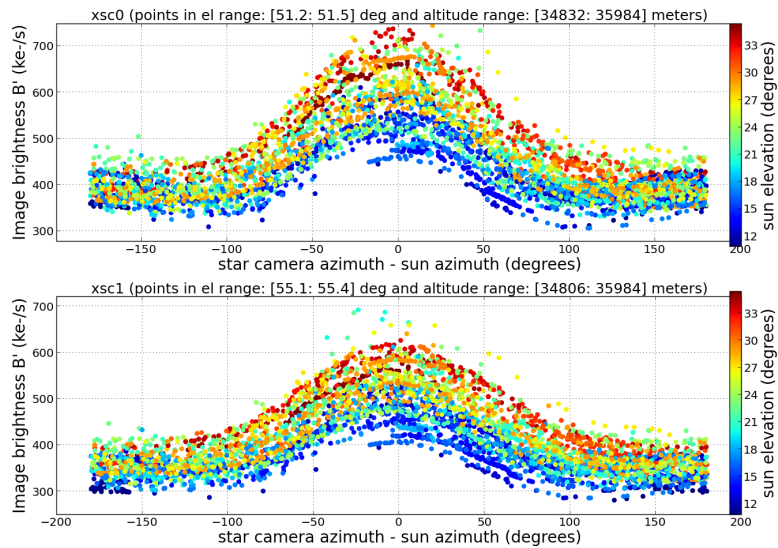
Figure 5.1: Brightnesses B' for star cameras 0 (xsc0) and 1 (xsc1), as a function of the azimuthal distance to the sun. Colorscale corresponds to various sun elevations. The brightness has been scaled to full open aperture (f=1.8). xsc0 points 4° lower than xsc1 in elevation, which explains why the overall brightness observed is larger for xsc0. Data was measured in the altitude range 34.8 to 36 km, and at star camera elevations ∼51° and ∼55° for xsc0 and xsc1, respectively.

5.3 Scaling for telescope elevation and altitude

5.3.1 Scaling by MODTRAN

We use MODTRAN simulations to measure how the atmospheric brightness scales with telescope elevation and altitude. MODTRAN calculates the atmospheric brightness using the following input parameters:

- azimuth angle between the sun and the telescope
- sun elevation
- telescope elevation
- telescope altitude

In Antarctica in the summer, the sun elevation varies between 5° and 35°. We investigate telescope altitudes between 30 and 40 km and telescope elevations between 15° and 50°,

51
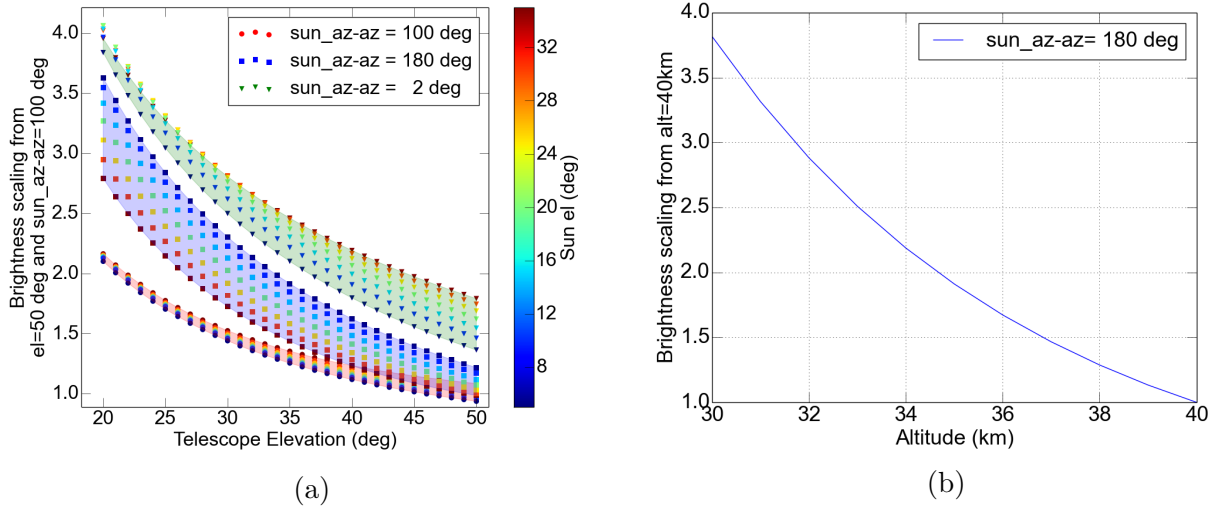
Figure 5.2: (a) Scaling of atmospheric brightness with telescope elevation. The reference used for scaling is the atmospheric brightness at telescope elevation 50°, azimuth between the sun and the telescope 100°, sun elevation 20°. Various configurations are plotted. Notice how the sun elevation has a much bigger effect when the telescope azimuth is anti-sun or towards the sun, compared to when the telescope azimuth is ∼90° from the sun. This is because scattering of the sunlight from the atmosphere into the telescope is most important for orientations pointing directly into the sun or opposite to the sun. (b) Scaling of atmospheric brightness with telescope altitude. The reference used for scaling is the atmospheric brightness at altitude 40 km, telescope elevation 50°, azimuth between the sun and the telescope 180°.

which are typical for balloon-borne instruments. Figure 5.2 shows how the sky brightness scales with telescope elevation and altitude. Note that because the atmospheric brightness depends on the 4 parameters mentioned above, several curves are plotted in Figure 5.2a to try and encompass all cases.

5.3.2   Using scaling factors on EBEX measurements

In this section we use brightnesses B' measured by xsc0 in the LD2013 flight, and MODTRAN scaling, to extrapolate the sky brightness to different telescope altitudes and elevations. This is meant to be used as a guideline for future balloon-borne experiments.

The sky brightness measured is very dependant on the sun position relative to the telescope attitude. In order to provide a range of possible *expected* sky brightnesses, we define a
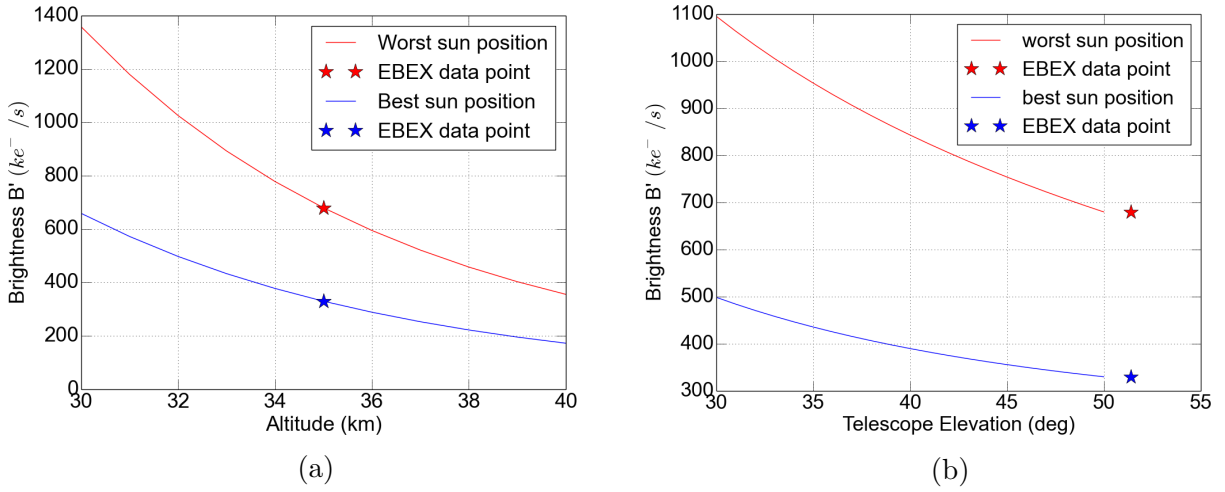
Figure 5.3: (a) Sky brightness B' for various altitudes, at telescope elevation 51.4°. Worst and best sun positions are plotted. The star corresponds to actual EBEX B' measurements using Figure 5.1. (b) Sky brightness B' for various elevations, at telescope altitude 35 km. Worst and best sun positions are plotted. The star corresponds to actual EBEX B' measurements using Figure 5.1

'worst case scenario' (high sky brightness) and 'best case scenario' (low sky brightness) for the sun position. We pick from Figure 5.1 the sun positions corresponding to the highest and lowest sky brightnesses, summarized in Table 5.1. We scale the EBEX measurements, initially taken at altitude 35 km and elevation 51.4°, using the elevation and altitude scalings shown in Figure 5.2. The resulting brightnesses are shown in Figure 5.3.

Table 5.1: Extreme configurations for sun attitude relative to telescope

Case	Sun elevation	Azimuth between sun and telescope	xsc0 B'
Worst	30°	0°	680 e^-/s
Best	15°	100°	330 e^-/s

5.3.3 Summary

Using Figure 5.3, the ranges of brightnesses extrapolated from LD2013 for altitudes [30-40] km and elevations [30°-50°] are summarized in Table 5.2. The numbers stated correspond to $B'(ke^-/s)$, the average brightness at the CCD for a full open aperture (f=1.8).

Table 5.2: Range of expected sky brightnesses for an Antarctic flight

	Best Sun Position	Worst Sun Position
Best Telescope Altitude (40 km) and Elevation (50°)	$\sim$180 ke^-/s	$\sim$350 ke^-/s
Worst Telescope Altitude (30 km) and Elevation (30°)	$\sim$975 ke^-/s	$\sim$2,176 ke^-/s

5.4 Scaling the brightness seen by another camera

In this section we provide tools to scale the results presented above to cameras with different specifications. As defined in the previous sections, the brightness B of an image is the average number of e^-/s that fills the CCD. It depends on the power transmitted by the atmosphere, the aperture and FOV of the camera, the filters in the camera and the CCD efficiency:

$$B = \frac{A \times FOV}{N_{pix}} \int \frac{P(\lambda)\lambda}{hc} f(\lambda)\eta(\lambda)d\lambda \tag{5.3}$$

where N_{pix} is the total number of pixel in the CCD, P is the sky power per unit area, solid angle and wavelength, f is the filter, η is the efficiency of the CCD, A is the area of the aperture and FOV is the field of view. Note that instead of using FOV/N_{pix} one can use the FOV of a single pixel.

To calculate how much brightness another camera with similar filters and CCD efficiency would see, one only needs to scale the FOV, the number of pixels or the area of the aperture (see equation 5.2 for the relation between f-number and area). The well depth of the different CCDs should also be used to compare saturation times. The EBEX cameras have the

following properties, that can be used to directly extrapolate the brightness B from EBEX measurements to another camera:

Camera	Canon EF 200 mm f/1.8
Focal length F	20 cm
Open aperture f	1.8
FOV	2.7 deg x 4.05 deg
Filter	Hoya 25A
CCD	Kodak KAF-1603E
Number of pixels N_{pix}	1036x1024
Pixel size	9 μm
Well Depth	100 ke^-

Chapter 6

Post-flight Attitude Determination

6.1 Introduction

The post-flight attitude reconstruction is accomplished by combining star camera images with gyroscope rate information. As discussed in Chapter 3, the high velocity scan strategy of EBEX coupled to its float altitude (which determines the sky brightness) only permits the star cameras to take solvable images at scan turnarounds, every $\sim$40 s. Between star camera readings the gyroscope rates are integrated to produce accurate relative pointing information. Any non-ideality in the star-camera-gyroscope system integrates into a growing attitude error between star camera images. Though this pointing system is common on balloon-borne instruments, the relatively large amount of time between star camera images on EBEX, coupled to a tight requirement for post-flight attitude accuracy resulted in the need to carefully assess the systematic errors affecting the system. We developed an attitude determination software (ADS) capable of both determining the attitude and producing estimates of relevant pointing system properties such as gyro offsets, gains, etc. In parallel, a simulation pipeline was developed to generate realistic sensor data and test the ADS. In this chapter, we review the attitude accuracy requirements and detail the primary pointing system systematic errors. Then we discuss the ADS and the simulation pipeline, and finally

we present the time-domain results for the LD2013 flight.

6.2 Post-flight Attitude Requirements

Errors in attitude determination can generate B-modes from E-mode signals. We require that spurious B-modes coming from attitude errors be less than 10% of the expected total B-mode signal for r=0.05. To meet this requirement in the map domain, the error on the mean of the attitude inside a pixel of size 2' must be less than $\sim 9''$. In Chapter 7, we will give a detailed description of how attitude errors in the map domain create spurious B-modes and evaluate the spurious B-mode power spectra created by the LD2013 attitude errors.

In this chapter we focus on the attitude errors in the time domain. The EBEX attitude requirement in the time domain is dependent on the scan strategy and the number of repeated hits per pixel. We use our known LD2013 scan pattern to transform the map domain requirement into a requirement on the error over a 40 s azimuth throw. We define the error on a throw as the RMS of the difference between the true attitude and the reconstructed attitude for the set of points between two star camera images. Given our LD2013 scan strategy, the map-domain requirement results in an allowable time-domain RMS error of $< 54''$ over a 40 s azimuth slew. Details of this calculation can be found in Appendix A.

6.3 Elements Affecting Attitude Determination

In this section we list the elements of the pointing system that affect the accuracy of the reconstructed attitude. We characterize the effect of each element on the attitude determination and motivate which properties of the pointing system need to be determined by the ADS. If relevant, we detail the steps taken in the design of the system to minimize the magnitude of the systematic error.

6.3.1 Gyroscope Noise

Gyroscope rate noise translates into a growing attitude error when gyroscope rates are integrated. To assess the effect of this noise, we break it up into a white noise component and a slow varying drift (or bias) component. It is common to assess the noise on different timescales using the Allan variance method [47], which determines the spread in the consecutive means of many chunks of data, as a function of the chunk length τ. The Allan variance measurement and the white noise specification for each EBEX gyroscope are shown in Figure 6.1.

The uncertainty on the attitude coming from integrating gyroscope white noise grows like $\sqrt{N}$, where N is the number of integrated samples. The RMS on the reconstructed attitude of a 40 s throw coming from the EBEX gyroscope rate white noise is $\sim 11\ ''$, as is detailed in Appendix B. This is well under our requirement of RMS = 54 $''$, which is why those gyroscopes were chosen.

We then evaluate the effect of bias on the reconstructed attitude. Figure 6.1 shows that the bias is constant on timescales of $\tau \simeq 200$ seconds. Thus between two star camera readings, the bias is well approximated as a constant systematic offset in the gyroscope rate reading. The gyroscope specifications state that the bias can have values up to $20''\,\mathrm{s}^{-1}$. A constant offset of $20''\,\mathrm{s}^{-1}$ in the gyroscope rate integrated during 40 s between star camera images translates to an RMS error of $516''$, which is well above the EBEX requirement. The ADS therefore needs to determine the bias offset as a function of time throughout the flight. We do this on timescales of 40 s. Details on how this is done are given in Section 6.4.

6.3.2 Gyroscope - Star Camera Alignment

The attitude is determined in the star camera frame. To integrate the attitude between star camera solutions, we need to know the rotation rate of the star camera frame, but what we measure is the rotation rate around each gyroscope axis. Each custom-built gyroscope box is comprised of three independent single-axis gyroscopes. We thus need to know the trans-
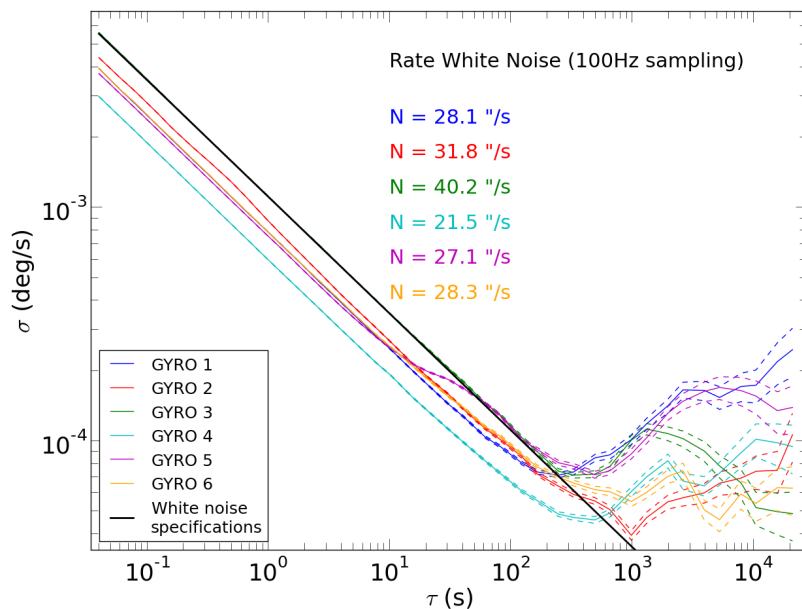
Figure 6.1: Allan variance measurement for all six EBEX gyroscopes. The test is performed by measuring the gyroscope rates for 24 hours while the gondola is immobile on the ground, facing south (to minimize measurements of the earth rotation rate). For a given chunk length τ, the RMS of the difference in the mean of consecutive chunks is plotted. The white noise level, measured by the offset of the -1/2 slope on short timescales, is given for each gyroscope and can be compared to the $40\,''\,\mathrm{s}^{-1}$ specification, plotted in black. The curves' lowest point indicate the timescales on which the bias varies, roughly 200 seconds.

formation matrix (TM) between the star camera frame and the frame defined by the three gyroscopes. An error in this TM means that in between images the attitude is integrated around an erroneous axis, and this translates into an attitude error that grows linearly with integrated angular distance. We break up the TM in two constituent transformations:

- An "orthogonalization" matrix O, which transforms the three independent single-axis gyroscopes into an orthogonal frame. It depends on three small angles, called the misalignment angles.
- A rotation matrix R, which rotates the now orthogonal gyroscope frame into the star camera frame. It depends on three angles, called the rotation angles.

Those six angles (three rotation angles & three misalignment angles) are parameters that are determined by the ADS (one set of angles needs to be determined for the whole flight). The conventions used for the angles can be found in Appendix C. Note that we design the system such that the misalignment angles are small: the gyroscope boxes are precision machined such that outside surfaces are mutually parallel and orthogonal to within 4.9'.

How well do these parameters need to be determined? The mapping between uncertainties on those six angles and the error on the attitude is dependant on the specific motion of the telescope and thus not easily analytically calculated. For a rough one dimensional estimate, an error of $\sim$4.5' on the orientation of a gyroscope around which the telescope rotates translates into an error of 54" in the reconstructed attitude for a 40 s, 20° throw. Section 6.5 details the simulation used in order to determine how well the parameters need to be measured to achieve the required attitude accuracy. Details on how the ADS finds all six angles are given in section 6.4.

6.3.3 Gyroscope Gains

The manufacturer's specifications on the gyroscope gains are calculated for the entire +/- $350° \, \mathrm{s}^{-1}$ rate range, and are not constraining enough for the regime in which we use the
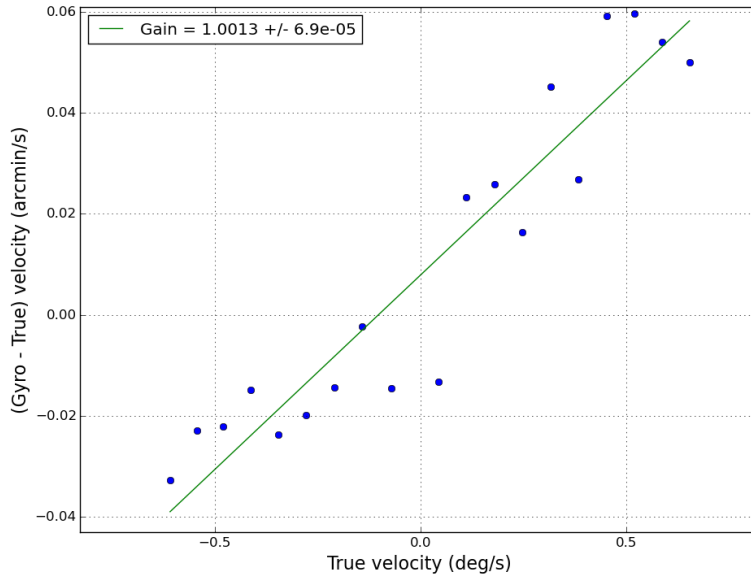
Figure 6.2: Measurements of a gyroscope scale factor. The gyroscope is aligned with the elevation axis, and the inner frame is rotated at various rotation rates. "True" rotation rate is measured with the elevation encoder. The y-axis shows the difference between the gyroscope rate and the encoder rate (blue points). The gain (shown in the legend) is measured using the slope of the best-fit line (green), and adding 1.

gyroscopes (+/- $2°\,\mathrm{s}^{-1}$). Therefore the scale factor of each gyroscope is re-measured by aligning it with the gondola's elevation axis and moving the gondola in elevation at various velocities. The scale factor is found by calculating the best fit line between the encoder and the gyroscope velocities, see Figure 6.2. Amongst the six gyroscopes, scale factors found range from 1.001 to 1.005 with a measured uncertainty of 7e-5. Simulations show this characterization is sufficient for the attitude requirement to be met. Therefore the gains are not fit by the ADS, and instead the measured value for each gyroscope gain is used in the ADS.

6.3.4 Magnetic Fields

The fiber optic gyroscopes are sensitive to ambient magnetic fields, which alter the rotation rate reading, so we shield them by taping them in overlapping strips of Metglas[1]. The rate dependence on the magnetic field was then tested using a Helmotz coil. The sensitivity to magnetic fields was reduced from $17.2'' \, \text{s}^{-1} \, \text{G}^{-1}$ to $2.3'' \, \text{s}^{-1} \, \text{G}^{-1}$ by the Metglas. On the LD2013 flight trajectory, the earth magnetic field's horizontal component is at maximum 200 mG. For 20° azimuthal throws, this translates to a maximum field change of 68 mG, or a change in the gyroscope bias of $0.16'' \, \text{s}^{-1}$. This is smaller than the uncertainty to which the bias is fit by the ADS for every throw and this effect is ignored from hereafter.

6.3.5 Summary

The elements affecting attitude reconstruction are gyroscope noise (white noise and bias), star camera to gyroscope TM, gyroscope gains, and magnetic fields. In Section 6.5, we describe how we simulate star camera and gyroscope data, including how we simulate most of the systematic effects. Ultimately only the gyroscope bias and the star camera to gyroscope TM are insufficiently determined by pre-flight measurements, and require in-flight determination by the ADS.

6.4 Attitude Determination Software

The goal of the Attitude Determination Software (ADS) is to estimate the telescope attitude given star camera and gyroscopes measurements. As shown in Section 6.3, the ADS also needs to determine the gyroscope bias values and the six angles of the TM. Figure 6.3 shows an overview diagram of the ADS. It is separated into an Unscented Kalman Filter (UKF) [48] and a least squared optimizer (LSO). The UKF estimates the telescope attitude and the gyroscopes bias given a fixed TM. It then outputs a metric to assess the quality of the

---

[1]http://www.metglas.com/assets/pdf/2714a.pdf

reconstructed attitude. The LSO uses this metric to find the correct TM. The UKF is run many times until the LSO converges on a TM with error on the angles less than a few arcminutes. In the next subsections we review the UKF and the LSO in more details.
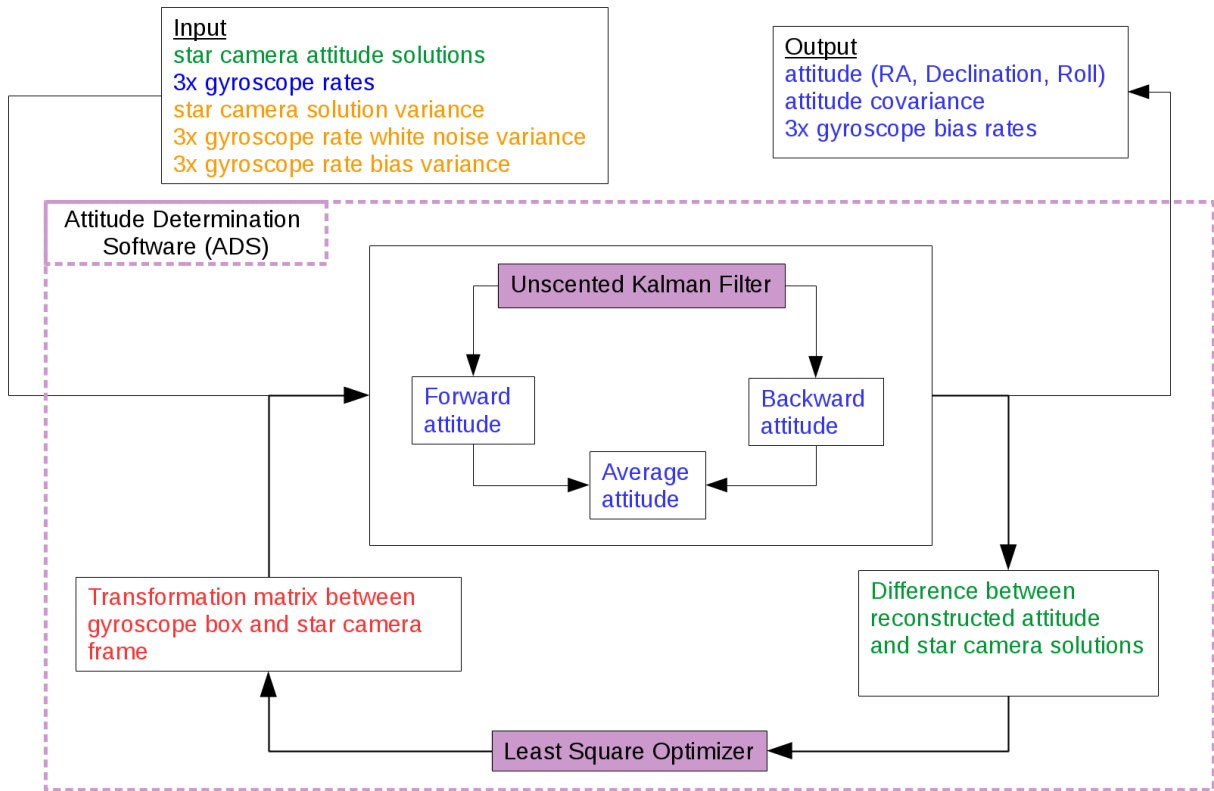
Figure 6.3: Diagram of the ADS. The filled purple boxes denote the two main constituent codes. The blue text represents arrays of data with identical lengths at sample rate 100.16 Hz. The green text represents much smaller arrays with length equal to the number of star camera solutions. The orange text designates single numbers, and the red box is a 3x3 matrix with six independent parameters.

6.4.1 Unscented Kalman Filter

We adapted an UKF (pykalman[2]) from Python to C++ to determine the attitude for EBEX. Kalman filters [44] have been extensively described in the literature to estimate the state (the attitude) of linear systems given a set of noisy measurements (gyroscope rates and star camera solutions). The algorithm works in a two step process: the "prediction" step and the "update" step.

In the "prediction" step, the filter integrates gyroscope rates (ω_1, ω_2, ω_3) at time t to produce an estimate of the next attitude and its covariance at time $(t+1)$, using Equations 6.1 and 6.2 determined by Euler angles kinematics [49]:

$$\begin{pmatrix} \dot{\theta} \\ \dot{\psi} \\ \dot{\phi} \end{pmatrix} = \begin{pmatrix} c_\psi & 0 & s_\psi \\ s_\psi t_\theta & 1 & -c_\psi t_\theta \\ -\frac{s_\psi}{c_\theta} & 0 & \frac{c_\psi}{c_\theta} \end{pmatrix} R^{-1} O^{-1} \begin{pmatrix} \omega_1 \\ \omega_2 \\ \omega_3 \end{pmatrix} \tag{6.1}$$

$$\begin{pmatrix} \theta_{t+1} \\ \psi_{t+1} \\ \phi_{t+1} \end{pmatrix} = \begin{pmatrix} \theta_t \\ \psi_t \\ \phi_t \end{pmatrix} + \begin{pmatrix} \dot{\theta}_t \\ \dot{\psi}_t \\ \dot{\phi}_t \end{pmatrix} \times dt \tag{6.2}$$

where c, s and t stand for cosine, sine and tangent and (θ, ψ, ϕ) are the attitude Euler angles for Dec, Roll and RA. Note that this is the inverse of equations 6.6 and 6.5 used in the next section to simulate gyroscope rates given the Euler rates. R and O are the previously described rotation and orthogonalisation matrices.

Equation 6.1 is highly non-linear with respect to the attitude (θ, ψ, ϕ). Kalman filters are designed to estimate the predicted state using linear equations. In our case it is thus necessary to use a generalization of Kalman filters in order to propagate the attitude and the covariance. The UKF provides a good balance between Extended Kalman Filters, which linearize the system to first order, and full Monte Carlo simulations, which take significantly

---

[2]https://pykalman.github.io/

longer to run. To propagate the attitude and the covariance, the UKF uses a deterministic sampling technique known as the unscented transform [50] to pick a minimal set of sampling points around the current attitude, using the current covariance matrix. These points are propagated through the full non linear Equation 6.1. The next attitude and covariance are computed using the mean and covariance of the propagated points. The attitude covariance grows as subsequent gyroscope samples are integrated between star camera measurements.

When a new star camera solution is available, the "update" step is performed. The attitude is updated using a weighed average of the integrated attitude (IA) and the new star camera reading. When the star camera solutions are good, this weighted solution is dominated by the star camera measurement. The error on the attitude drops, and the process is repeated on the next throw. Figure 6.4 shows a diagram of how the reconstructed attitude and covariance matrix grow with time between two star camera readings:
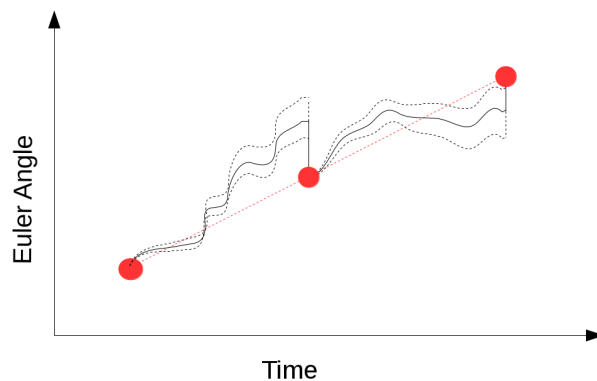
Figure 6.4: Schematic of the reconstructed attitude between star camera solutions, for a single Euler angle and integration in the positive temporal direction. The red dots are the star camera solutions. The red dashed line is the true attitude. The solid black line is the reconstructed attitude – it forms a random walk around the true attitude because we integrate gyroscope noise. The dashed black line corresponds to the uncertainty on the reconstructed attitude. It grows with integrated gyroscope rates, and collapses when new star camera solutions are available.

Section 6.3 showed that the gyroscopes bias must be fit by the ADS in order for the EBEX requirement to be met. Finding this additional parameter is possible because every new star

camera reading provides an accurate measurement of the current attitude. The attitude integrated from the previous star camera reading can be compared to the new reading, and information on the gyroscope bias can be deduced by comparing those two measurements. A bias value is fitted for every throw and every gyroscope in this manner. This is achieved by modifying the UKF state (called up to now the attitude because it was holding only the Euler angles) to be a six parameter vector including three Euler angles as well as three bias values, and updating the UKF equations accordingly:

$$
\begin{pmatrix} \dot{\theta} \\ \dot{\psi} \\ \dot{\phi} \end{pmatrix} = \begin{pmatrix} c_\psi & 0 & s_\psi \\ s_\psi t_\theta & 1 & -c_\psi t_\theta \\ -\frac{s_\psi}{c_\theta} & 0 & \frac{c_\psi}{c_\theta} \end{pmatrix} R^{-1} O^{-1} \begin{pmatrix} \omega_1 + b_1 \\ \omega_2 + b_2 \\ \omega_3 + b_3 \end{pmatrix} \tag{6.3}
$$

$$
\begin{pmatrix} \dot{b_1} \\ \dot{b_2} \\ \dot{b_3} \end{pmatrix} = \begin{pmatrix} 0 \\ 0 \\ 0 \end{pmatrix} \tag{6.4}
$$

At every time step, the UKF provides an estimate of the six parameter state (θ, ψ, ϕ, b_1, b_2, b_3) , as well as an estimate of the 6x6 covariance matrix of the state.

Finally, because this analysis is performed after flight, the UKF is run both forward and backwards in time. When run forward, the uncertainty on the attitude grows with time, and is largest right before the next star camera reading is included in the solution. When run backward, the uncertainty grows in the inverse temporal direction. The forward and backward attitudes are weighted together to form the average attitude, for which the uncertainty is largest mid-throw (between star camera readings). The weights used to do the average are the inverse of the forward and backward covariances output by the UKF.

6.4.2 Least Square Optimizer

A non-linear least square optimizer (Levenberg-Marquardt) (LSO) is used to find the six TM parameters, which are fixed throughout the flight. The UKF outputs for the whole 11 day flight the set of differences between integrated attitude (IA) and star camera solutions, and this set of differences is used as a metric for the LSO. This procedure has some degeneracy with finding the gyroscope bias offsets which is broken by rotating around all three gyroscopes during the gyroscope 1/f noise stability timescale (ie while the bias is constant). Note that the metric is calculated using the forward (or backward) IA **before** the new star camera reading is incorporated in the solution, in order to provide a non-biased estimate.

The parameters varied in the optimizer are the six rotation and misalignment angles of the TM. The initial guess for the six angles in the LSO is $0°$, and the parameter space allowed is $0.5°$ for misalignment angles, and $10°$ for rotation angles. The reduced parameter space for the misalignment angles is made possible by pre-flight measurements of the orthogonalisation matrix O using a rotary table [51]. The parameter space for the rotation angles is deduced from knowledge of the mounting hardware.

The correct step size in the parameter space for the six angles has to be tuned for the LSO to converge. This is done by trial and error using simulated data. After tuning the step size, it takes on average 90 iterations for the LSO to converge, and each iteration (reconstructing the attitude with the UKF on the entire 11 day flight), takes approximatively 80 minutes on a single 2.1 GHz processor. The code is multi-processed. The UKF is then re-run one last time with the optimized TM. The forward, backward and average attitude and covariance matrices are written to disk. The simulations show us that for scan strategies similar to that of the LD2013 flight, the rotation and misalignment angles are found to within $\sim 3.4'$ on average, and are more accurately found if data with varied motion are input to the UKF.

6.5 Simulations

Pre-flight, a simulation pipeline was developed to test the ADS and ensure it reconstructed the attitude to the desired accuracy. Figure 6.5 shows the data flow between the simulation software and the ADS. The pipeline first simulates attitude time streams, called hereafter the parent attitude. From this parent attitude, simulated star camera solutions and gyroscope rate readings are generated. The systematic effects described in Section 6.3 (gyroscope noise, TM, gyroscope gains) are included in the simulation. The simulated sensor data is then sent to the ADS, which reconstructs the attitude. The attitude output by the ADS can then be compared to the input parent attitude to estimate the quality of the attitude determination. In this section we review the simulation software, detailing how sensor data and systematic errors are simulated.
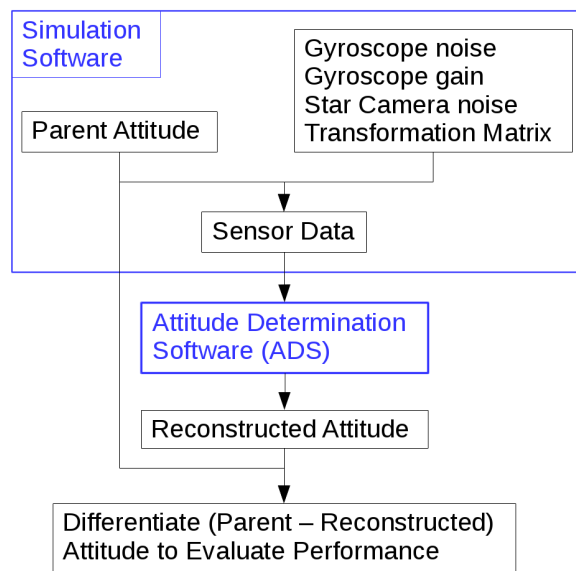
Figure 6.5: Data flow between the simulation software and the ADS.

6.5.1 Generating Parent Attitude

Simulating the parent attitude is the first step to generating simulated sensor data. Before the LD2013 flight, the parent attitude was created by simulating raster scanning with a given

scan speed, azimuth throw amplitude, and elevation step size. After the LD2013 flight, a more realistic parent attitude was generated to account for our loss of azimuth control. We focus on post-flight simulations in this chapter. The parent attitude used is a smoothed, rough estimate of the LD2013 EBEX flight attitude, estimated first using real-time in-flight attitude and after one iteration using the reconstructed attitude.

6.5.2 Generating Sensor Data

The star camera and gyroscopes are simulated for the entire 11 day flight, with the same format as real data from flight.

Star Camera Solutions

A star camera solution consists of an attitude (the three Euler angles RA, Dec and Roll) at a given time corresponding to when the image was taken (the trigger). The first step to simulate star camera solutions is to simulate the triggers. The star cameras only take pictures when conditions of slow velocity and acceleration are met. The same code used in FCP to determine when the star cameras should take images can be used to place the triggers in the simulated data. Alternatively, the simulation software can use actual triggers from flight. The results presented here are based on the latter method. For a given trigger, a solution is generated by adding Gaussian noise to the parent attitude corresponding to the trigger time-stamp. The magnitude of the Gaussian noise is given by the accuracy of the star camera solutions. The magnitude of the star camera errors is estimated by the STARS pattern-matching least-squares algorithm [51] when "solving" the images. Before flight, images were generated by simulating sky noise as discussed in Chapter 5, and star fields using the measured camera point spread function and stellar field simulated from our custom-made catalog [51]. The average error for star camera solutions is 1.5″ in Dec and cross-Dec and 40″ in Roll [52].

Gyroscope rates

The gyroscope rates ω_1, ω_2, ω_3 of each gyroscope need to be computed from the parent attitude. First the parent attitude is differentiated to get the time variation of the Euler angles $\dot{\phi}$, $\dot{\theta}$, $\dot{\psi}$. Then the rotation rates of the body axes of the star camera frame are obtained from Euler angles kinematics [49]:

$$
\begin{pmatrix} \omega_{X_{sc}} \\ \omega_{Y_{sc}} \\ \omega_{Z_{sc}} \end{pmatrix} = \begin{pmatrix} \cos(\psi) & 0 & -\sin(\psi)\cos(\theta) \\ 0 & 1 & \sin(\theta) \\ \sin(\psi) & 0 & \cos(\psi)\cos(\theta) \end{pmatrix} \begin{pmatrix} \dot{\theta} \\ \dot{\psi} \\ \dot{\phi} \end{pmatrix} \tag{6.5}
$$

Finally those star camera body rates $\omega_{X_{sc}}$, $\omega_{Y_{sc}}$, $\omega_{Z_{sc}}$ are transformed into the gyroscope rates ω_1, ω_2, ω_3 using the rotation matrix R and the orthogonalisation matrix O described in Section 6.3.2:

$$
\begin{pmatrix} \omega_1 \\ \omega_2 \\ \omega_3 \end{pmatrix} = O(\delta, \epsilon, \eta) R(\alpha, \beta, \gamma) \begin{pmatrix} \omega_{X_{sc}} \\ \omega_{Y_{sc}} \\ \omega_{Z_{sc}} \end{pmatrix} \tag{6.6}
$$

where δ, ϵ, η are the misalignment angles, and α, β, γ are the rotation angles. These angles will later be fit by the ADS. To simulate the gyroscope data, a value needs to be chosen for these angles. Fiducial values are chosen from a Gaussian distribution with mean $0°$ and standard deviation $5°$ and $0.5°$ for the rotation and misalignment angles, respectively. This corresponds to an upper bound on the uncertainty in these values based on the measured tolerances of the mounting hardware. The conventions used to compute the R and O matrices can be found in Appendix C.

The rates ω_1, ω_2, ω_3 are then multiplied by a scale factor to simulate unknown gains. The scale factor is randomly chosen from a Gaussian distribution with a mean of 1.0 and a standard deviation of 7e-5, corresponding to the uncertainties on the measurements of the scale factors described in Section 6.3.3. Note that unlike other effects simulated, the scale

factors are not fit by the ADS. Instead we used simulations to show that the uncertainties on the measured gains were small enough that the reconstructed attitude satisfies the EBEX requirement without further processing.

Finally we add the gyroscope noise. To simulate realistic noise, the power spectra of the EBEX gyroscopes are computed using the same data taken for the Allan variance measurements. Each power spectrum P is fitted to the model:

$$P = n(1 + (f_{knee}/f)^{\alpha}) \tag{6.7}$$

where n is the white noise level and f_{knee} the critical frequency for drifts, seen to be roughly 5e-3 Hz from Figure 6.1. The α values for EBEX gyroscopes vary between 1 and 1.5. The gyroscope noise is then created by generating a time stream of random Gaussian noise with standard deviation n, taking the power spectrum of this white noise, scaling the lower frequencies according to $(f_{knee}/f)^{\alpha}$, and taking the inverse power spectrum. The noise time stream is then added to the gyroscope rates.

Figure 6.6 shows a comparison between real gyroscope rates from LD2013 and simulated gyroscope rates, showing very good agreement.

6.6 Results in the Time Domain

This section describes the methods available to evaluate the reconstructed attitude and gives the results obtained in the time domain both from simulations and from the LD2013 flight data.

6.6.1 Simulations

The ADS is run on simulated star camera and gyroscope data and outputs reconstructed attitude. Figure 6.7 shows the difference between parent and reconstructed Declination as function of time, as well as parent and reconstructed gyroscope bias for one of the gyroscopes.
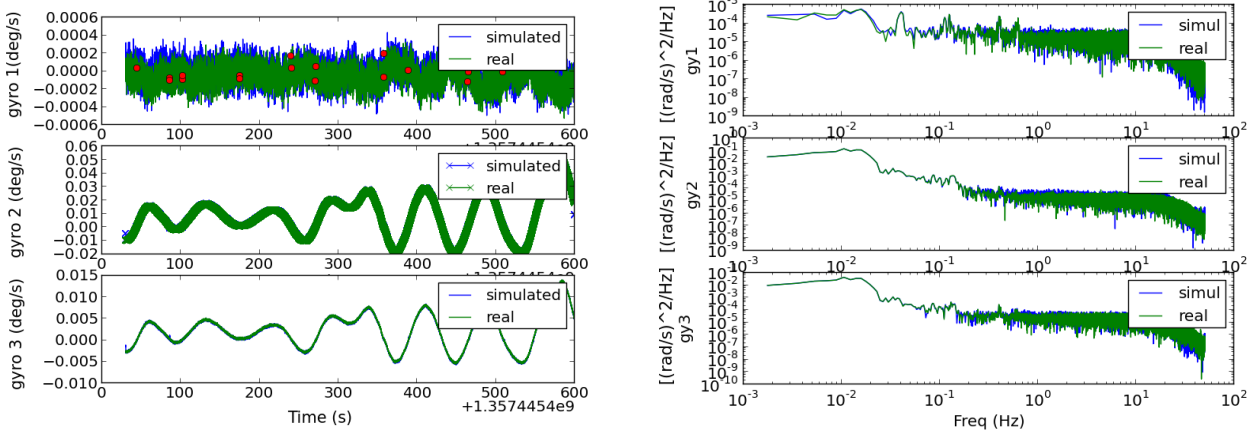
Figure 6.6: Comparison of gyroscope rates from LD2013 flight (green) with gyroscope rates simulated using the procedure described in Section 6.5.2 (blue). *Left*: Rates plotted against time for gyroscopes 1, 2 and 3. The red dots represent the time of the star camera solutions. *Right*: PSD of the gyroscope rates for gyroscopes 1, 2 and 3.

The filter-estimated uncertainty on the average Declination is also plotted in dashed blue for every sample, and it is apparent that the error is largest mid-throw in between two star camera readings. The bias is reconstructed to within $\sim 1'' \, s^{-1}$, and the results presented below show this is sufficient to satisfy the EBEX requirement.

The histogram of the difference between parent and reconstructed attitude (for the average solution) is plotted in blue in Figure 6.8. Dec and cross-dec attitude angles are included. The standard deviation of this histogram, $14.9''$, is to be compared to the EBEX requirement[3] $56''$. This result shows the ADS reconstructed the attitude to the required accuracy. Note that the ADS also provides a covariance matrix of the attitude for every sample. The square root of the average of the Dec and cross-Dec variances, extracted from those covariance matrices, is also shown on Figure 6.8 in green. The two metrics show good agreement.

It is useful to develop a metric to evaluate the reconstructed attitude that does not depend on the parent attitude, so that it can be used on flight data. The covariance output by the ADS can be used, but it is heavily dependant on numbers provided to the ADS by the

---

[3]For the histogram only samples that are part of a 40 s throw were kept to be able to compare the standard deviation of the histogram to the EBEX requirement. Samples pertaining to 40 s throws represents the majority of the data.
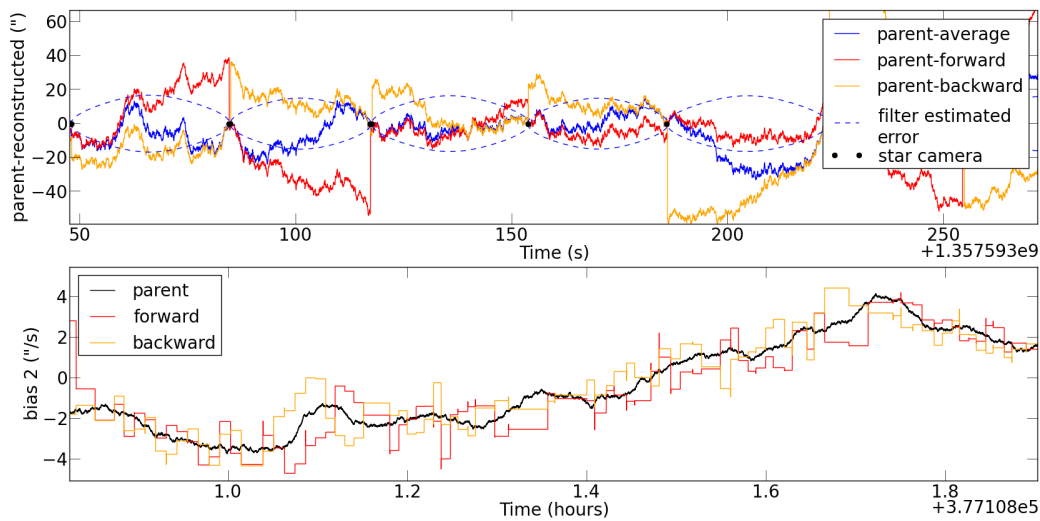
Figure 6.7: Reconstructed attitude and biases using the ADS applied to *simulated* data. **Top panel**: Difference between parent and reconstructed attitude for Declination (forward reconstructed: red, backward reconstructed: orange, average reconstructed: blue). The black dots correspond to star camera solutions. In dashed blue is the ADS estimated uncertainty on the average Declination. **Bottom panel**: The parent (black) and reconstructed (red and orange) gyroscope bias are plotted for gyroscope 2. Note that this plot shows much longer timescales than the top plot. The reconstructed bias is calculated at every star camera reading, hence the step pattern on the plot. The average bias is not plotted as it is not actually used in the reconstruction: the forward attitude is integrated using the forward bias, and the backward attitude the backward bias.
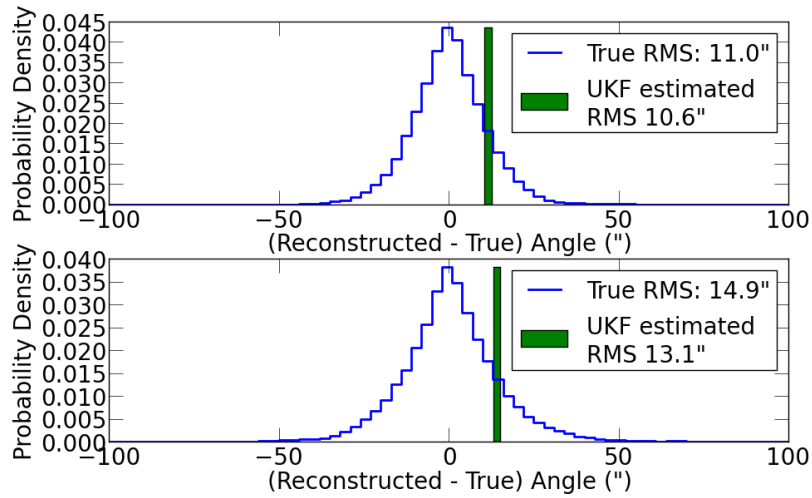
Figure 6.8: Histograms of the difference between parent and reconstructed attitude, for all samples in all 40 second simulated throws. **Top**: White noise reference case. The simulated data includes only gyroscope and star camera white noise. The reconstruction software doesn't fit the gyroscope bias or the TM, which are known. The measured RMS, 11", matches the theoretical case calculated in appendix B. The RMS estimated by the UKF is shown in green. **Bottom**: Full noise case. The simulated data includes gyroscope bias, non-unity TM, and non-unity gains. The reconstruction software fits the gyroscope bias and the TM. The RMS is smaller than the EBEX requirement of 54", though the RMS is larger in the full noise simulation than in the white noise case, as expected.

user: gyroscope white noise value and bias timescale. For this reason, we also develop a new method that relies only on reconstructed attitude and star camera solutions, called the "star camera difference method". Similarly to the LSO metric, the angular distance between the forward or backward IA and the new star camera solution is used to evaluate the error on the IA at the time of the star camera image. As shown in Figure 6.4, this error grows with time since the last star camera solution. Though the majority of star camera images are separated by ~40 s, there are many images separated by shorter periods. Gathering all these images and measuring the error for each image, we plot in Figure 6.9 the size of the forward or backward attitude error as a function of the time to the previous star camera solution, using both the "star camera difference" method and the error reported by the UKF.

This is a fair representation of the error on the forward or backward IA. The error on the average attitude at time t can be computed from the forward and backward errors in the following manner:

$$\frac{1}{\sigma_t^2} = \frac{1}{\sigma_{t_F}^2} + \frac{1}{\sigma_{t_B}^2} \tag{6.8}$$

where F and B stand for forward and backward. Using Equation 6.8 and the data points from Figure 6.9, we compute the RMS of the average attitude over a 40 s throw:

$$RMS = \sqrt{\frac{1}{N} \sum_{t=0}^{t=N} \sigma_t^2} \tag{6.9}$$

The results, shown in the legend of Figure 6.9, are RMS of $11.6''$ for the white noise only simulations and $11.8''$ for the full noise simulations. These numbers are to be compared to the true RMS $11''$ and $14.8''$ computed with the parent attitude, showing this is a reasonable method to compute the error. In the next section we apply this method to the reconstructed attitude from LD2013 flight data.
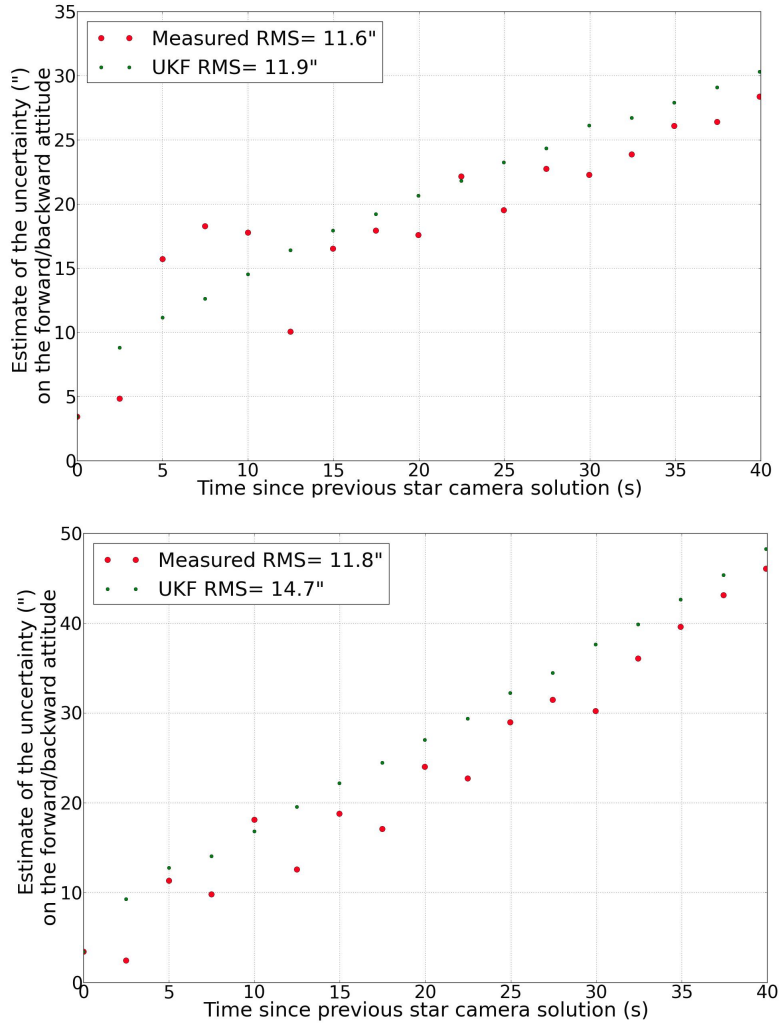
Figure 6.9: Error on the forward or backward attitude as a function of the time elapsed since a star camera reading. Times are binned in 2.5 s bins. Red: for all images within a given bin, the standard deviation of the difference between the IA and the star camera solution is plotted. Green: for all images within a given bin, the average uncertainty reported by the UKF at that time-stamp is plotted. *Top:* White noise only simulation. *Bottom:* Full noise and TM simulation. *Legend*: The error on the average attitude is computed using the plotted data points and Equation 6.8, and the RMS of the average attitude over the entire throw is displayed.

6.6.2   LD2013 Flight

For simplicity only results with gyroscope Box A and star camera 0 are presented here. The gains measured pre-flight are used in the ADS. Figure 6.10 shows the "star camera difference"

method described above, applied to the LD2013 flight reconstructed attitude. The plot is constructed identically to Figure 6.9 in the previous subsection, but using LD flight data instead of simulated data. The error reported by the UKF is also shown in green. Using data in Figure 6.10 and Equation 6.8 we calculate the RMS of the average attitude on a 40 s throw. The result is 15.3", a factor of 3.5 under the EBEX requirement of 54".
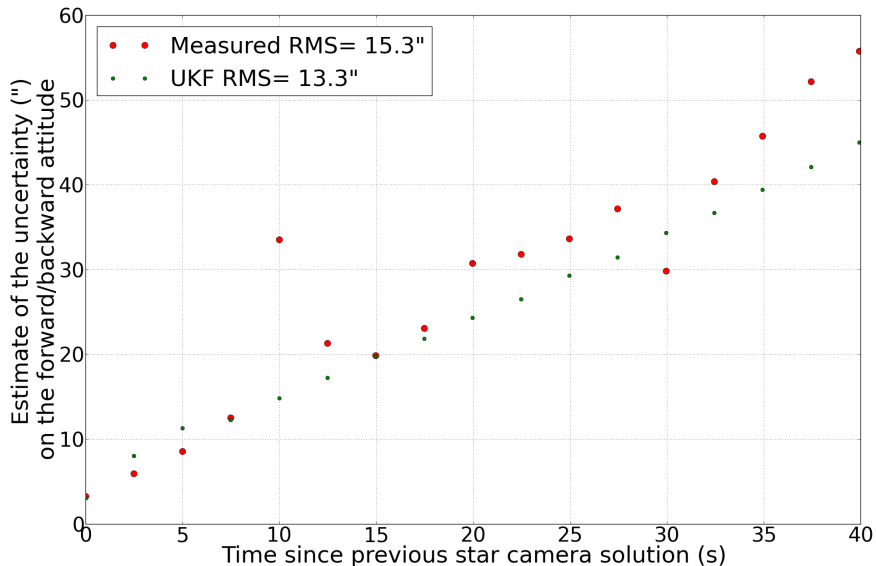
Figure 6.10: Error on the forward or backward attitude as a function of the time elapsed since a star camera reading for LD2013 data. Times are binned in 2.5 s bins. Red: for all images within a given bin, the standard deviation of the difference between the IA and the star camera solution is plotted. Green: for all images within a given bin, the average uncertainty reported by the UKF at that time-stamp is plotted. The error on the average attitude is then computed using the data points and Equation 6.8, and the RMS of the average attitude over the entire throw is shown in the legend.

In the next Section, we evaluate the B-modes induced from attitude errors in the map domain. This is the most accurate tool to determine if our reconstructed attitude satisfies our requirement.

Chapter 7

Effect of Attitude Errors on B-modes

In "Benchmark Parameters for CMB Polarization Experiments" [53], the authors provide a mathematical framework to describe how various instrumental systematic effects distort the CMB temperature and polarization fields and contaminate the B-modes. In this chapter, we rely on this framework to quantify how attitude errors in EBEX contaminate B-modes.

7.1 Theory

In this section we summarize the model developed in [53], applying it specifically to attitude errors and leading to Equations 7.8 and 7.9 which form the basis of our algorithm to calculate the spurious B-mode power spectrum coming from attitude errors.

At a given time sample i, we measure the orientation of the instrument as $\hat{n}$, but the true orientation of the telescope is $\hat{n} + \delta\vec{\theta_i}$, where $\delta\vec{\theta_i}$ represents the attitude error in (RA, Dec) at that sample. We assign to this direction $\hat{n}$ the measurement $\tilde{Q}_i$:

$$\tilde{Q}_i(\hat{n}) = Q(\hat{n} + \delta\vec{\theta_i})$$
$$\simeq Q(\hat{n}) + \delta\vec{\theta_i} \cdot \vec{\nabla}Q(\hat{n}) \tag{7.1}$$

As EBEX scans the same area repeatedly, we assign to a given direction $\hat{n}$ the average of all measurements in that direction:

$$\tilde{Q}(\hat{n}) = \frac{1}{N}\sum_{i=1}^{N}\tilde{Q}_i(\hat{n})$$

$$= Q(\hat{n}) + \frac{1}{N}(\sum_{i=1}^{N}\delta\vec{\theta}_i) \cdot \vec{\nabla}Q(\vec{\theta})$$

$$= Q(\hat{n}) + \delta\vec{\theta}_{map}(\hat{n}) \cdot \vec{\nabla}Q(\hat{n}) \tag{7.2}$$

$$\tilde{U}(\hat{n}) = U(\hat{n}) + \delta\vec{\theta}_{map}(\hat{n}) \cdot \vec{\nabla}U(\hat{n}) \tag{7.3}$$

where N is the number of repeated hits assigned to direction $\hat{n}$ and $\delta\vec{\theta}_{map} = \frac{1}{N}(\sum_{i=1}^{N}\delta\vec{\theta}_i)$ is the mean attitude error in that direction. There is an "averaging-down" of the attitude error in a pixel with repeated passes. Throughout the rest of the chapter we will refer to the attitude error in one pixel as $\delta\vec{\theta}_{map}(\hat{n})$ and use this quantity in our computations.

In a flat sky approximation E and B-modes are defined by:

$$(\tilde{E} + i\tilde{B})(\vec{\ell}) = \int d\hat{n}(\tilde{Q} + i\tilde{U})(\hat{n})e^{-2i\Phi_\ell}e^{-i\vec{\ell}\cdot\hat{n}} \tag{7.4}$$

where $\Phi_\ell = \arccos(\ell_x/\ell)$, ℓ_x being the x component of $\vec{\ell}$. Replacing $\tilde{Q}$ and $\tilde{U}$ with their above expressions, and keeping only first order perturbation terms, the B-modes induced by attitude error become:

$$\delta\tilde{B}(\vec{\ell})_A = \int \frac{d^2\vec{\ell_1}}{(2\pi)^2}\tilde{E}(\vec{\ell} - \vec{\ell_1})\delta\theta_{map}(\vec{\ell_1})((\vec{\ell} - \vec{\ell_1}) \cdot \hat{\ell_1})\sin(2(\Phi_{\ell-\ell_1} - \Phi_\ell)) \tag{7.5}$$

$$\delta\tilde{B}(\vec{\ell})_B = \int \frac{d^2\vec{\ell_1}}{(2\pi)^2}\tilde{E}(\vec{\ell} - \vec{\ell_1})\delta\theta_{map}(\vec{\ell_1})((\vec{\ell} - \vec{\ell_1}) \times \hat{\ell_1}) \cdot \hat{z}\sin(2(\Phi_{\ell-\ell_1} - \Phi_\ell)) \tag{7.6}$$

where $\delta\theta_{map}(\vec{\ell})$ is the Fourier transform of the map of attitude errors, assuming isotropic errors. In practice the errors are not isotropic and RA and Dec directions were considered separately. The "A" and "B" subscripts stand for two distinct effects and should be added up to compute the total B-mode produced. The power spectrum C_ℓ^{SS} of a field S is defined by:

$$< S(\vec{\ell})S^*(\vec{\ell_1}) > = (2\pi)^2 \delta(\vec{\ell} - \vec{\ell_1}) \, C_\ell^{SS} \tag{7.7}$$

To compute the δC_ℓ^{BB}'s induced by our attitude error we square the B-mode Fourier transform in Equations 7.5 and 7.6, and integrate over all ℓ, which gives us:

$$p_A: \quad \delta C_\ell^{BB} = \int \frac{d^2\vec{\ell_1}}{(2\pi)^2} C_{\ell_2}^{EE}(\sigma) C_{\ell_1}^{\theta\theta} [\vec{\ell_2} \cdot \hat{\ell}_1 \sin[2(\Phi_{\ell_2} - \Phi_\ell)]]^2 \tag{7.8}$$

$$p_B: \quad \delta C_\ell^{BB} = \int \frac{d^2\vec{\ell_1}}{(2\pi)^2} C_{\ell_2}^{EE}(\sigma) C_{\ell_1}^{\theta\theta} [(\vec{\ell_2} \times \hat{\ell}_1) \cdot \hat{z} \sin[2(\Phi_{\ell_2} - \Phi_\ell)]]^2 \tag{7.9}$$

where $\vec{\ell_2} = \vec{\ell} - \vec{\ell_1}$, σ is the experiment Gaussian beam width, and p_A and p_B stand for pointing effects A and B. Note that in these equations, $C_\ell^{EE}(\sigma)$ is smoothed over the beam: $C_\ell^{EE}(\sigma) = C_\ell^{EE} \exp{(-\ell(\ell+1)\sigma^2)}$. Given a sky map of attitude errors $\delta\theta_{map}$, we compute the power spectrum of the attitude error $C_\ell^{\theta\theta}$ and we use Equations 7.8 and 7.9 to compute the spurious B-mode power spectrum.

In the previous chapter we stated that the requirement on the EBEX attitude is that the average attitude error in a pixel be less than $9''$. This was calculated by using a simple white noise model for attitude errors, with magnitude $\sigma_{\theta map}$ and coherence scale ℓ_s:

$$C_\ell^{\theta\theta} \simeq \frac{2\pi\sigma_{\theta map}^2}{\ell_s^2} \exp(-\frac{\ell(\ell+1)}{2\ell_s^2}) \tag{7.10}$$

Replacing $C_\ell^{\theta\theta}$ in Equation 7.8, we get:

$$\delta C_\ell^{BB} \simeq \frac{1}{2} \frac{\sigma_{\theta map}^2}{\ell_s^2} \int^{\ell_s} d\ell_1 \, \ell_1^3 \, C_{\ell_2}^{EE}(\sigma) \tag{7.11}$$

For a beam with FWHM=8′, δC_ℓ^{BB} peaks at $\ell_s \sim 500$, and for that value, requiring $\delta C_\ell^{BB} < 0.1 \times C_\ell^{BB}$ is most stringent at $\ell \simeq 1000$ and yields $\sigma_{\theta map} = 9''$.

In the following sections, we use more realistic models for the attitude error map and perform the full integral to compute the spurious B-modes generated.

7.2 Simulations

As described in the previous chapter, a pipeline was developed pre-flight to simulate realistic parent attitude and test the attitude reconstruction. We showed in Chapter 6 how these simulations can be used to construct differences between a parent and reconstructed attitude as a function of time for a simulated flight. The data can then be binned in the map domain, producing maps of the mean attitude error $\delta\theta_{map}$ in each pixel on the sky. The resulting map is shown in Figure 7.1, for the first 12 hours of simulated flight for one bolometer using our pre-flight scan strategy. Note that using more detectors and more integration time decreases $\delta\theta_{map}$, reducing the level of spurious B-mode production. The direction of scanning is apparent in the figure, with smaller errors at the patch edges where star camera solutions occur, and larger errors mid-scan.

Using these maps we compute with the Healpix "anafast" function the power spectrum of $\delta\theta_{map}$, $C_\ell^{\theta\theta}$, plotted in Figure 7.2 for the first 12 hours of simulated flight. This attitude error power spectrum $C_\ell^{\theta\theta}$ is then convolved with the EE power spectrum C_ℓ^{EE} following Equations 7.8 and 7.9 to compute the BB power spectrum δC_ℓ^{BB} created from attitude errors. The results are plotted in Figure 7.3 for the first 12 hours of simulated flight. The "A" and "B" effects are added up to produce a total spurious δC_ℓ^{BB}. The average of the cross-Dec and Dec power spectra is used.

Figure 7.3 shows that in the pre-flight scan strategy, the spurious B-modes produced by
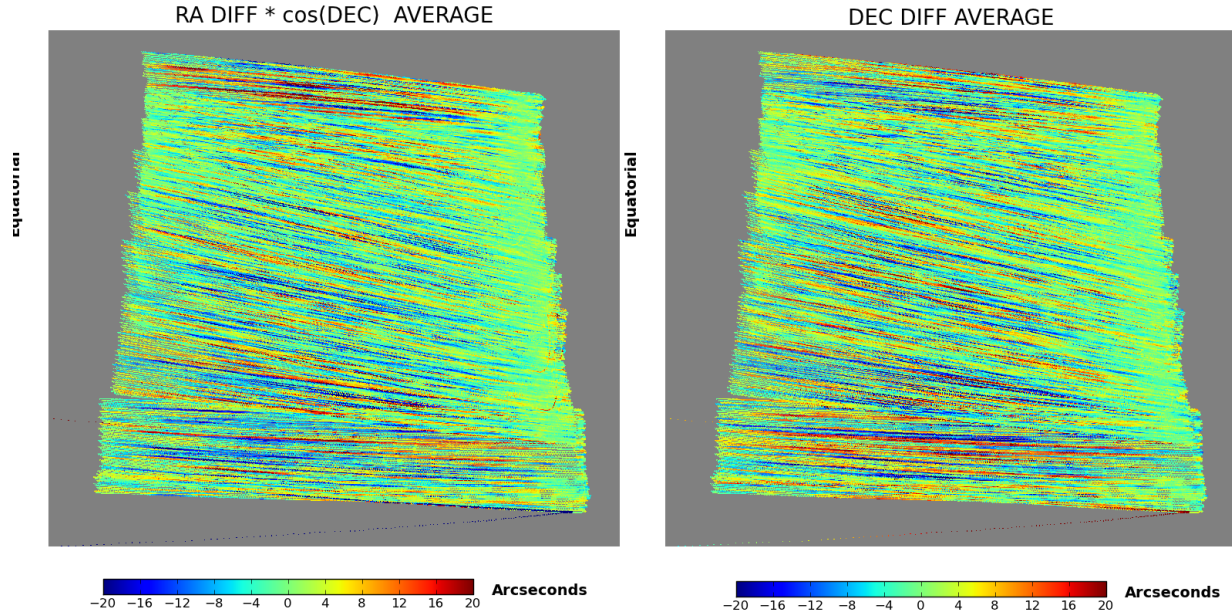
Figure 7.1: Map of $\delta\theta_{map}$, the attitude error for the first 12 hours of simulated flight data for one bolometer (using the pre-flight scan strategy). The maps are generated with Healpix [45], binned and averaged using NSIDE 2048, which corresponds to $\sim$1.7' pixels. *Left:* cross-Dec error. *Right:* Dec error.

one detector over 12 hours are smaller than 1/10th of the expected sky B-modes (for r=0.05) up to $\ell \sim 2000$. With a beam size of FWHM=8 ', EBEX cannot resolve modes higher than $\ell \sim 1500$. Given this result, more realistic simulations including all detectors and the full 11 day flight were not produced because this result represents a conservative upper limit on the error from the entire flight.

7.3 LD2013 Flight Data

In a preliminary analysis, we apply the method described in the previous section to the LD2013 reconstructed attitude for a single bolometer. We list at the end of this section the next steps needed to improve our analysis, including using more bolometers, using the full sky equations and refining our estimate of the map of attitude errors.

To apply the method described in the previous section, we first need to generate an
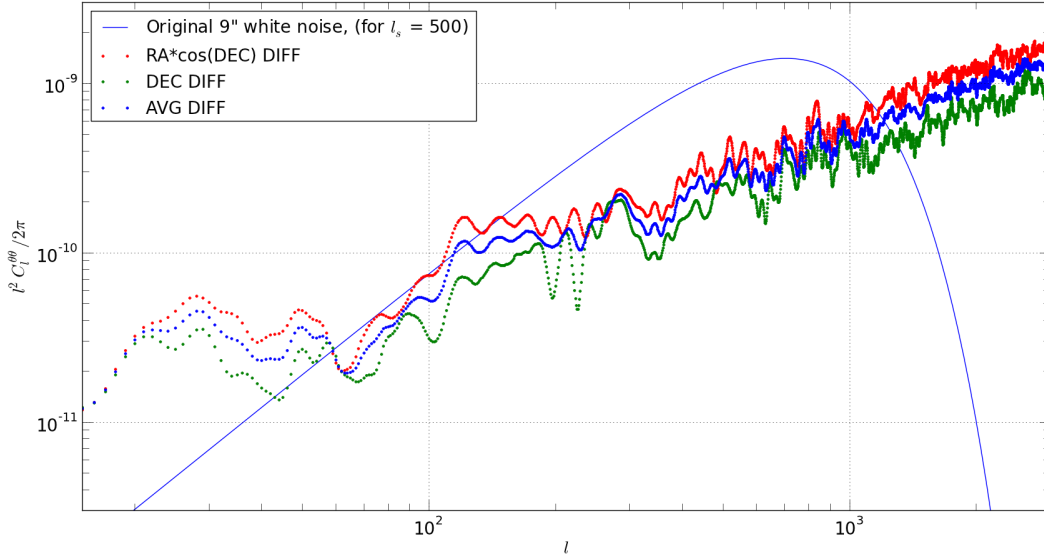
Figure 7.2: Power spectrum of the attitude error for cross-Dec (red diamond), Dec (green diamond) and their average (blue diamond) for the first 12 hours of simulated flight. For reference, the power spectrum of white noise with $\sigma_\theta = 9''$ and coherence scale $\ell_s = 500$ is also plotted in solid blue.

estimate of the mean attitude error $\delta\vec{\theta}_{map}$ in every pixel. To achieve this, we run the ADS on the entire flight until it converges, producing time-streams of reconstructed attitude and its covariance matrix. We then produce a realisation of the attitude error time-stream $\delta\vec{\theta}_i$ using the following method. For every time sample, an attitude error $\delta\vec{\theta}_i$ is generated by sampling a Gaussian distribution with standard deviation obtained from the ADS covariance matrix at that sample. We then bin this time-stream of attitude errors into sky maps, producing the mean attitude error in every pixel, as shown in Figure 7.4.

Using the map of the mean attitude error, we produce the attitude error power spectrum $C_\ell^{\theta\theta}$. Many pixels within our coverage have no hits which biases the estimate of the power spectrum even once we account for the fraction of the sky covered. We estimate and correct the magnitude of the bias in the following manner. We start from a white noise power spectrum with standard deviation equal to the standard deviation of the flight $\delta\theta_{map}$. We generate a noise realisation of this white noise power spectrum, and using our flight coverage
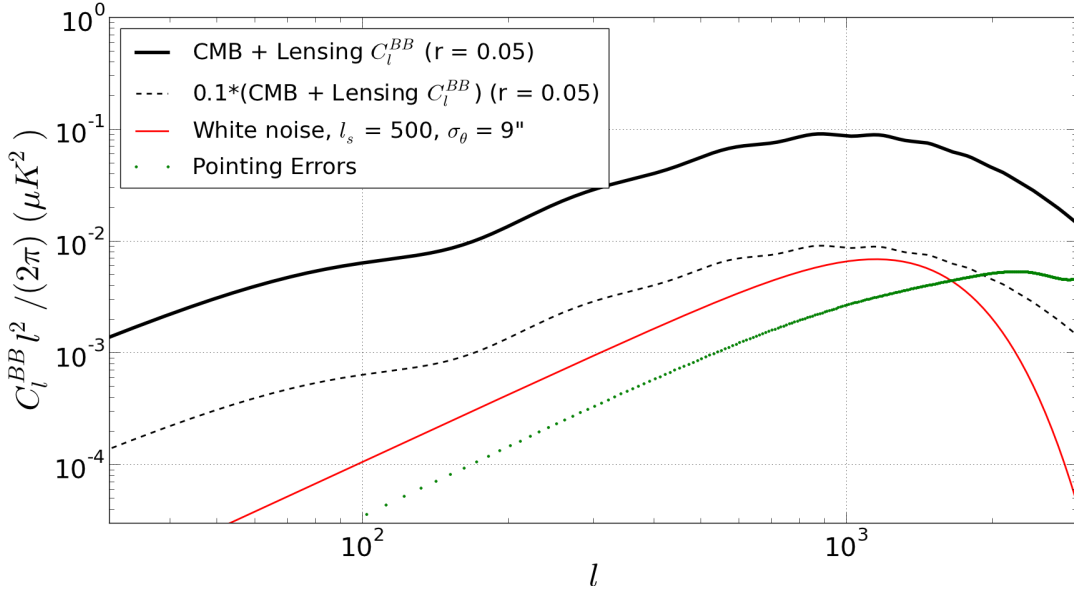
Figure 7.3: Power spectrum of the C_ℓ^{BB} generated from attitude errors (green) for the first 12 hours of simulated flight, compared to the sky C_ℓ^{BB} for r=0.05 (thick black). In dashed black is plotted 10% of C_ℓ^{BB}. For reference, the C_ℓ^{BB} coming from white noise attitude errors with $\sigma_\theta = 9''$ and $\ell_s = 500$ is plotted in red.

we measure the power spectrum of the noise realisation. We compute a scaling factor by comparing the known white noise power spectrum and the measured white noise power spectrum, and apply this scaling factor to the flight power spectrum. The corrected flight power spectrum $C_\ell^{\theta\theta}$ is shown in Figure 7.5.

Finally we compute the spurious B-modes using $C_\ell^{\theta\theta}$ and Equations 7.8 and 7.9, and show the result in Figure 7.6. The spurious B-modes produced are under 1/10th of the predicted sky B-modes (for r=0.05) at all ℓ of interests for EBEX, showing promising preliminary results.

Because this analysis pipeline was developed for pre-flight EBEX characteristics and scan strategy, some elements can be updated to improve the spurious B-mode measurement given LD2013 data. We provide here a list of general items to improve the analysis presented:

- The equations in Section 7.1 are derived using a flat sky expansion. They can be generalized to the spherical harmonic expansion (Appendix A in [53]).

84

- The plots should be updated using the beam size measured from flight: FWHM=15′ (see Section 8.8). This will reduce the leakage of E-modes from higher ℓ.

- The maps of the mean attitude error are underestimated: repeated hits from within the same scan have correlated attitude errors that do not average down. Some correlation function could be implemented, or simply a down-sampling of attitude as a function of scan speed.

- Including multiple detectors in the analysis will increase the number of hits per pixel and decrease $\delta\theta_{map}$ and the amount of spurious B-modes generated. When including multiple detectors, the effect of the star camera equatorial Roll error, which propagates into a detector RA and Dec error, should be included. Preliminary analysis [54] showed that for the EBEX focal plane this is not a major contributor.

A more detailed analysis will be performed using the improvements listed above.
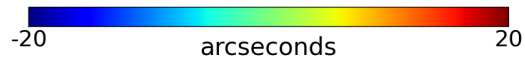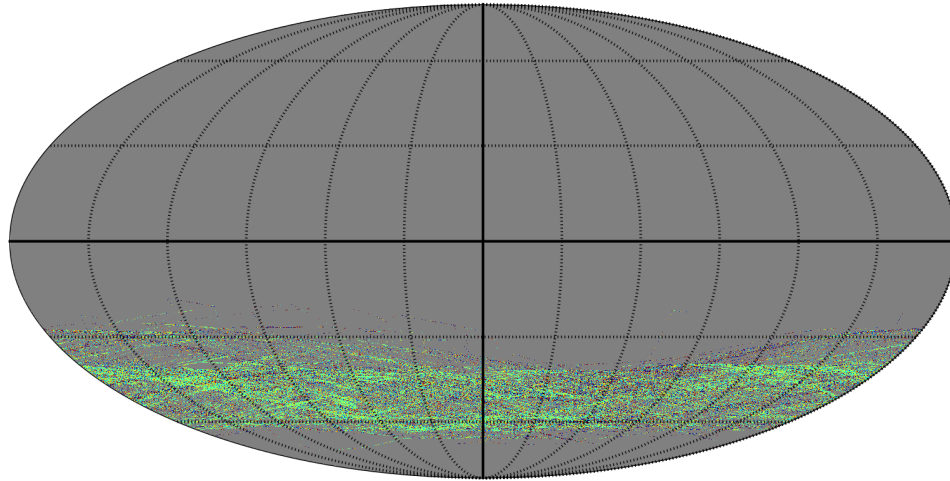
(a) cross-Dec mean attitude error
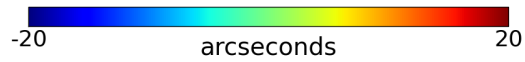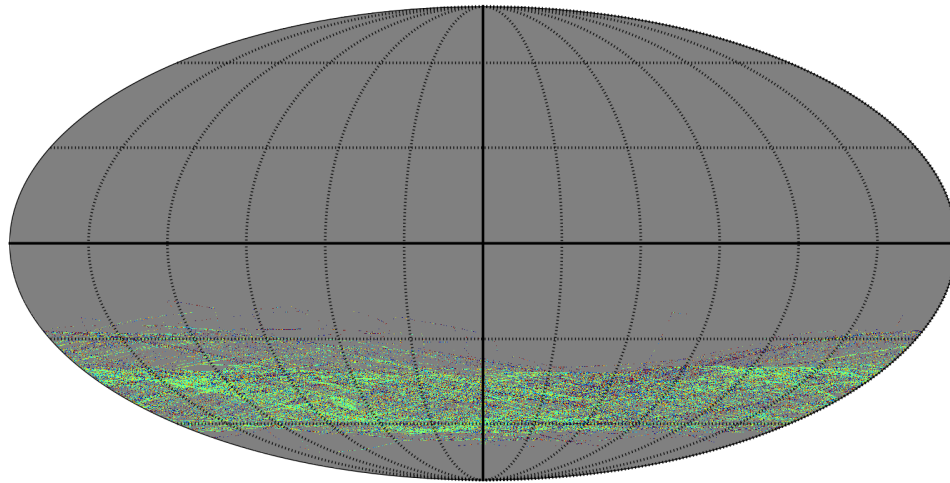
(b) Dec mean attitude error

Figure 7.4: Map of $\delta\theta_{map}$ for LD2013 data for a single bolometer, using NSIDE=2048. For every pixel, the average of all attitude errors within that pixel are plotted for (a) cross-Dec and (b) Dec angles. For every time sample, the attitude error in Dec and cross-Dec is generated by sampling a Gaussian distribution with standard deviation provided by the UKF. The map has a sparse coverage because it includes only one bolometer.
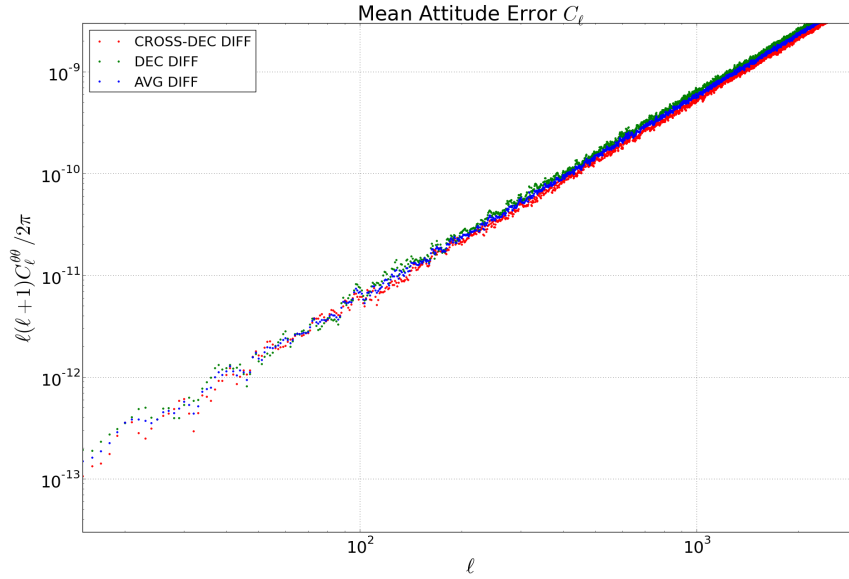
Figure 7.5: Power spectrum $C_\ell^{\theta\theta}$ of the estimated mean attitude error for a single LD2013 bolometer for Dec (green diamonds), cross-Dec (red diamonds) and their average (blue diamonds).
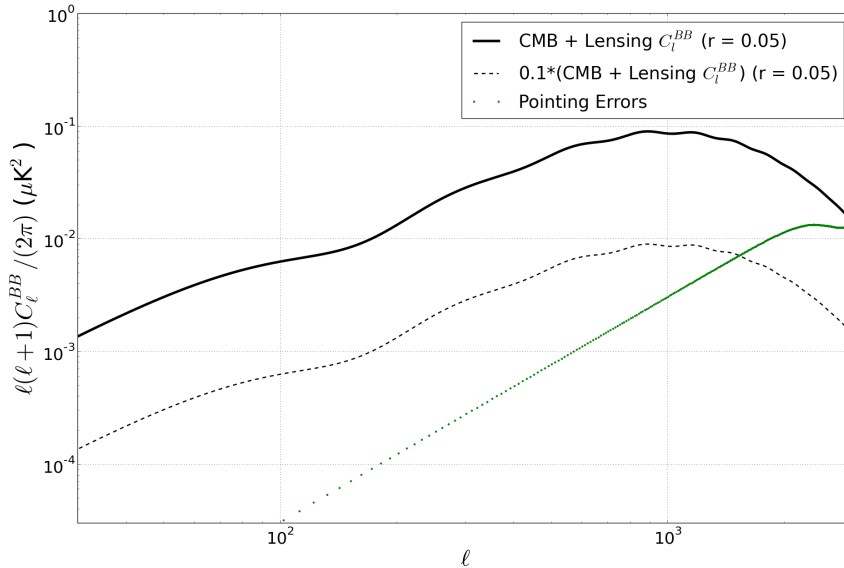
Figure 7.6: Power spectrum C_ℓ^{BB} of the spurious B-modes induced by a single bolometer attitude errors (green diamonds) during the LD2013 flight.

Chapter 8

Data Analysis Pipeline

8.1 Overview

This chapter describes the post-flight data analysis pipeline aiming to reduce the $\sim$1 TB of raw time-streams from the LD2013 flight first into sky maps of temperature and polarization, and ultimately into power spectra of E and B-modes. We focus here on the pipeline stages converting the time-streams to maps. An comprehensive diagram of the pipeline is shown in Figure 8.1. The principal stages are:

1. Flight base creation: ordering the raw time-streams in logical structures.

2. Attitude determination (see Chapter 6)

3. Removal of the HWP-synchronous signal from the bolometer time-streams

4. Transient removal and flagging of invalid samples

5. Calibration of bolometers to temperature units and measurement of star camera to detector rotation angles

6. Filtering and binning bolometers into sky maps of Stokes parameter I, Q and U

7. Removal of I to Q/U leakage (from instrumental polarization (IP), see Chapter 9)

8. Producing power spectra from cleaned, IP-removed maps

I wrote or significantly contributed to all of the above stages, with the exception of the
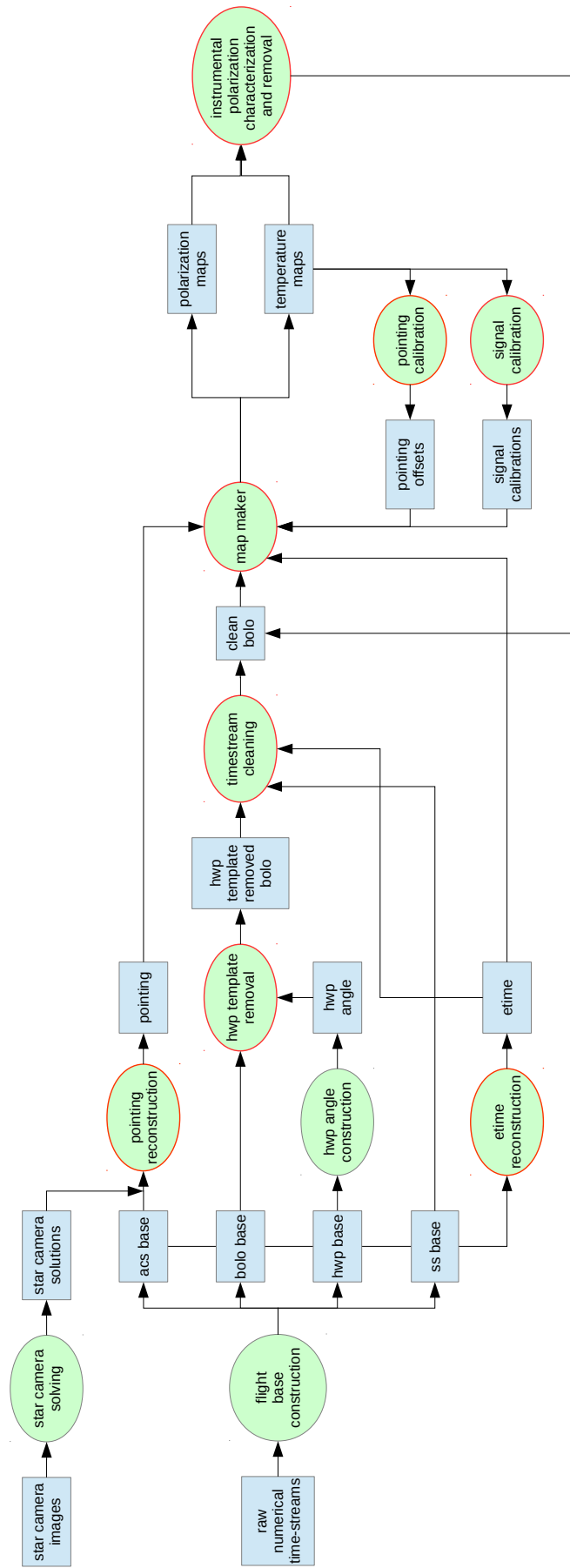
Figure 8.1: Diagram of the analysis pipeline, up to the map-making stage (figure courtesy of Daniel Chapman). Blue boxes correspond to datasets. Green ovals correspond to pipeline stages, executed by a program. All of the programs in the pipeline, as well as the loading and writing of datasets, is performed within the LEAP software framework described in Section 8.4. Pipeline stages outlined in red are reviewed in this thesis.

calibration, and will review most of them in this chapter. The characterization and removal of instrumental polarization required the development of a new technique and is quite involved, so it is described in a separate chapter. This chapter is structured as follows: in the next three sections, we review the data model, the structure of the flight base, and the "LEAP" software framework that we developed to support the analysis pipeline. The following sections will then each cover individual pipeline stages.

8.2 Data Model

The EBEX data model is:

$$s(t) = \frac{1}{2} \left[I^{sky}(t) + Q^{sky}(t) \cos \left[4\gamma(t) + 2\psi(t) \right] + U^{sky}(t) \sin \left[4\gamma(t) + 2\psi(t) \right] \right] \tag{8.1}$$

where I^{sky}, Q^{sky}, U^{sky} are the sky Stokes parameters, γ is the HWP rotation angle and ψ is the telescope Galactic roll angle. This equation is obtained by modelling an ideal HWP and a linear polarizer using the Mueller matrix formalism, as shown in Section 8.2.2. We first define our coordinate system.

8.2.1 Coordinates

In the focal plane, we define the coordinates such that the x axis corresponds to the cryostat symmetry axis, with the $+$ direction corresponding the positive Elevation direction when projecting the focal plane on the sky, as shown in Figure 8.2. The $+y$ direction corresponds to positive Azimuth, and the $+z$ axis points from the cryostat to the sky. In this instrument frame, a positive Stokes Q corresponds to linear polarization along the x-axis, negative Q corresponds to polarization along the y-axis, and positive Stokes U corresponds to polarization 45 degrees between the $+x$ and $+y$ directions.
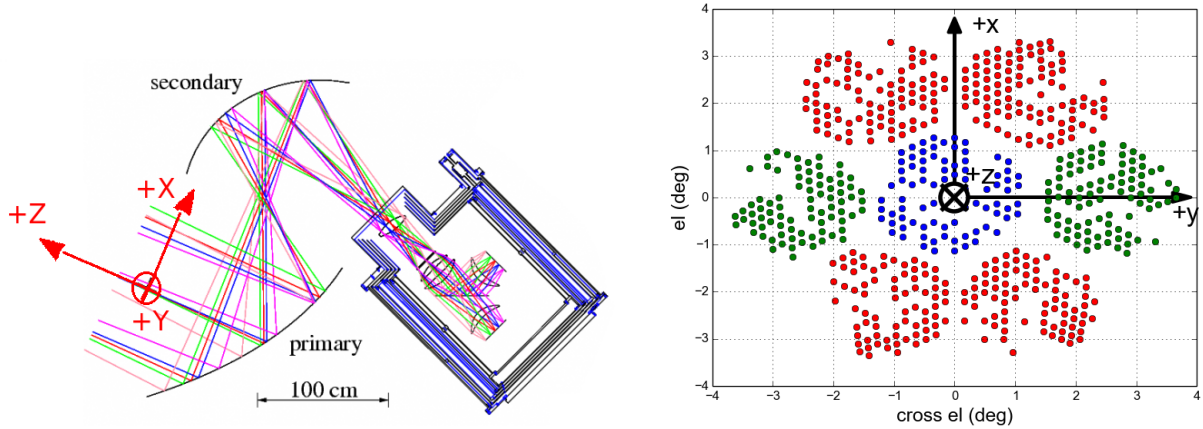
Figure 8.2: Coordinate system used to describe the polarization in EBEX. *Left:* Ray-tracing of radiation as it enters the telescope. *Right:* Projection of a focal plane on the sky. The polarization angle α is 0° when aligned with the x axis, corresponding to positive Stokes Q. α is 90° when aligned with the y axis, corresponding to negative Stokes Q.

8.2.2 Data Model with Ideal HWP and Linear Polarizer

We model the instrument with a simple monochromatic HWP and a linear polarizer. The effect of the AHWP on incoming radiation is to generate a frequency-dependant phase delay that is accounted for in the analysis [55] but not detailed here as it doesn't affect the development of the data model.

Incoming radiation is described by a Stokes vector $\vec{S}_{in} = (I_{in}, Q_{in}, U_{in}, 0)$ where we assume linear polarization only. The HWP acts as a retarder and effectively mirrors the incoming polarization angle around its fast axis. The HWP is rotating at a constant speed and we call γ the time-dependant angle between the HWP fast axis and the x axis. The HWP Mueller matrix is:

$$M_{hwp}(\gamma) \;=\; R(\gamma)M_{hwp}(0)R(-\gamma) \tag{8.2}$$

$$= \; R(\gamma)\begin{pmatrix} 1 & 0 & 0 & 0 \\ 0 & 1 & 0 & 0 \\ 0 & 0 & -1 & 0 \\ 0 & 0 & 0 & -1 \end{pmatrix} R(-\gamma) \tag{8.3}$$

$$= \; \begin{pmatrix} 1 & 0 & 0 & 0 \\ 0 & \cos(4\gamma) & \sin(4\gamma) & 0 \\ 0 & \sin(4\gamma) & -\cos(4\gamma) & 0 \\ 0 & 0 & 0 & -1 \end{pmatrix} \tag{8.4}$$

where the rotation is described by:

$$R(\gamma) = \begin{pmatrix} 1 & 0 & 0 & 0 \\ 0 & \cos(2\gamma) & -\sin(2\gamma) & 0 \\ 0 & \sin(2\gamma) & \cos(2\gamma) & 0 \\ 0 & 0 & 0 & 1 \end{pmatrix} \tag{8.5}$$

Radiation then goes through a linear polarizer, that we will choose aligned with the x axis for this calculation (in reality, it forms an angle β with the x axis that is accounted for in our analysis). The linear polarizer has the following Mueller matrix:

$$M_{lpx} = \frac{1}{2}\begin{pmatrix} 1 & 1 & 0 & 0 \\ 1 & 1 & 0 & 0 \\ 0 & 0 & 0 & 0 \\ 0 & 0 & 0 & 0 \end{pmatrix} \tag{8.6}$$

The output Stokes vector $\vec{S}_{out}$ is then obtained by:

$$\vec{S}_{out} \quad = \quad M_{lpx} \, M_{hwp}(\gamma) \, \vec{S}_{in} \tag{8.7}$$

$$= \quad \frac{1}{2} \begin{pmatrix} 1 & \cos(4\gamma) & \sin(4\gamma) & 0 \\ 1 & \cos(4\gamma) & \sin(4\gamma) & 0 \\ 0 & 0 & 0 & 0 \\ 0 & 0 & 0 & 0 \end{pmatrix} \begin{pmatrix} I_{in} \\ Q_{in} \\ U_{in} \\ 0 \end{pmatrix} \tag{8.8}$$

The detectors are only sensitive to power (the Stokes I parameter) and therefore the data model is:

$$s(t) \quad = \quad I_{out} \tag{8.9}$$

$$= \quad \frac{1}{2} \left(I_{in} + Q_{in} \cos(4\gamma) + U_{in} \sin(4\gamma) \right) \tag{8.10}$$

$$= \quad \frac{1}{2} I_{in} \left(1 + P_{in} \, \cos(4\gamma - 2\alpha_{in}) \right) \tag{8.11}$$

where we used the usual definition for the polarization fraction $P = \sqrt{Q^2 + U^2}/I$ and the polarization angle $\alpha = \frac{1}{2} \arctan(U/Q)$.

The previous description is valid in the instrument frame. To reconstruct the Stokes parameters in the sky frame, we must account for the telescope galactic Roll ψ. We adopt the WMAP conventions [11]: the polarization that is parallel to the Galactic meridian is Q > 0 and U = 0. When the x-axis of the telescope is aligned with the Galactic meridian, the telescope Galactic Roll ψ is 0°. The updated equations in the sky frame are:

$$s(t) = \frac{1}{2} \left(I_{in} + Q_{in}^{sky} \cos(4\gamma + 2\psi) + U_{in}^{sky} \sin(4\gamma + 2\psi) \right) \tag{8.12}$$

$$= \frac{1}{2} I_{in} \left(1 + P_{in}^{sky} \, \cos(4\gamma - 2\alpha_{in}^{sky} + 2\psi) \right) \tag{8.13}$$

Further refining the data model, the bolometer time-stream contains noise n, but also a HWP-synchronous signal that we model as a sum of harmonics of the HWP rotation frequency f_{hwp} (see Section 8.7.1):

$$s(t) = \frac{1}{2} I_{in} \left(1 + P_{in}^{sky} \cos(4\gamma - 2\alpha_{in}^{sky} + 2\psi)\right) \tag{8.14}$$

$$+ \sum_{n=1}^{n=20} A_n \cos(n\gamma) + B_n \sin(n\gamma) \tag{8.15}$$

$$+ n(t) \tag{8.16}$$

8.3 The Flight Base

The flight base refers to the LD2013 dataset as it was structured after flight. Real-time, the flight computer program (FCP) receives and writes files (called "framefiles"), of length 30 min to 1 hour, mixing multiple channels (for example 'altitude' and 'azimuth') within a single file. The raw data comes from 59 asynchronous streams, each with one of four distinct sampling rates:

- 1 ACS stream: it contains ACS data, timing, and housekeeping information from other subsystems. The data is sampled at 100 Hz.
- 2 HWP stream: it contains the HWP encoder data and timing used to reconstruct the HWP angle. The data is sampled at 3050 Hz.
- 28 board streams: each board contains 64 bolometer signal and timing. Boards are asynchronous. The data is sampled at 191 Hz.
- 28 slow-streamer (SS) boards: each board contains housekeeping information for each of the bolometers, and timing. Boards are asynchronous. The data is sampled at 1 Hz.

After flight, we re-organise the data using the Dirfile standard [56]. A Dirfile is a file-system based database for time-ordered binary data. Each Dirfile is a directory in which each

94

channel (ex: 'altitude') is written to disk in a separate file in its native binary format. For each of the 59 streams listed above, and for each section of continuous, uninterrupted data, we create a Dirfile. The resulting structure of the flight base is shown as an example below for the ACS stream, with '\' indicating normal folders and [D] indicating Dirfiles:

```
acs\
  segmentA\
    subsegment0\ [D]
        channel1
        channel2
        ...
    subsegment1\ [D]
    ...
  segmentB\
    subsegment0\ [D]
    ...
```

A "segment" represents data taken between two intentional shutdowns of the experiment. They last 3 to 20 hours. The shutdowns were necessary as the flight computers were periodically exposed to sunlight due to our lack of azimuth control, and overheated. The segments are named with the convention YYYY-MM-DD–hh-mm-ss at which they start. Within a segment, there can be one or more sections of continuous data called "subsegments". These are the Dirfiles and contain the channels to load. Multiple subsegments can occur within a segment because of unintentional, short duration reboots. A similar structure exists for the data in each board, ss board, and HWP board. The process of creating the flight base is discussed in more details in [51].

8.4 The LEAP Software Framework

8.4.1 Motivation

The analysis team consists of 10-20 collaborators spread over multiple institutions and each contributing software code to the various pipeline stages outlined in Figure 8.1. Most of these programs require similar tools, such as loading and writing EBEX formatted flight

time-streams, flagging invalid data, removing transients and filtering time-streams, transforming coordinates or fitting simple functions. To avoid duplicating work and to speed up the analysis, I developed, along with another graduate student Daniel Chapman, a software framework in Python to write the analysis pipeline: the Long duration Ebex Analysis Pipeline, or LEAP. It consists mainly of applications ("apps"), which are pieces of software corresponding to a pipeline stage, and libraries which are a common set of software tools used by many apps. A style guideline also ensures all collaborators' code is easy to understand. To date LEAP has been the main analysis pipeline for EBEX and used by more than a dozen collaborators. It is stored in a repository on a server at Columbia University.

8.4.2 Structure

The main LEAP directory is structured as follows.

apps This directory contains all pipeline stages (as well as other apps) such as attitude determination, calibration, or map making. Each app has an associated directory located in the apps directory, containing the software files (with the app code) and the parameter files to run the app. Individual pipeline stages will be discussed in more details in the following sections.

lib This directory ("lib" for libraries) contains all the common tools used by apps, organized in folders such as "time_domain_processing", "map_making", "units", etc. We briefly summarize here the major library functions.

- i/o_management (input/output): this library manages loading and writing of EBEX data. It loads all the channels requested by the user in a memory-efficient manner, iterating the loading by segments and bolometers. Data can also be loaded in smaller sections of user-defined length to limit memory usage. It writes newly created time-ordered datasets into Dirfiles with the same format as the flight base. To perform those

96

tasks, the library organizes the loaded data into a logical custom-made class called a "Dataset", which calls other libraries to perform background operations like interpolating the attitude to the bolometer sampling, or rotating the star camera attitude into each detector frame.

- chunking: chunking functions are part of the i/o library and use flagging libraries, as well as user defined preferences, to "chunk" up the arrays in smaller sets of continuous valid data. This is important for any operation that does not support "nan", like Fourier transforms.

- leap_multiprocessing: LEAP multiprocessing functions are built around the Python multiprocessing library and make it easy for the user to parallelize jobs.

- leap_app: this library contains code that all apps inherit with basic administrative app functionalities such as logging, timing, or creation of time-stamped output directories for the app output data.

- time_domain_processing: this library contains functions to flag, identify and remove transients, and filter data.

- mapping: this library contains functions to bin data into weighted maps and produce temperature or polarization maps.

- geometry: this library contains functions to rotate the star camera attitude into each detector attitude and convert between various coordinate systems.

- numerical: this library contains functions to measure noise, power spectra, and fit Gaussian histograms.

output   This directory is the location where all apps write their output data. Nothing inside that folder is saved on the repository as the data commonly generated is too large to be saved on a repository. Each app, when writing some output data to disk, will automatically create in this 'output' directory a folder named by time-stamp and app name in which it will write its data. This directory is designed to be a temporary storage space.

resources   This directory is used to store experimental parameters such as frequency bands, bolometer time constants, detector rotations with respect to the star camera, etc.

ldb_data   This directory is used to place links to the location of the data on the computer. The LEAP i/o management library uses those links to find the location of the data. This is useful because different laboratories might have different conventions as to where data is typically stored on a computer. In addition, it is useful to be able to rapidly switch between different datasets, for example real LD2013 flight data and simulated data. This is possible by creating two folders within the ldb_data directory, "real_data" and "simulated_data", each with a different set of links. When executing an app, changing from one dataset to the other will be a one line change, from parameter.data_path = "real_data" to parameter.data_path = "simulated_data". A folder like "real_data" has a fixed structure of links corresponding to the needed data such as ACS, bolometer, timing, etc. We show below a simplified example of this fixed structure.

```
ldb_data\
   real_data\
      acs\
           acs --> link to the acs dataset from flight
           timing --> link to the time array for the acs
           pointing --> link to reconstructed attitude
      bolo\
          bolo --> link to the raw bolometer dataset
          template_subtracted --> link to the bolometer dataset
                                   with the HWP synchronous signal removed
          timing --> link to the time array for the bolometer
   simulated_data\
      acs\
           acs --> link to the simulated acs dataset
           timing --> link to the time array for the acs
           pointing --> link to simulated attitude
      bolo\
          bolo --> link to a simulated bolometer dataset
          template_subtracted --> link to a simulated bolometer dataset
                                   with the HWP synchronous signal removed
          timing --> link to the time array for the bolometer
```

documentation   This directory stores relevant memoranda, figures helpful for understanding the function of various pipeline stages, and definitions and conventions used throughout the pipeline.

In the next sections, we review individual pipeline stages.

8.5 Simulations

The function of the simulation app is to simulate bolometer time-streams. It is not a pipeline stage per se, but it is used extensively to test apps in development, to understand the effects of a given stage on our data (eg map making, or template removal), or to investigate various bolometer properties such as time constants, noise, or template magnitude. It takes as input three sky maps of the Stokes parameters I, Q and U (for example, the Planck Sky Model integrated over the EBEX frequency bandwidth), time-dependant boresight attitude and HWP angle γ; and scans the sky producing bolometer time-streams as a function of time according to our data model in Equation 8.12. Most commonly, the LD2013 flight attitude is used to simulated realistic scanning, but any attitude can be input to the app. Various options are available to build upon the model:

- **add noise**: the desired noise power spectrum properties (white noise level, f_{knee} and α values) can either be input from the user, measured on-the-fly from flight data, or pre-computed values from the leap/resources folder can be loaded. Noise is simulated by producing white noise with the desired level, taking its power spectrum and scaling the frequencies smaller than f_{knee} by $f^{-\alpha}$, and finally inverting the power spectrum.
- **add HWP synchronous signal (template)**: the HWP template can be added to the data. The template measured from LD2013 flight data can be used, or the user can provide his own coefficients A_n and B_n defined in Equation 8.15.
- **simulate time constant**: the time-streams can be modified according to a single-pole low-pass filter modelling the time constant response of a bolometer. Time constants can be input by the user, or values measured pre-flight can be loaded from the leap/resource folder.

99

- **simulate non-linearity**: as we will show in Chapter 9, our detectors exhibit a non-linear response. The simulation app has the option to simulate this non-linearity with a user-defined function.

- **simulate instrumental polarization (IP)**: IP is modelled by adding to the existing time-stream the following power:

$$s_{IP}(t) = I(t)\epsilon_{IP}\cos(4\gamma - 2\alpha_{IP})$$

where $I(t)$ is the bolometer time-stream scanned from the I map, and ϵ_{IP} and α_{IP} are the user-provided IP leakage and angle for that bolometer.

The simulated time-streams are written to disk by the i/o library, in the same format as the flight data. This means in later stages, apps can seamlessly switch between loading simulated data or flight data as they have the same format. Using the LEAP multiprocessing tools, each board and each segment of data are processed independently and in parallel. As a result, simulating time-streams with noise for ~1,000 bolometers during 11 days of flight takes ~12 hours on a 24-core computer.

8.6   Timing Alignment

Two time-servers (A and B) provide timing to EBEX subsystems, each through a major period incrementing every six hours and a minor period incrementing every 1e-5 seconds. The ACS receives both time-servers, while each bolometer board receives either time-server A or B. The goal of the timing app is to produce a time array for each dataset (ACS, boards, ss boards, HWP boards) that can be used to align the asynchronous datasets. It is also convenient to add an offset to this time array in order to synchronize with the unix time providing absolute timing. This is done using CPU time provided by the flight computers. The aligned and offset timing streams are labeled "etime". The output of the timing app is a set of a Dirfiles for each dataset along with the corresponding etime channel.

Multiple bugs in the raw timing were identified and fixed in the generation of etime. We list here the major bugs found. The minor period occasionally shows one sample transients of unknown origin. These samples are identified and interpolated. The major periods are sometimes set to zero at computer reboots following a bug in the time-server firmware, until the major period increments and jumps to its correct value. These samples are easily found and the major period replaced with the correct value. Before computer reboots, old samples are sometimes found to be inserted at the end of a Dirfile, in all ACS channels, for reasons still being investigated. These samples are found by searching for etime decrementing instead of incrementing, and those samples are marked as invalid. Finally, the minor period occasionally increments at half its nominal rate for a short duration, again due to a bug in the time-server firmware. These samples are found and marked as invalid. After all those issues are identified and fixed, etime is generated and written to disk for each dataset. For the ACS dataset, two etime channels are generated: one from time server A and one from time server B.

We plot in Figure 8.3 the difference between etime A and etime B computed from the ACS stream over the entire flight. The gap around January 2, 2013 corresponds to a period when time-server A was down for the ACS. During this time, we align the boards on time-server A with attitude timestamped by time-server B. Because the maximum difference between the two time-servers is 0.002 seconds, and 90% of our scan speeds are under $0.5° \, \mathrm{s}^{-1}$, we conclude that the attitude error coming from mismatching the time-servers is at maximum a few arcseconds and can be ignored. Given that conclusion and to simplify the i/o and interpolation software, we use time-server A to generate the reference ACS etime for most of the flight, except when it is down during which we use time-server B. The LEAP i/o management library uses the etime channel to interpolate attitude, HWP and SS data to each board time base.
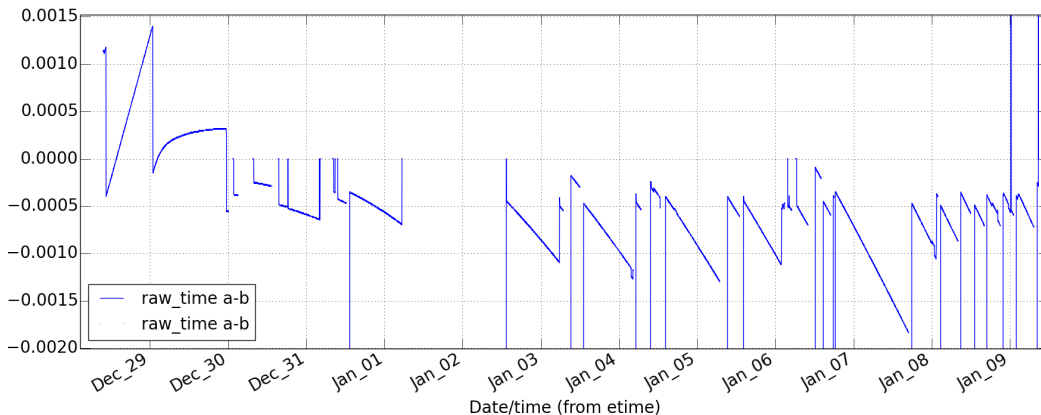
Figure 8.3: Time difference between etime generated from time-server A and etime generated from time-server B, showing an absolute maximum of ∼0.002 seconds. The vertical lines correspond to invalid samples and can be ignored.

8.7 Time-stream cleaning

Before using bolometer time-streams for map making, we first remove the HWP synchronous signal, flag invalid samples, and replace transients with noise realisations.

8.7.1 Template Removal

The continuously rotating HWP creates a signal in the bolometer time-stream. The largest contribution to this signal comes from instrumental polarization and polarized emissions from the mirrors. Thermal emission from the HWP is another contributor. This signal, called from hereafter the HWP template, is synchronous with the HWP rotation rate f_{hwp}= 1.23 Hz. It is several orders of magnitude larger than the sky signal and the bolometer noise, and larger than was anticipated pre-flight, due to instrumental polarization (see Chapter 9). A plot of the HWP template versus time, and the HWP template versus HWP angle is shown in Figure 8.4. Linearly polarized radiation of constant power incident on the HWP will create power in the detector time-stream at the 4th harmonic of the HWP rotation rate (see Section 8.2.2). The polarization signal from the sky is modulated by the telescope scan
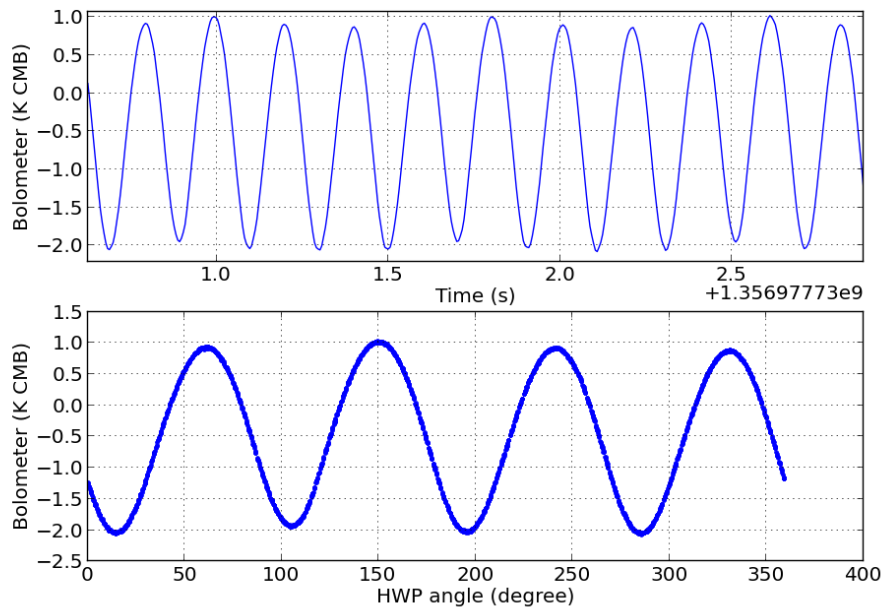
Figure 8.4: *Top:* Plot of a calibrated bolometer time-stream prior to HWP template removal over ∼3 s of data. The HWP template has amplitude of ∼3 K and dominates the signal. *Bottom:* Plot of the same bolometer time-stream versus HWP angle, showing the HWP template is synchronous with the HWP rotation. The 4th harmonic dominates the template.

and will have power in the sidebands of the 4th harmonic, which is how we differentiate it from the polarized emissions of the instrument which are stationary. We model the HWP template as:

$$h(t) = \sum_{n=1}^{n=20} (C_{1_n} + C_{2_n}t)\cos(n\gamma(t)) + (S_{1_n} + S_{2_n}t)\sin(n\gamma(t)) \tag{8.17}$$

where $\gamma(t)$ is the measured rotation angle of the HWP (see Chapter 2). To remove the HWP template, we need to find the C_n and S_n coefficients for all harmonics of interest. Because the HWP template is 10^3-10^4 orders of magnitude larger than the bolometer noise and the sky signal, we neglect the sky signal and the noise to find the HWP template and fit for $h(t)$ as a function of the HWP angle $\gamma(t)$ using a maximum likelihood method. Gathering all samples of $h(t)$ in a vector, we re-write Equation 8.17 in a matrix form:

$$\vec{h}_t = \Omega_{tn} \, C_n \tag{8.18}$$

where we use:

$$
C_n = \begin{pmatrix} C_{1_1} \\ C_{2_1} \\ S_{1_1} \\ S_{2_1} \\ C_{1_2} \\ C_{2_2} \\ S_{1_2} \\ S_{2_2} \\ . \\ . \\ . \end{pmatrix} \tag{8.19}
$$

$$
\Omega_{tn} = \begin{pmatrix} \cos\gamma(t_0) & t_0\cos\gamma(t_0) & \sin\gamma(t_0) & t_0\sin\gamma(t_0) & \cos 2\gamma(t_0) & t_0\cos 2\gamma(t_0) & \sin 2\gamma(t_0) & t_0\sin 2\gamma(t_0) & ... \\ \cos\gamma(t_1) & t_1\cos\gamma(t_1) & \sin\gamma(t_1) & t_1\sin\gamma(t_1) & \cos 2\gamma(t_1) & t_1\cos 2\gamma(t_1) & \sin 2\gamma(t_1) & t_1\sin 2\gamma(t_1) & ... \\ . & . & . & & & & & & \\ . & . & . & & & & & & \end{pmatrix} \tag{8.20}
$$

The maximum likelihood estimator of C_n is:

$$\hat{C}_n = (\Omega^T \Omega)^{-1} \Omega^T \vec{h}_t \tag{8.21}$$

Before building the Ω matrix and solving for the C_n coefficients, the bolometer time-stream in $\vec{h}_t$ is pre-processed as follows:

- A temporary estimate of the slow varying drifts in the bolometer time-stream (called the signal baseline) is computed and removed from the time-stream using a 10th order Butterworth low-pass filter with cutoff frequency 0.2 Hz set by the f_{knee} of the bolometer noise properties (see Table 8.2).

- A temporary template is computed and subtracted from the baseline-removed bolometer time-stream, using the maximum likelihood method described above.

- Transients are identified using the temporary template subtracted time-streams, using the procedure described in Section 8.7.3. Transients are thought to be caused by cosmic rays or electrical burst noise.

- A definitive baseline is computed from the temporary template-subtracted time-stream using a moving mean with window size 4.87 s (corresponding to 6 HWP rotations).

- The definitive baseline is subtracted from the raw bolometer time-stream which is then band-passed filtered between 0.01 and 40 Hz using a Butterworth filter of order 8. The bandpass is chosen to remove DC and high-frequency noise, while keeping the information in our signal bandwidth.

- The final template is computed using the filtered time-stream, and the maximum likelihood method, on chunks of 60 seconds. This 60 second period is chosen empirically to ensure the best removal of the HWP template given its observed time-varying coefficients, while ensuring enough rotations are included in the fit to find the coefficients. We are still investigating why removing the HWP template on longer timescales gives sub-optimal results. Note that removing the template on 60 second chunks will remove
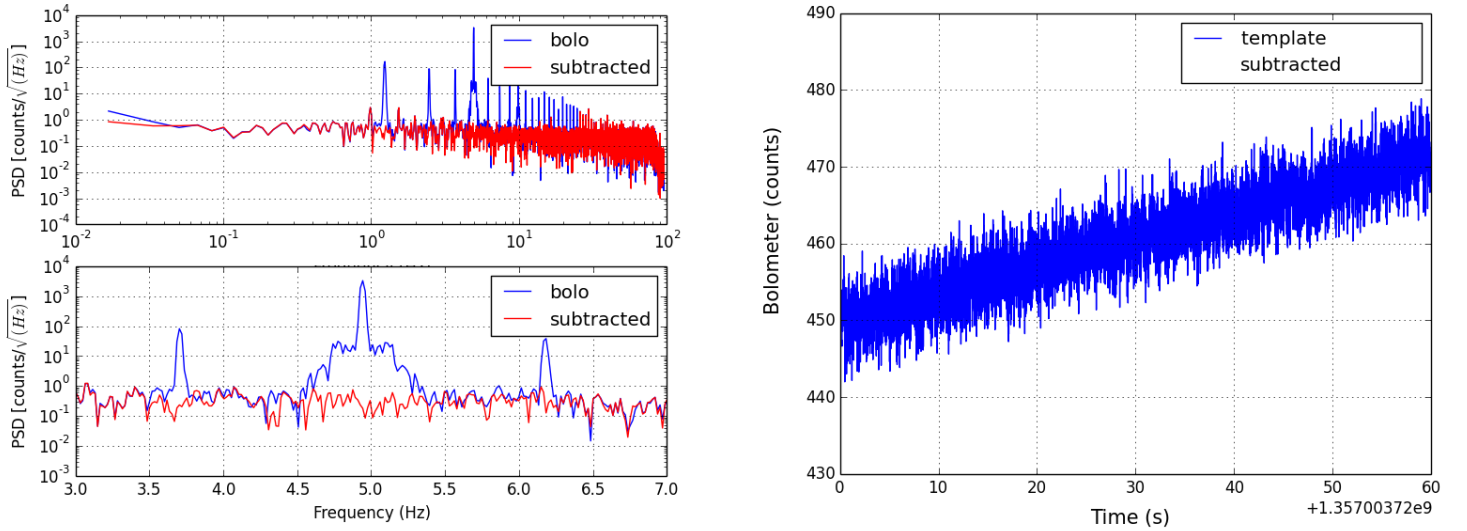
Figure 8.5: *Left:* PSD of a bolometer time-stream before (blue) and after (red) template subtraction. All harmonics of the HWP rotation frequency are visible in the pre-subtraction time-stream. Harmonics above n=20 are not removed to save computation time since those harmonics are filtered out of the analysis in subsequent steps. A zoom around the 4th harmonic is presented in the bottom panel, showing successful template removal at the level of the noise. *Right:* Plot of a bolometer time-stream after template removal over a ∼60 s period.

the sky polarization signal on angular scales larger than ∼6°.

Figure 8.5 shows an example of a bolometer time-stream and the corresponding PSD after successful template removal. Though the template removal procedure is successful in the majority of cases, a significant number of sections show leftover template after the removal procedure, as shown for example in Figure 8.6. Temperature variations in the instrument are being investigated as possible causes. Un-removed template shows up as power around $4 \times f_{hwp}$ (see Figure 8.6), which after demodulation corresponds to power at low frequencies. To account for the un-removed template, we apply a high-pass filter to the Q/U time-streams after demodulation and before map making. See Section 8.9 for more details.

106
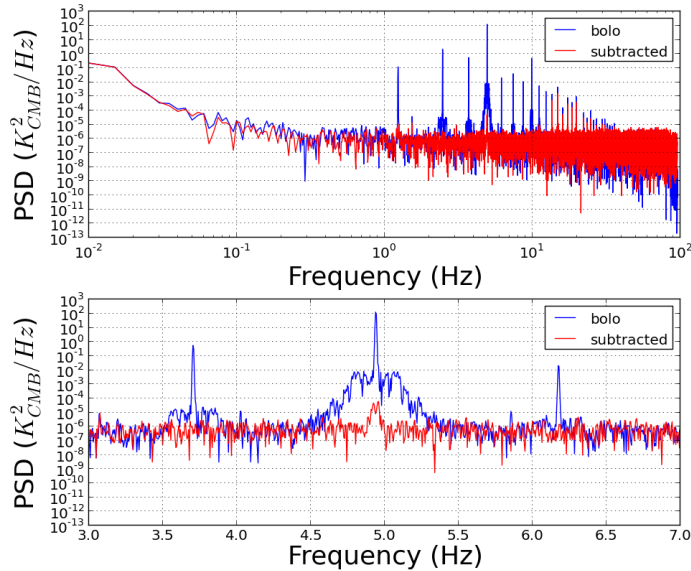
Figure 8.6: Example of a bolometer with leftover template after the removal procedure. The plot shows the PSD of a bolometer time-stream before (blue) and after (red) template subtraction. The bottom panel is a zoom around $4 \times f_{hwp} \sim 5$ Hz.

8.7.2   Data Flagging

Data flagging aims at identifying samples in the time-streams containing either abnormalities or undesired features, and removing those samples from the final data included in sky maps. A flag array is produced for every bolometer indicating for each sample if the sample is valid (1) or invalid (0). The map making procedure then uses the flag array to decide which samples to include in the maps.

Data flagging is implemented in LEAP as a library function, with each individual flag and its parameters modifiable through the function arguments. When needed, the flagging function is called inside an app and the flag array is generated during the app execution according to the parameters specified by the user. If no parameters are specified the default values for the flagging are called. Each individual flag and the corresponding code and default arguments are added to the library function by the collaborator finding the need for this new flag. We decided to generate the flag array every time an app runs because

107

parameters to generate flags are subject to change and writing flags to disk for the entire flight takes time. If a given flag takes significant time to generate, it is written to disk and re-loaded when the flagging function is called.

We list here the flags implemented for LD2013, and when relevant, their default parameters (which are used for map making). Figure 8.7 shows the percentage of data affected by each flag, as well as the cumulative percentage of data affected.

- **hwp transition cuts**: Flags samples when the HWP is ramping up or down and has not reached its final rotation speed. The HWP is stopped for take-off and various housekeeping operations throughout the flight.

- **valid template**: Flags samples when the HWP synchronous signal cannot be fit and removed. This mainly includes when the HWP is not spinning or when bolometers are unresponsive. This flag should be turned off for Stokes I analysis as the HWP doesn't need to be spinning to collect temperature information.

- **template removal glitch**: Flags samples that were found to be transients in the HWP template removal analysis. These are a subset of the transients found with the "glitch cuts" flag, but was implemented first and has been kept historically.

- **bad squid dc**: Flags samples when the SQUID direct current is not nominal.

- **squid jumped**: Flags samples when the SQUID is operating at the edge of its linear response.

- **max covariance dec**: Flags samples when the reconstructed attitude has uncertainty greater than $5'$. This flags ∼10% of the data because of periods lacking star camera solutions, corresponding to the instrument being turned on and set-up after intentional and necessary shutdowns.

- **glitch cuts**: Flags samples that were found to be transients ("glitches") in the bolometer time-streams after the HWP synchronous signal was removed. Note that a known issue in the HWP template removal app leaves glitch-like features in the bolometer time-streams, increasing the number of samples that get flagged for glitches. The issue

is now fixed and a new HWP template being generated, but the percentage of glitch cuts is not updated in Figure 8.7. See Section 8.7.3 for more details on the origin of transients and the procedure to identify them.

- **el step**: Flags samples that are part of an elevation change.

- **latched bolo**: Flags samples when bolometers become unresponsive after not receiving enough power ("latching"). This can happen when the amount of power incident on a bolometer decreases after tuning, such that the bolometer is taken fully into its superconductive regime and has zero resistance, and thus no current response to incoming power. Bolometers need to be re-tuned after a latching event. Several bolometers exhibit latching events late in the flight, for reasons still being investigated.

- **max velocity**: Flags samples when the telescope is moving faster than 1.5 (0.8) $^\circ\,\mathrm{s}^{-1}$ for I (Q/U) Stokes parameters time-streams. For Q/U, the cutoff is determined by requiring limited overlap of the I and Q/U signal bandwidth (see Section 8.9.1 for more details). For I, the flag is a sanity check and invalidates negligible amounts of data.

- **t calib**: Flags sections of data for which the bolometer calibration procedure provided outlier values (see Section 8.8 for more details). These can come from insufficient Galactic coverage or unresponsive bolometers.

- **min velocity**: Flags samples when the telescope is moving slower than $0.01^\circ\,\mathrm{s}^{-1}$. For I, the cutoff is determined by requiring limited overlap between the signal bandwidth and slow varying noise. This cutoff could be relaxed if using a Maximum Likelihood or Destriper map maker which identifies and removes slow varying noise. For Q/U, the cutoff is determined by requiring limited overlap between the signal bandwidth and the bandwidth of leftover HWP template. This cutoff could be relaxed with improved removal of the HWP template (see Section 8.7.1).

- **stimulator cuts**: Flags samples when the stimulator (a power source inside the receiver) is flashing. The stimulator periodically flashes every $\sim$20 minutes to measure
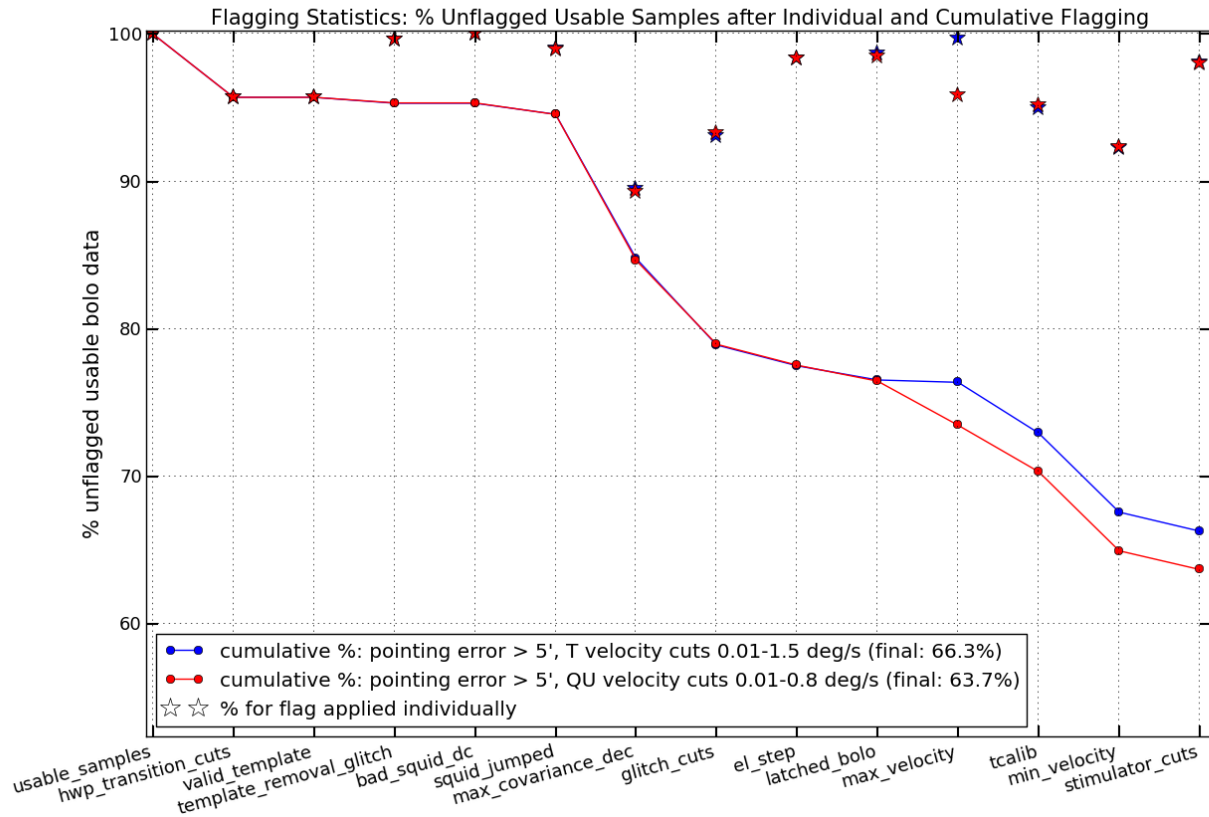
Figure 8.7: Percentage of valid data remaining after flagging for stokes I (blue) and Q/U (red) time-streams. Usable samples are defined as samples having tuned bolometer data. Stars correspond to valid data remaining after each flag is applied individually. Dots and connecting lines corresponds to valid data remaining after cumulative flagging.

the responsivity of the bolometers.

8.7.3 Transient Removal

As mentioned previously, transients exist in the data, as shown for example in Figure 8.8. They are thought to originate either from cosmic rays or from electrical burst noise. All transients observed correspond to a sudden and brief **increase** of power on the detectors. Transients bias the sky maps and need to be removed. In this section, we detail the procedure to identify transients. This procedure is used to generate the "glitch cuts" and "template
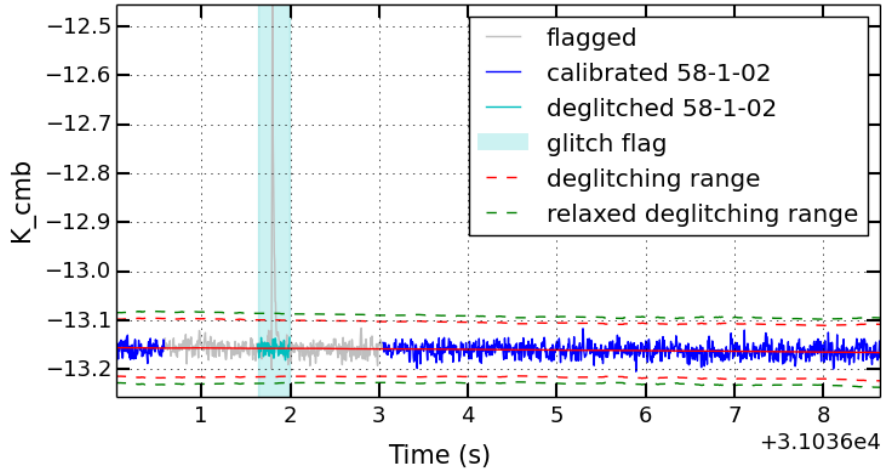
Figure 8.8: Example of transient identification and removal. In blue is a calibrated time-stream for bolo 58-1-2. The cyan rectangle represents the initial duration of the transient flag and the cyan line shows a white noise realisation around the moving median (solid red line). The grey line shows the final flagging with the 1 s buffer. The dashed line represent the moving MAD multiplied by rejection factor 6.5 (red) and 8.0 (green, used for Galaxy crossings only).

removal glitch" flags detailed in Section 8.7.2. Note that in addition to finding and flagging samples containing transients, it is necessary to replace transients with noise realisations before any filtering is performed on the time-streams. This is because when performing an FFT on a time-stream, which is needed for Butterworth filtering, it is not possible to flag out any samples in the data array to be Fourier transformed. Filtering a transient will induce ringing of the transient outside the flagged samples, and chunking up the data to exclude all transients will result in a multitude of small chunks and induce unnecessary edge effects. Instead, we replace the transients with noise realisations before filtering, and then exclude the flagged samples (and thus the noise realisation) from the map.

Similarly to flagging, transient removal ("deglitching") is implemented in LEAP as a library function and called by any app needing to remove transients from the time-streams. The algorithm to flag transients and replace the flagged samples with a noise realisation is detailed below. Figure 8.8 illustrates the procedure by showing an example of a transient, its flagging and replacement with noise realisation. The algorithm works as follows:

- First pass of transient removal using the Median Absolute Deviation (MAD):

  – The moving median of the time-stream is computed with window size 5 seconds (solid red line in Figure 8.8).

  – The absolute deviation of the time-stream from the moving median is computed.

  – The moving median of the absolute deviation (MAD) is computed with window size 5 seconds. For normally distributed data, $\sigma = 1.48$ MAD where σ is the standard deviation.

  – The samples with absolute deviation greater than 6.5 times the moving MAD are flagged as transients. For normally distributed data, this corresponds to flagging samples located more than $\sim 10\ \sigma$ away from the mean. This number is chosen to ensure minimal probability of discarding valid, normally distributed data. 6.5 is called the rejection factor. In Figure 8.8, the moving MAD times the rejection factor is plotted in dashed red.

- To avoid flagging the Galaxy, samples with associated Galactic latitude within +/- 4° from the Galaxy center are processed with the above transient removal code but a rejection factor of 8.0. This number is empirically chosen given the observed strength of the Galaxy signal in the bolometer time-streams. In Figure 8.8, the moving MAD times the relaxed rejection factor is plotted in dashed green.

- Some transients, called "burst noise", appear as a series of transients closely spaced in time. These burst noise events can bias the moving MAD and not be flagged by the first pass of transient removal. To address this issue, we use the fact that all transients are always in the same direction (of increased power on the detector). We perform a second pass of transient removal where we use the moving minimum of the time-stream (instead of the moving MAD) as a baseline to find samples part of transients. This is not shown in the figure.

- If transients are separated by less than 30 seconds, the data is between those transients is also flagged as invalid. This is a precaution to avoid including data affected by

anomalous electrical noise. A 30 sample buffer around each transient is added to the flags, to ensure the entirety of the transient is flagged out. The flagged samples correspond to the cyan rectangle in Figure 8.8.

- The white noise component of the time-stream is calculated using the data left and right of the transient, on timescales equivalent to the duration of the transient. The flagged samples are replaced with the moving median and a white noise realisation, as shown with the solid cyan line in Figure 8.8.

- A $\sim$1 s buffer is added to each side of the flags to ensure any ringing of the white noise realisation from filtering doesn't affect valid data. This corresponds to the greyed solid line outside of the cyan rectangle in Figure 8.8. A $\sim$1 s buffer is empirically shown to be sufficient to flag any ringing given our filtering bandwidth.

8.8 Calibration

For each detector, we need to determine the relationship between "counts" from the read-out system, and power on the sky expressed in equivalent black body temperature K_{CMB}. We do this by comparing single detector maps in "count" units to a reference map in K_{CMB}. Using all pixels on the Galaxy, we find the best fit calibration in units of K_{CMB} per count. In this section, we summarize the procedure used to find the calibration. A detailed description is available in [57].

To create the single detector Stokes I sky map, we follow the procedure described in the preceding sections: HWP template removal, flagging, transient removal, filtering and weighted binning (the last two stages are described in Section 8.9). We compare this detector map in units of "counts" to a reference map processed in an similar manner. It is important that the reference map be processed in a similar manner to flight data to account for the effects of filtering, flagging and coverage. A full sky reference map is first generated by summing the Planck component maps [58], scaled and integrated over the corresponding

EBEX frequency band. Then we generate reference time-streams in order to filter and flag them similarly to flight data. We achieve this by using the flight detector attitude and scanning the reference map. The reference time-streams are then flagged, filtered and re-binned into sky maps, identically to the EBEX bolometer time-stream. The two maps are now ready to be compared. All pixels pertaining to the Galactic plane are used to find a single multiplicative factor converting counts to power. The CMB is not used due to its low signal-to-noise for single detector maps, and RCW38, initially chosen for calibration, is scanned sporadically by a subset of detectors due to our revised scan strategy and is therefore unsuitable as a calibration source.

The calibration procedure requires simultaneous optimization of the beam size of the telescope and the star camera to detector rotation angles. If the reference map is not smoothed to the LD2013 EBEX beam size, two maps with different beam sizes will be compared and a biased calibration will be found. Similarly, if the star camera to detector rotation angles is wrong, the single detector map will be shifted compared to the reference map, which will bias the measurement of the calibration. An iterative process is developed to alternatively find the calibration and the beam size and rotation angles. A first calibration factor is obtained for every detector using the beam size and rotation angles measured pre-flight. Then with this first calibration factor measured for each detector, co-added maps of RCW38 are generated using all detectors in a given wafer. This RCW38 map is compared to the reference RCW38 map to find the beam size and the rotation angles. We use RCW38 because of its strong signal and because it is close to being a point source, and as such it puts strong constraints on the possible beam sizes and rotation angles. All detectors within a wafer are co-added to increase signal to noise and coverage of RCW38. A single telescope beam size for all detectors is assumed. Furthermore, only the rotation from the star camera to the center of the wafer is fit. The position of the detectors with respect to the center of the wafer is modelled using known relative positions of horns on the monolithic focal plane.

This two step process of first finding each detector calibration factor, followed by optimiz-

ing the telescope beam size and star camera to beam offsets, is repeated until all parameters converge. The mean calibration values, beam size and star camera to boresight rotation angles are listed per frequency band in Table 8.1. Note that the effective beam size is a factor of ~2 larger than the design value. This could be optical or from an improper model for the detector positions, and is still being investigated.

Table 8.1: Calibration parameters for LD2013.

Frequency Band (GHz)	Calibration (μK_{CMB}/count)	Smoothing scale (′)	Star Camera to Boresight angles (°)
150	-1,253	16	(-0.29, 2.83, 1.42)
250	-2,088	16	(-0.30, 2.84, -1.76)
410	-27,205	20	(-0.31, 2.85, 2.54)

8.9   I, Q, and U Maps

8.9.1   Overview

We present here the map making procedure that is implemented in LEAP to produce maps of the Stokes parameters I, Q and U. Often referred to as "naive" map making, it consists of high-passing the time-streams to eliminate slow varying drift noise, and then binning the time-streams, weighted by the inverse of their covariance, into pixels. A part of the sky signal is filtered-out by this procedure. More elaborate map makers, such as Maximum Likelihood or Destriper maps makers, attempt to estimate the noise properties and separate noise and sky signal at low frequencies. Currently two efforts exist in EBEX to apply these more sophisticated map makers to EBEX data, but are not presented here.

To understand the various necessary steps and possible trade-offs in the naive map making procedure, let us examine a diagram of the PSD of our bolometer model, re-written in Equation 8.22 with colors matching the corresponding curves in Figure 8.9.
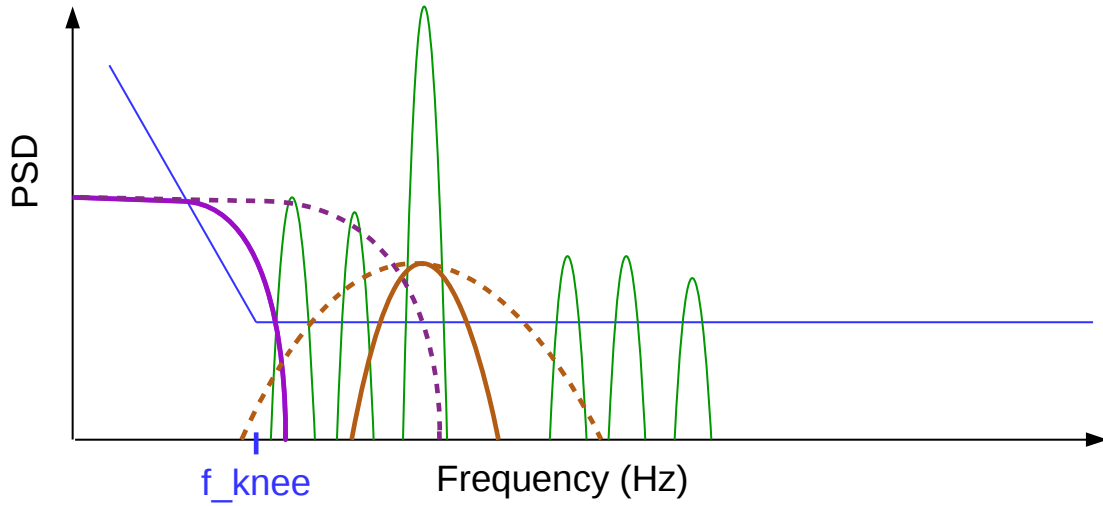
Figure 8.9: Diagram of the components of a bolometer PSD: sky I (purple), sky Q/U (brown), selected HWP template harmonics (green) and noise (blue). Dashed curves correspond to sky signal for faster scan speeds or smaller angular scales. For example, a $30'$ feature scanned at $0.1°\,\mathrm{s}^{-1}$ will have a PSD with FWHM of 0.7 Hz

.

$$s(t) = \frac{1}{2}\left(I_{in}^{sky}(t) + P_{in}^{sky}(t)\cos(4\gamma - 2\alpha_{in}^{sky}(t) + 2\psi)\right) \tag{8.22}$$

$$+ \sum_{n=1}^{n=20} A_n \cos(n\gamma + \phi_n)$$

$$+ n(t)$$

As shown in the diagram, the I time-stream has a low-frequency bandwidth centered around 0 Hz. The Q/U time-stream has a bandwidth centered around $f = 4f_{hwp} \sim 5$ Hz. A Gaussian feature in the sky with angular scale θ will have a Gaussian shaped PSD with width:

$$\sigma_{freq} = \frac{1}{2\pi}\frac{\text{scan speed}}{\theta} \tag{8.23}$$

Following this equation, low scan speeds or large angular scales are represented in the diagram by the solid lines, and fast scan speeds or small angular scales by the dashed lines. Filtering (see Section 8.9.3) and scan speed selection (see Section 8.7.2) for naive map making are designed to address the following issues:

- Low scan speeds / Large angular scales:

  - Stokes I bandwidth is dominated by 1/f noise

  - Stokes Q/U bandwidth will overlap with any leftover HWP template from the 4th harmonic.

- High scan speeds / Small angular scales: Stokes Q/U and Stokes I overlap in the time domain. For a given pass over a pixel, allowing those high speed samples will result in I leaking into Q/U maps. Repeated passes over the same pixels, with multiple HWP angles, will average the I component and reduce the I leakage.

- All speeds and angular scales: high frequencies contain HWP template (harmonics larger than n=20 not removed by the template removal) and noise, but no sky signal.

In the next section, we list the LD2013 scan speeds and noise properties used to design the time-stream filtering presented in the following section.

8.9.2   LD2013 Scanning Speeds and Noise Characteristics

The distribution of scan speeds during the LD2013 flight is shown in Figure 8.10. The median scan speed is $\sim 0.1° \, \mathrm{s}^{-1}$, with 85% of the data taken between scan speeds $0.01° \, \mathrm{s}^{-1}$ and $1.0° \, \mathrm{s}^{-1}$.

Though not reviewed here, a noise analysis app was developed to measure the PSD properties for each bolometer, fitting each PSD to the model $PSD = NET \times (1 + (f_{knee}/f)^{\alpha})$ [59]. Table 8.2 summarizes the results of this analysis providing the median NET, f_{knee} and α values per frequency band:
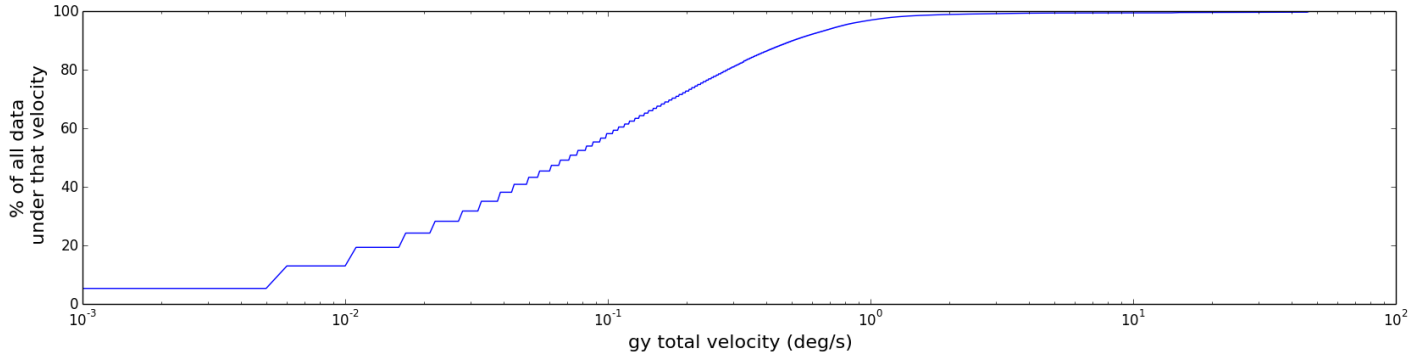
Figure 8.10: Distribution of scan speeds during LD2013 flight. The curve shows the percentage of data (y-axis) taken below a corresponding scan speed (x-axis) measured by the total gyroscope ("gy") velocity.

Table 8.2: LD2013 Median Noise Parameters.

Frequency Band (GHz)	NET $(\mu K_{CMB}\sqrt{s})$	f_{knee} (Hz)	α (unit-less)
150	478	0.2	2.1
250	1,053	0.2	2.1
410	17,600	0.2	2.1

8.9.3 Filtering

Deconvolution

The bolometers have a time constant and act as a low-pass filter on incoming radiation, filter that we model as a 1 pole RC-filter:

$$s_f(f) = \frac{1}{1 + i\frac{f}{f_{3dB}}} s_i(f)$$

where f is the frequency, $s_i(f)$ is the Fourier transform of the incoming radiation, f_{3dB} is the time constant frequency and $s_f(f)$ is the bolometer response. If unaccounted for, the time constant disturbs rapidly varying I signals in time and rotates the incoming polarization angle $\alpha = 0.5\arctan(U/Q)$. Tests were performed pre-flight to measure the time constants [39],

118

showing f_{3dB} in the range 10-15 Hz. Analysis is still underway to measure LD2013 bolometer time constants, and as a result the analysis presented in the next sections does not include any time constant deconvolution, though the ability to do so is already implemented in the map making pipeline. Note that bolometer time constants vary with optical load, depth of transition, and bath temperature, and as a result must be re-measured in flight. If LD2013 flight time constants are consistent with pre-flight measurements, not accounting for the time constants translates into a negligible distortion effect for I (given our scan speeds and beam size), and a polarization rotation of $\sim 10°$. For comparison, the overall rotation of the instrument and the HWP angle must be known to $0.3°$ in order for spurious B-modes produced from rotational errors to be less than 10% of the expected gravitational lensing B-modes [60].

Temperature & Polarization Filtering Summary

In the two following subsections, we describe in detail the filtering applied to the calibrated, template removed signal in order to extract I, Q and U time-streams. We summarize those filters in Figure 8.11, where we show the PSD of a calibrated, template-subtracted bolometer from LD2013, as well as the bandwidth of the filters described below, the HWP rotation frequency and the f_{knee} of the bolometer noise. We purposely chose a detector with leftover HWP template after subtraction in order to illustrate the purpose of the post-demodulation polarization high-pass filter described below.

Temperature Filtering

A Stokes I time-stream is obtained by applying a band-pass filter to the calibrated, template removed bolometer signal $s(t)$. The band-pass filter is a Butterworth filter of order 10 with bandwidth 33 mHz to 3.0 Hz, corresponding to the pink shaded area in Figure 8.11. It ensures rejection of 1/f noise as well as high frequency noise and un-removed template harmonics. Simulations show the filtering cuts out $\sim 40\%$ of the CMB signal. This is mainly due to
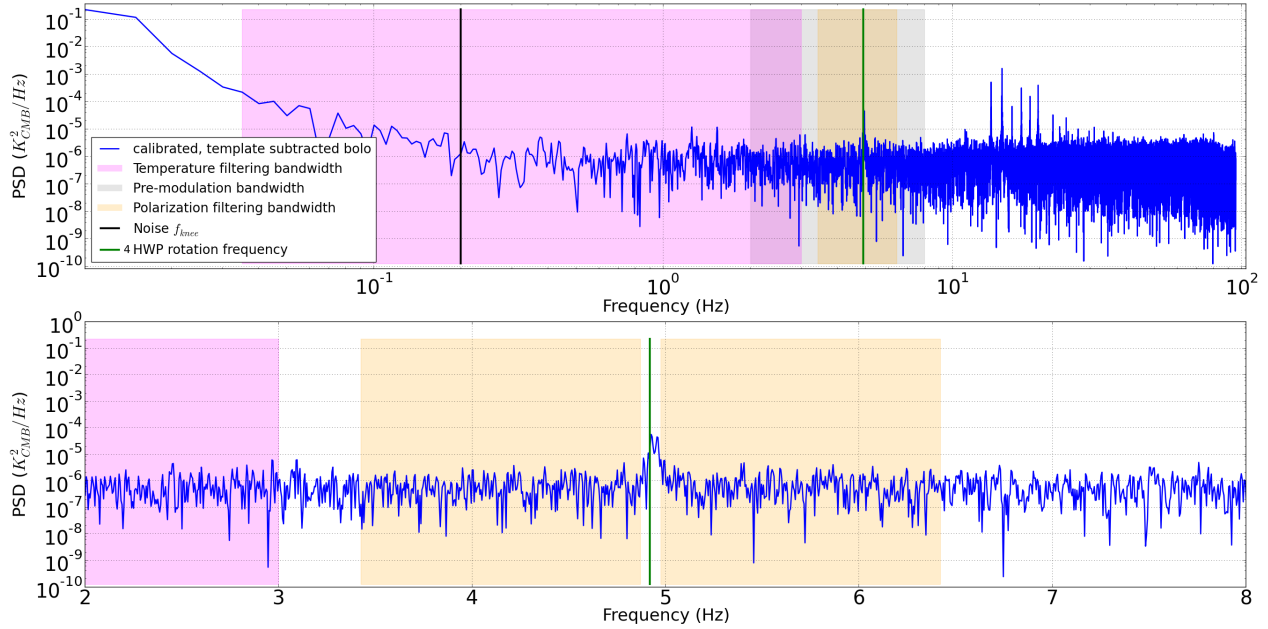
Figure 8.11: Top panel: PSD of a calibrated, template removed bolometer from LD2013 (blue). The pink shaded region corresponds to the bandwidth of the bandpass filter used to extract the I time-stream. The grey shaded region corresponds to the pre-modulation bandwidth. Signal out of the grey region will be filtered out before modulation is applied to the time-streams. The orange shaded region corresponds to the bandwidth of the post-modulation bandpass filter used to extract Q and U time-streams. The bottom panel is a zoom on the frequencies relevant to polarization. Leftover template is apparent in the bolometer PSD (blue), and the gap in the orange bandwidth coming from the post-demodulation highpass filter is designed to reject the leftover template.

our unanticipated scan strategy with a median speed of $0.1°\,\mathrm{s}^{-1}$, compared to the designed scanning speed of $0.4°\,\mathrm{s}^{-1}$. Some of this signal can be recovered by using more sophisticated map makers. Note that the DC level of the bolometer time-stream has no physical meaning and that EBEX is designed to measure the CMB anisotropies and not the total CMB power.

Polarization Filtering and Demodulation

To obtain the Stokes Q/U time-streams, a "demodulated" time-stream $s_Q(t)$ (or $s_U(t)$) must first be generated from the bolometer signal $s(t)$ by multiplying it by $\cos(4\gamma + 2\psi)$ (sin for

$s_U(t)$):

$$s_Q(t) \equiv 4\,s(t)\cos(4\gamma + 2\psi) \tag{8.24}$$

$$= 2I_{in}^{sky}(t)\cos(4\gamma + 2\psi) + 2Q_{in}^{sky}(t)\cos^2(4\gamma + 2\psi) + 2U_{in}^{sky}(t)\sin(4\gamma + 2\psi)\cos(4\gamma + 2\psi)$$

$$= Q_{in}^{sky}(t)$$

$$+ 2I_{in}^{sky}(t)\cos(4\gamma + 2\psi)$$

$$+ Q_{in}^{sky}(t)\cos(8\gamma + 4\psi) + 2U_{in}^{sky}(t)\sin(4\gamma + 2\psi)\cos(4\gamma + 2\psi)$$

$$s_U(t) \equiv 4\,s(t)\sin(4\gamma + 2\psi) \tag{8.25}$$

The demodulation pushes the I signal to higher bandwidth, and brings the Q (or U) signal to the low frequencies. On Figure 8.11, demodulation has an effect similar (but not identical) to inversing the pink and orange shaded area. The I signal now has power in a bandwidth centered on $4f_{hwp} \sim 5\text{Hz}$. To filter out the I power, we low-pass the demodulated s_Q or s_U, thus obtainting Q and U time-streams:

$$Q(t) \equiv \text{lowpass}(s_Q(t)) = Q_{in}^{sky}(t)$$

$$U(t) \equiv \text{lowpass}(s_U(t)) = U_{in}^{sky}(t) \tag{8.26}$$

Before demodulating the time-streams, the bolometer signal is processed with a Butterworth band-pass of order 10 and bandwidth 2 Hz to 8 Hz, as shown by the grey shaded area in Figure 8.11. This ensures DC levels in the bolometer aren't transformed into large 5 Hz sinewaves, and high frequency noise isn't folded into the signal bandwidth. The time-stream is then demodulated to produce s_Q and s_U. We note here that when demodulating, including the Galactic roll ψ in the argument to the sinewave will produce Q and U time-streams in the sky frame. Not including the Galactic roll will produce Q and U time-streams in the instrument frame. Finally, the s_Q and s_U time-streams are band-passed again using a

Butterworth filter of order 10 and bandwidth 50 mHz to 1.5 Hz, as shown by the orange shaded area in Figure 8.11. As mentionned above, the low-pass filter is used to remove the I leakage coming from the term $I_{in}^{sky}(t)\cos(4\gamma + 2\psi)$ in s_Q, though we note that repeated passes over a given pixel with various γ angles will have the same effect of averaging down the $\cos(4\gamma + 2\psi)$ term. The high-pass filter is used to remove any leftover template, as shown by the gap in the orange bandwidth in the lower panel of Figure 8.11. This filter will be removed or minimized as improved template removal releases are made.

8.9.4 Weighted Binning

The I, Q and U time-streams are noise dominated and are used directly to compute a noise variance estimate for every time sample. For each I, Q and U time-stream, a moving variance is computed with a window size of 20 minutes (to privilege long, stable noise measurements), and is used as a weight array for binning the time-streams into maps ($w_i = 1/\sigma_i^2$). For every bolometer and every section of continuous data, three unnormalized signal maps are created for I, Q and U by adding together the weighted time-streams samples that belong to each pixel (based on the attitude). In addition, three weight maps are also created to hold the sum of all the weights in each pixel. Once all the bolometers and sections of the flight have been processed, all the unnormalized signal maps are added together as well as all the weight maps (for I, Q and U separately). Finally a weighted signal map is produced for I, Q and U by dividing the total unnormalized signal map with the total weight map.

8.9.5 Results

We present here maps generated using the pipeline described above and the full flight dataset for 150 GHz (352 bolometers) and 250 GHz (257 bolometers).

Full sky (Galaxy removed) The maps are created using Healpix NSIDE 512, and then smoothed to 1° and down-sampled to NSIDE=64. Figure 8.12 shows the 150 GHz maps
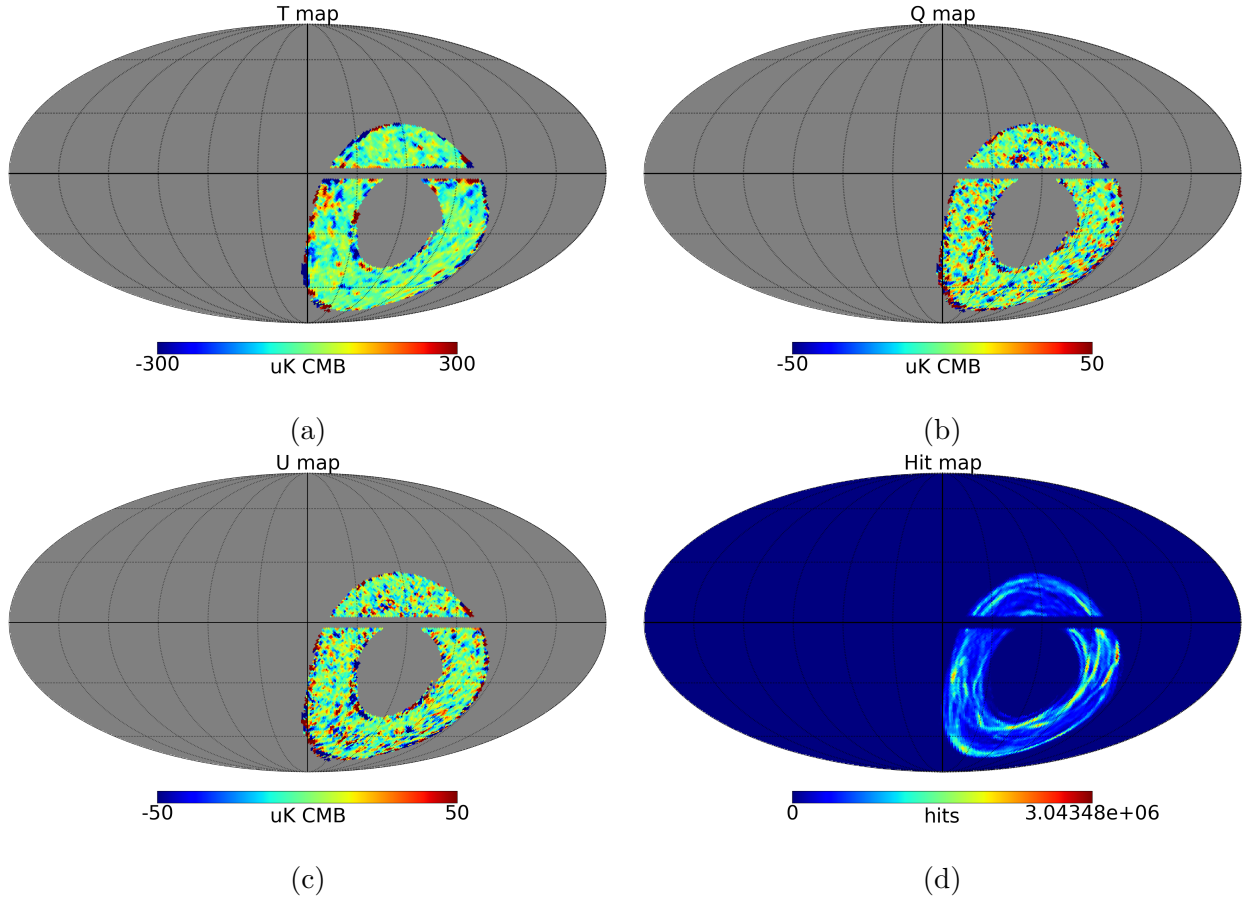
Figure 8.12: Maps of Stokes I (a), Q (b), and U (c) parameters generated with EBEX LD2013 150 GHz data. The maps are smoothed to 1° and plotted with Healpix NSIDE 64. The corresponding hit map is shown in (d).

and Figure 8.13 shows the 250 GHz maps, in Galactic coordinates. The Galaxy is removed before filtering to avoid ringing of the large Galaxy power into neighbouring pixels.

Galaxy Figure 8.14 shows I, Q and U maps of the Galaxy for the 150 and 250 GHz datasets, generated with NSIDE 512 and smoothed to the beam size (16′).

RCW38 Figure 8.15 shows 6°x 6° I, Q and U maps of RCW38 for the 150 and 250 GHz datasets, generated with NSIDE 512 and smoothed to the beam size (16′). RCW38 is a compact and bright source in the HII galactic region, known to have less than 1% of polarization fraction at those frequency bands.
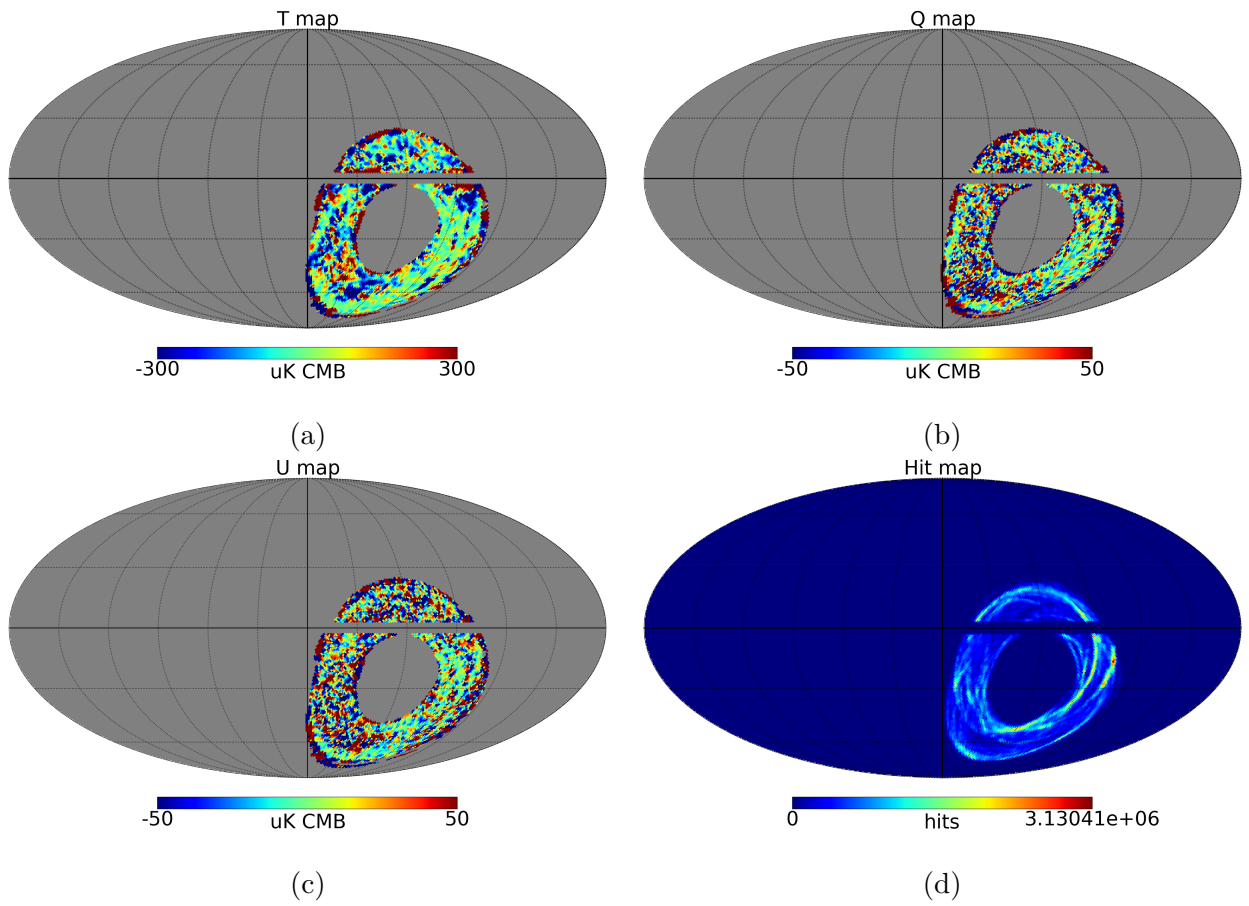
Figure 8.13: Maps of Stokes I (a), Q (b), and U (c) parameters generated with EBEX LD2013 250 GHz data. The maps are smoothed to 1° and plotted with Healpix NSIDE 64. The corresponding hit map is shown in (d).

I

mK

-2   10

Q

mK

-0.1   0.1

U

mK

-0.1   0.1

(a) 150 GHz maps

I

mK

-2   10

Q

mK

-0.5   0.5

U

mK

-0.5   0.5
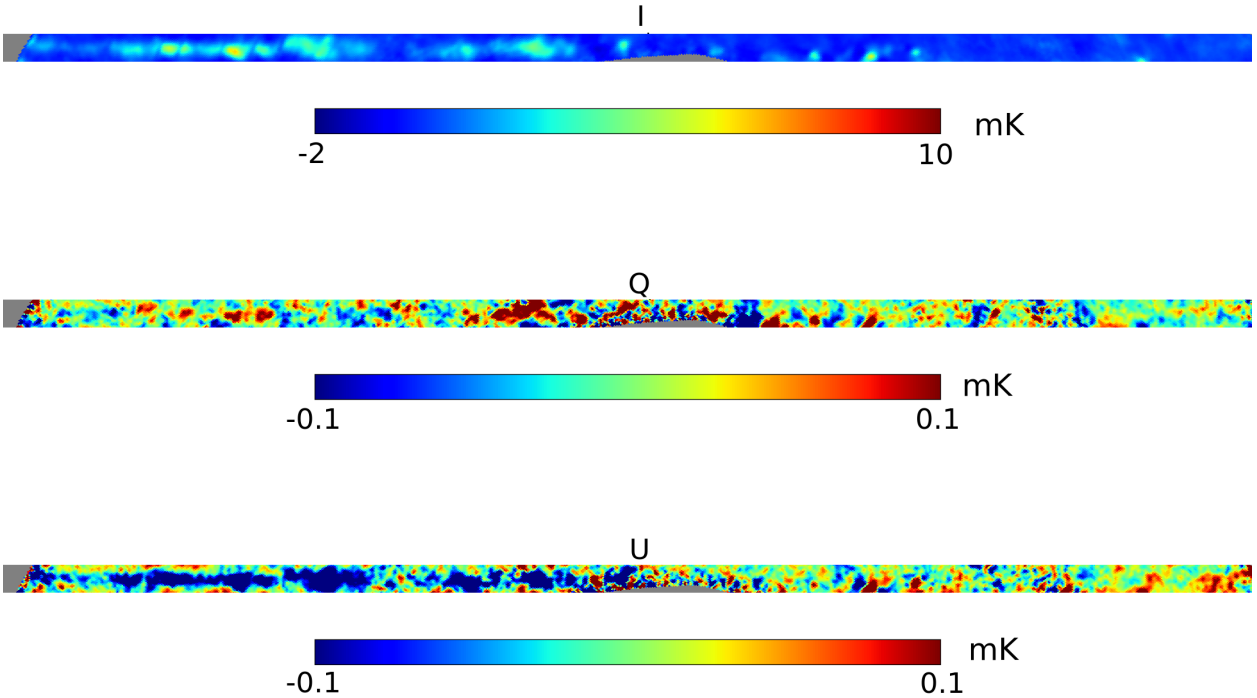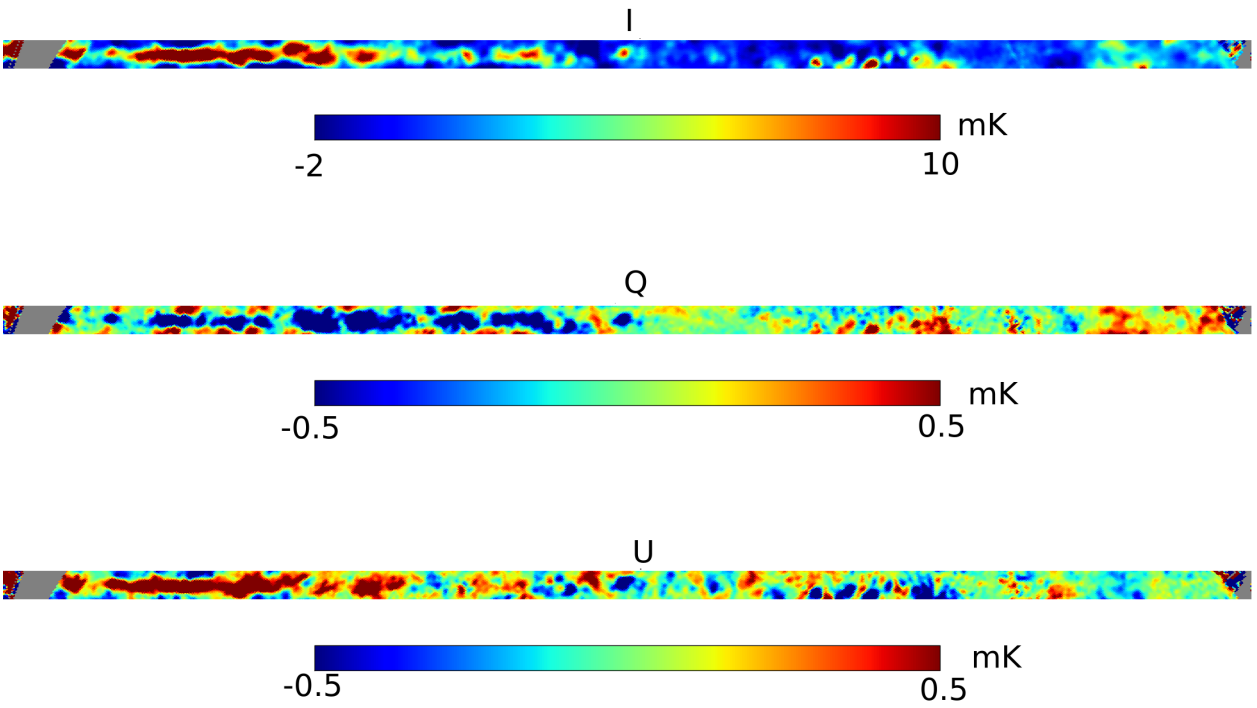
(b) 250 GHz maps

Figure 8.14: Galaxy maps of Stokes I, Q and U parameters generated with EBEX LD2013 data for 150 GHz (a) and 250 GHz (b) bolometers. The maps are smoothed to 16′ and binned with Healpix NSIDE 512.
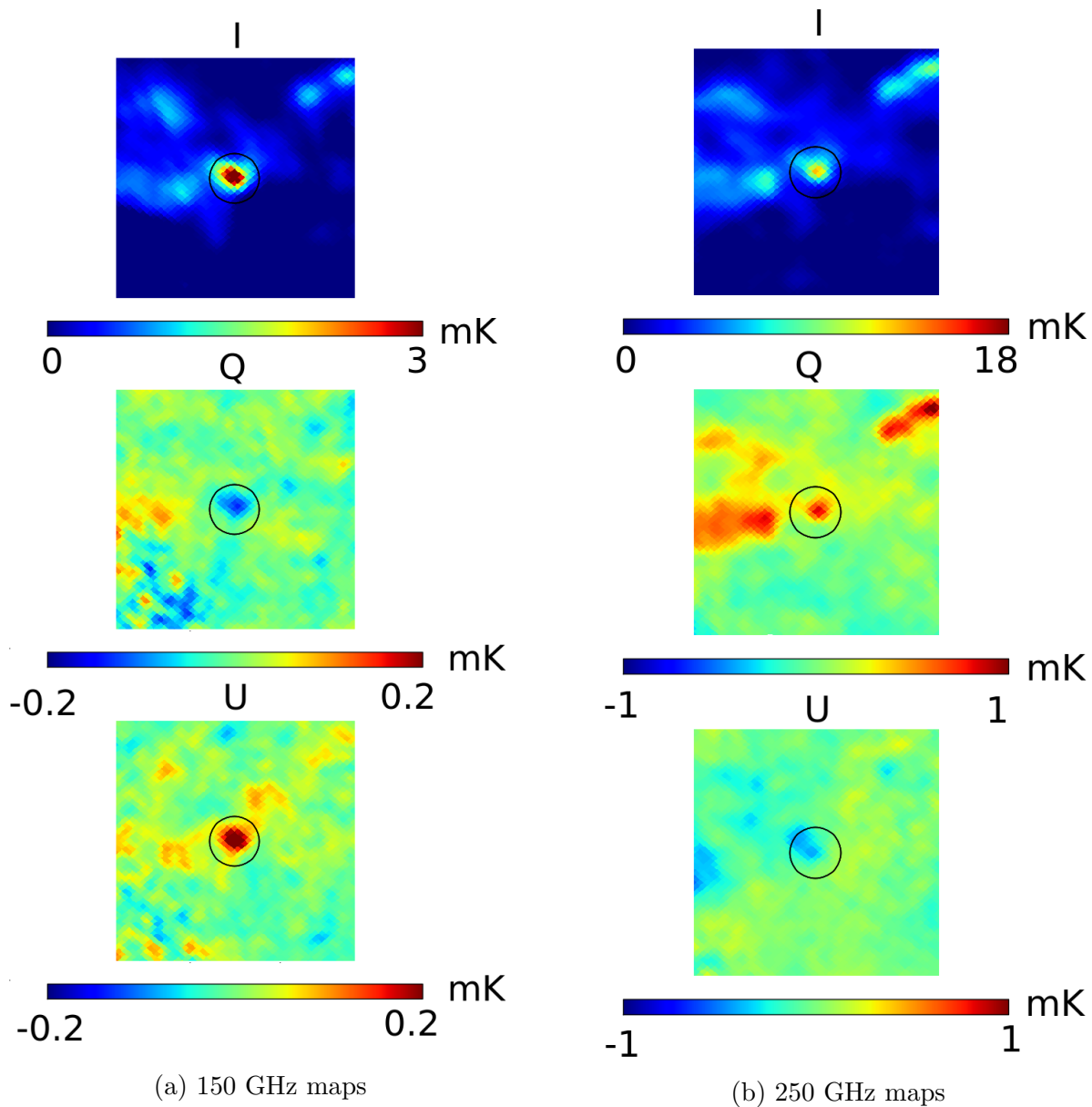
Figure 8.15: RCW38 maps of Stokes I, Q and U parameters generated with EBEX LD2013 data for 150 GHz (a) and 250 GHz (b) bolometers. The maps are smoothed to 16′ and binned with Healpix NSIDE 512. The images shown are 6°x 6° wide centered around (lon, lat) = (-92.1°, -1.1°)

8.9.6   Conclusion and Next steps

Excess polarization is observed in the Galaxy maps, the CMB maps and the RCW38 maps. Study of this excess polarization led to the working hypothesis that instrumental polarization is creating a significant HWP template, which itself is inducing non-linearity in the detector response, creating excess polarization. The characterization and removal of the instrumental polarization is the subject of the next chapter.

After removing the excess polarization, the next steps involve re-generating clean CMB maps of I, Q and U, potentially using one of the more sophisticated map maker currently being adapted for EBEX. Noise covariance matrices also need to be generated through Monte-Carlo simulations to evaluate the error on extracted cosmological parameters.

Once clean Q and U maps are generated, we combine them as $Q + iU$ and $Q - iU$, and do a spherical harmonic decomposition using ladder operators [61]:

$$Q \pm iU = \sum_{l,m} a_{lm}^{\pm 2}[Y_{lm}(\theta, \phi)]$$

E and B-modes are then defined by:

$$E \equiv \sum_{l,m} \left(-\frac{1}{2}(a_{lm}^{(2)} + a_{lm}^{(-2)}) \right) Y_{lm}(\theta, \phi)$$

$$B \equiv \sum_{l,m} \left(-\frac{1}{2i}(a_{lm}^{(2)} - a_{lm}^{(-2)}) \right) Y_{lm}(\theta, \phi)$$

Maps at the three frequency bands are used to estimate the frequency dependence of the foregrounds and remove them. With maps cleaned from foregrounds, we can generate the angular power spectra of the E and B-modes to place an upper limit on the tensor-to-scalar ratio r.

127

Chapter 9

Instrumental Polarization Removal

9.1 Excess Polarization in CMB Stacked Maps

The Galaxy and RCW38 maps presented in the previous section showed excess polarization compared to the expected sky signal. This result prompted us to investigate models of Instrumental Polarization (IP), defined as the polarization of unpolarized light by the instrument (conversion of Stokes I to Stokes Q/U). In this chapter, IP is examined in the **instrument reference frame**, as IP results in Stokes I being converted to Stokes Q/U in a consistent manner **within** the instrument, independently of the telescope Galactic roll.

We use the CMB as a known source to characterize the excess polarization. We are interested in the correlation between temperature and polarization, and use the "stacked map" technique first described in [11] to study this correlation. Stacked I, Q and U maps are produced with the following algorithm:

1. Start from I, Q and U sky maps, smoothed to 0.5°, with the Galaxy masked out

2. Identify the locations of the hot (or cold) spots in CMB I. This is done by checking, for each pixel, the value of all the neighbouring pixels. If the pixel being checked is the largest (smallest) of all the neighbours, and it has positive (negative) Stokes I, mark the pixel as a hot (cold) spot location.

3. Extract a square region of 5°×5° around each temperature cold or hot spot.

4. Coadd the extracted images for I, Q and U.

5. Remove monopoles from the co-added Q and U maps.

As an example, we provide in Figure 9.1 the stacked maps obtained from the above algorithm for cold spots, using as input Planck CMB full sky maps[1]. The peak of the CMB temperature power spectrum at $\sim 1°$ is visible in the size of the spot in the I stacked map (left). Q (center) and U (right) stacked maps show quadrupolar structures coming from the CMB E-modes. Note that the center of the stacked Q and U maps have no power, showing there is no correlation between I and Q/U at zero angular separation. This is useful to measure IP.
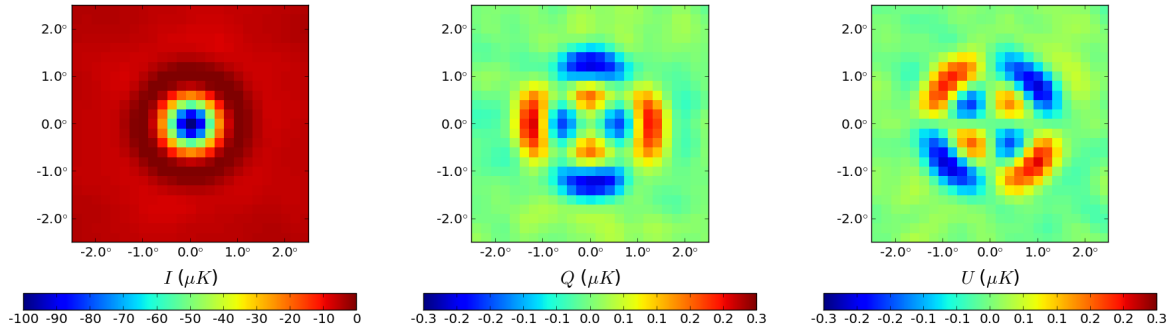
Figure 9.1: I, Q and U stacked maps made using colds spots CMB Planck maps. Around $\sim 14,000$ spots are stacked together.

To simulate the expected corresponding signal in the EBEX maps, we perform a similar analysis but using as input sky the Planck Sky Model, integrated over the EBEX 150 GHz bandwidth (i.e. using the full sky instead of the component separated CMB). In addition, we use the simulation app and LD2013 attitude to generate I, Q and U (noiseless) time-streams for all 150 GHz bolometers scanning this sky, and then reconstruct the maps using our map making pipeline. In this manner, the effects of filtering and of partial sky coverage (fewer cold spots being available) are included , as shown in Figure 9.2a. Finally, we use the I, Q and U time-streams to reconstruct the maps in the instrument frame instead of the sky frame,

---

[1] http://pla.esac.esa.int/pla/#maps

and show the result in Figure 9.2b. The CMB polarization is no longer apparent because as the telescope scans a pixel with multiple Galactic roll angles, CMB Q and U average down in the instrument frame. This reference frame is useful when trying to measure IP both because the sky polarization averages down and the IP does not.

(a) Sky Frame

(b) Instrument Frame
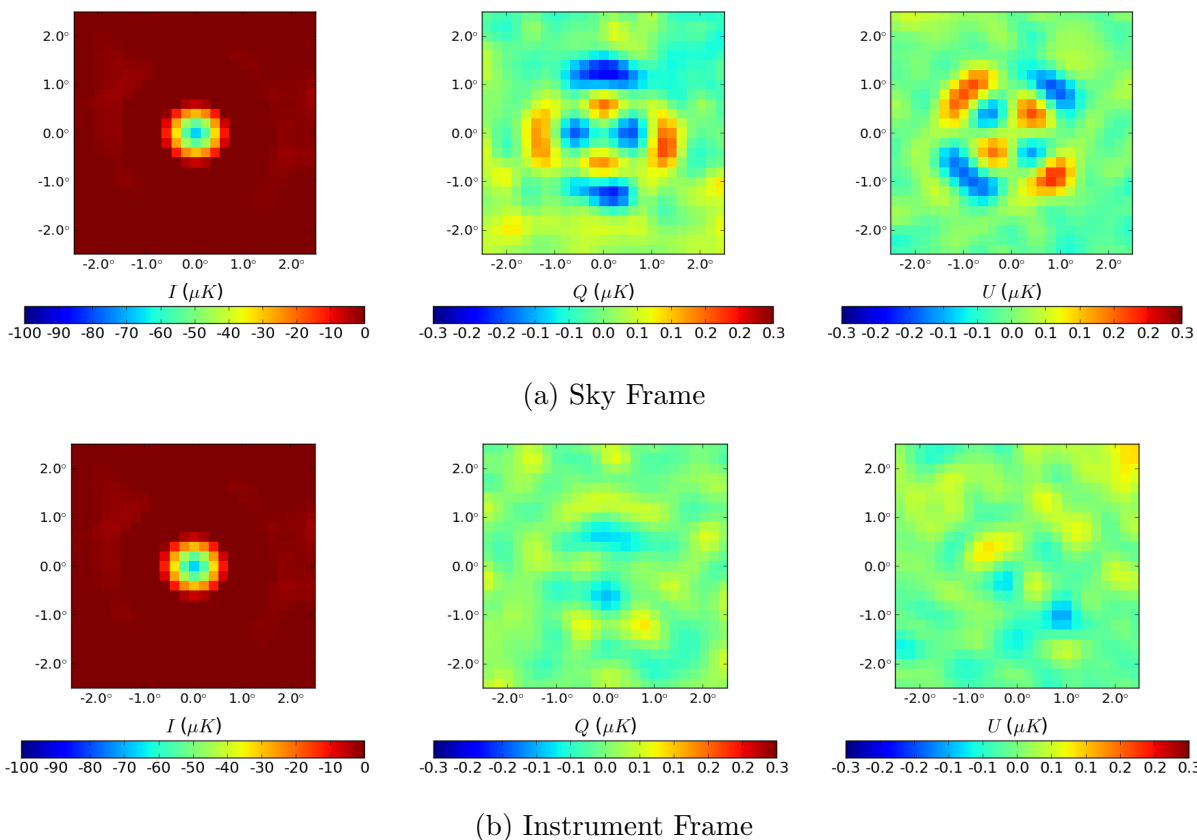
Figure 9.2: Stacked maps generated from simulated EBEX noiseless time-streams (150 GHz bolometers). Approximatively 2,240 cold spots are co-added. The input sky is the Planck Sky Model integrated over the EBEX bandwidth. The CMB E-modes are the source of the quadrupolar patterns observable in the Q and U stacked maps from Figure a. In Figure b, the stacked maps are generated in the instrument frame, and the CMB polarization is averaged down from repeated passes over a given pixel with multiple Galactic roll angles.

We now apply this analysis to maps generated from EBEX LD2013 time-streams, for both 150 and 250 GHz bolometers. Note that the location of the cold and hot spots are determined using Planck CMB maps and not EBEX data. The EBEX I, Q and U maps are generated in the instrument frame. The result is shown in Figures 9.3 and 9.4. In both
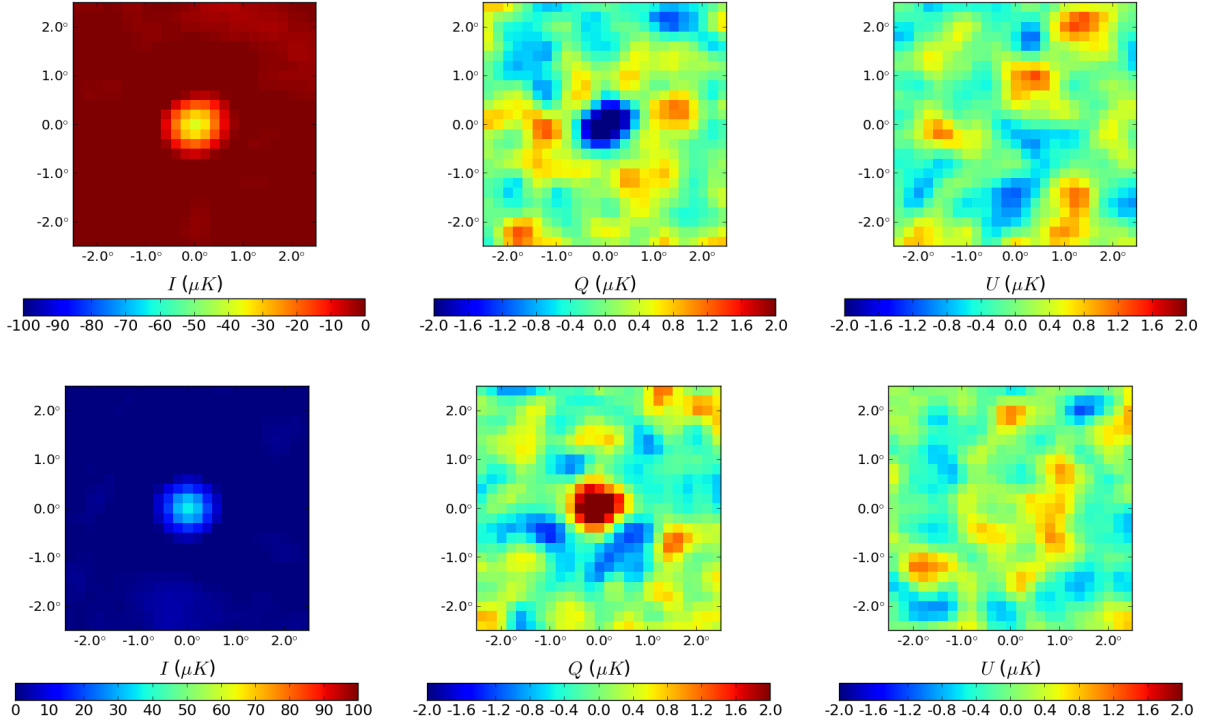
Figure 9.3: Cold (top) and hot (bottom) spot stacked maps generated in the instrument frame from LD2013 EBEX 150 GHz time-streams. Approximatively 2,240 cold (and hot) spots are added. The I stacked map shows the CMB anisotropies. Stacked Q and U maps exhibit a similar pattern from the I map, showing there is a leakage from I to polarization in EBEX data. N.B: It is a coincidence that all the polarization power shows up in Q when co-adding all 150 GHz detectors, as we will show in later sections.

figures we observe in the I stacked maps the CMB T anisotropies measured by EBEX. The presence of a similarly shaped spot in the Q and U stacked maps is direct evidence of I leaking into Q and U from IP. The two Q (or U) spots corresponding to cold or hot I spots are of opposite magnitude, as is anticipated if I leaks into Q (or U). The average I to P leakage measured is 8.5% for 150 GHz and 18% for 250 GHz.

In the next section, we develop a model explaining the observed IP after which we detail a method to measure and remove the IP on a bolometer per bolometer basis.

131
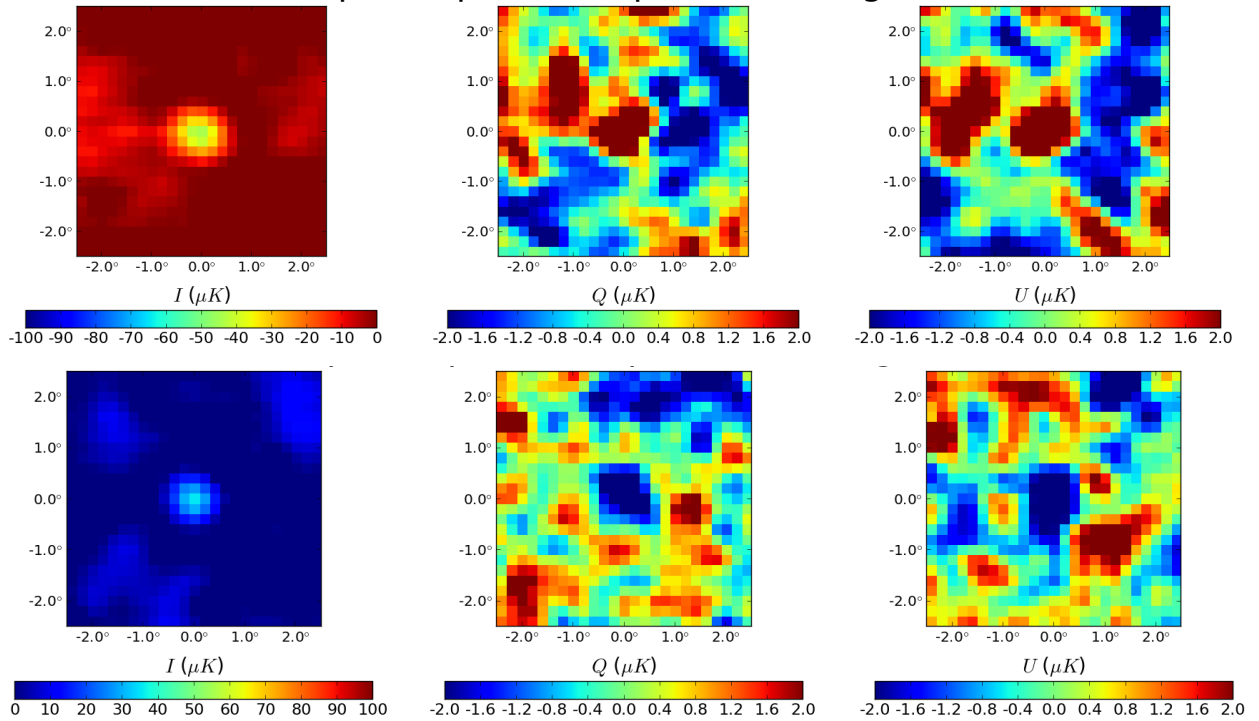
Figure 9.4: Cold (top) and hot (bottom) spot stacked maps generated in the instrument frame from LD2013 EBEX 250 GHz time-streams. Approximatively 2,240 cold (and hot) spots are added. The I stacked map shows the CMB anisotropies. Stacked Q and U maps exhibit a similar pattern from the I map, showing there is a leakage from I to polarization in EBEX data.

9.2   Instrumental Polarization Models

In this section we present two models attempting to explain the observed leakage of I to polarization in the data. We call instrumental polarization (IP) *any* instrumental process by which unpolarized light appears as polarization in the detector time-stream. We call **optical** IP the process by which an optical element creates physical polarization in the radiation incident on the detectors. In addition, it is useful to differentiate two types of polarized signal measured by the detectors, differentiated by their bandwidth:

- **HWP template 4th harmonic**: this is the polarized radiation that is stationary in the instrument frame and has a very narrow bandwidth located at $4f_{hwp}$. This radiation is either polarized emissions from the instrument, or unpolarized emission from the instrument that is polarized by IP.

- **Polarized radiation in the "signal" bandwidth**: This radiation originates from the sky, and is therefore modulated by the scanning strategy and has a large bandwidth centered around $4f_{hwp}$. This radiation is either polarized emission from the sky, or unpolarized emission from the sky that is polarized by IP.

9.2.1   Instrumental Polarization through a di-attenuator

Modelling the instrument with the optical design software Code V[2] shows that the main source of optical IP in the instrument is the field lens. The field lens is shown in the ray tracing diagram in Figure 2.2. In this section we detail the properties of a field lens induced IP, and explore the viability of this model as a source for the excessive polarization observed in the CMB and the Galaxy. We also show that given the behavior (presented in this section) of the phase ϕ_d and amplitude A_d of the HWP template 4th harmonic for each detector, the template is well modelled by instrument-emitted unpolarized light that gets polarized by the field lens.

---

[2]`https://optics.synopsys.com/codev/`

A di-attenuator polarizes light because of differential transmittance along the "in-plane" and "out-of-plane" direction from the incident light. Let us call x-y the plane of the di-attenuator (the field lens). The Mueller matrix of a di-attenuator with in-plane direction forming an angle α with the x-axis is:

$$
G(\alpha) = \frac{1}{2} R(-\alpha)
\begin{pmatrix}
\eta & \varepsilon & 0 & 0 \\
\varepsilon & \eta & 0 & 0 \\
0 & 0 & \sqrt{\eta^2 - \varepsilon^2} & 0 \\
0 & 0 & \sqrt{\eta^2 - \varepsilon^2} & 0
\end{pmatrix}
R(\alpha)
$$

where $R(\alpha)$ is the rotation described in Section 8.2.2, $\eta \sim 2$ is the sum of the transmittances along the two perpendicular axis and $\varepsilon \sim 0$ is the difference between the transmittances of the two axis. Note that ε increases as the angle of incident light increases, producing more IP at the edge of the field lens than in the center. Using an index of refraction $n \sim 1.5$ for the lens, and ignoring the AR coating, we calculate that at the edge of the lens where the effect is maximum, $\eta \sim 1.8$ and $\varepsilon \sim 0.2$. Applying this Mueller matrix to incoming unpolarized light and using our data model in Equation 8.7 we have:

$$
\vec{S}_{out} = M_{lpx} \, G(\alpha) \, M_{hwp}(\gamma)
\begin{pmatrix}
I_{in} \\
0 \\
0 \\
0
\end{pmatrix}
$$

$$
s^{IP}(t) = \frac{1}{2} I_{in} \left(\eta + \varepsilon \cos(4\psi - 2\alpha) \right) \tag{9.1}
$$

Any unpolarized radiation incident on the field lens at a location forming an angle α with the x-axis, and radius r, will produce in the corresponding illuminated detector a polarization

134

signal, correlated with the unpolarized radiation I_{in}, with polarization fraction $\varepsilon(r)$ and polarization angle α. Because the field lens is **located at an image of the focal plane**, the corresponding illuminated detector **is** the detector with radius r and **polar angle α**. Therefore each detector will see IP with polarization angle α equal to the polar angle ρ of the detector position on the focal plane.

HWP Template Observations

If the HWP template is dominated by field lens IP acting on unpolarized light emitted by the instrument, the polarization angle of the HWP 4th harmonic for each detector should be equal to the detector polar angle ρ. Figure 9.5 shows this is exactly what we observe (modulo a negative sign coming from different conventions for α and ρ). The small constant offset between α and ρ apparent in the figure comes from other sources of the HWP template, likely the primary mirror emitting polarized light. We also show in Figure 9.6 that the HWP template magnitude increases towards the edge of the focal plane, as predicted by the field lens IP model. Finally, Code V models for EBEX predict at maximum 2-3% of IP fraction from the field lens. Given the magnitude of the CMB monopole and the emissivity of the optical components sky side of the field lens (mirrors, window and filters), 2-3% IP will produce a template with magnitude $\sim$3-4 K. This is in agreement with the magnitude of the HWP template observed, as shown in Figure 9.6. In conclusion, the shape and amplitude of the observed HWP template 4th harmonic are in agreement with predictions from the field lens IP model, strongly supporting the hypothesis that this is the dominant source for the HWP template.

Signal Bandwidth Observations

The field lens IP is a coherent model to explain the origin of the HWP template 4th harmonic. Is the field lens IP also the mechanism causing excessive polarization in the signal bandwidth? Measurements of the CMB spots or of RCW38 polarization consistently show $\sim$8% of IP

fraction for the 150 GHz averaged measurement and ~18% IP fraction for the 250 GHz measurements, which is much stronger than the 2-3% IP fraction predicted by Code V. In addition, we will show in Section 9.3.1 that in the signal bandwidth in the instrument frame, we observe an excess polarization angle offset by 90° from the polarization angle expected from filed lens IP (i.e., we find $\alpha^{IP} = \rho + 90°$ instead of $\alpha^{IP} = \rho$). These observations prompt us to present an additional model for the source of the excess polarization, that we describe in the following section along with its effects on the observed signal. In Section 9.3.1, we use LD2013 measurements to differentiate between the two models and conclude that signal bandwidth excess polarization is caused by this second model.

9.2.2 Instrumental Polarization through Non-Linearity

The PSD of raw bolometer data, as shown for example in blue in Figure 8.5, shows significant power at *all* of the HWP rotation rate harmonics. This could in principle be caused by HWP emissions at all harmonics, but it could also be the signature of a non-linear detector response. In this case the template would initially be composed of fewer, physically motivated harmonics (like harmonics 1, 2 and 4), and the non-linear response causes the resulting PSD to exhibit a multitude of higher harmonics. An example of this effect on simulated data is shown in Figure 9.7 b. The non-linear response could be caused by the strong HWP template amplitude of several K_{CMB} incident on the detectors.

We investigate the effects of a non-linear response on the extraction of the I, Q and U time-streams using the plots in Figure 9.8. The plots simulate the scanning of an **unpolarized** Gaussian source I^{sky} with detector non-linearity. The detector signal is modelled as:

$$s_{out}^{NL}(t) = f_{nl}(\frac{1}{2} I^{sky} + A_4 \cos(4\gamma + \phi_4)) \tag{9.2}$$

where the green elements correspond to a simplified 4th harmonic only HWP template, I^{sky} is the unpolarized sky source, and f_{nl} is a non-linear response function modelled by
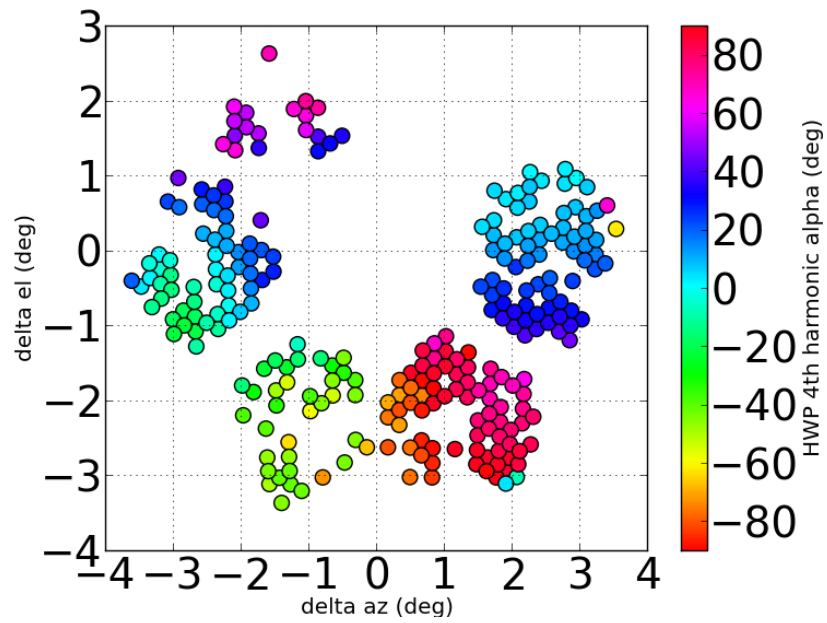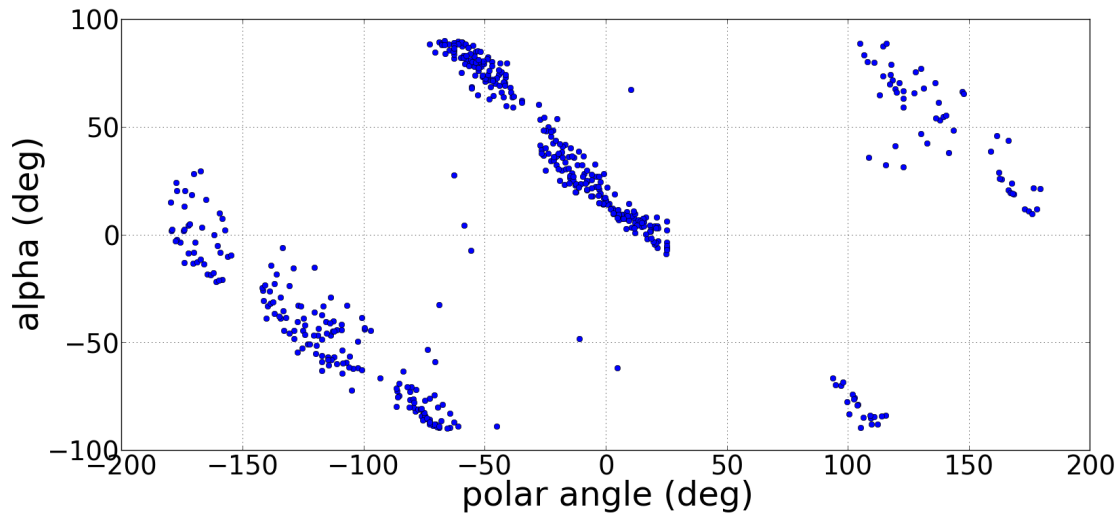
Figure 9.5: (a) Plot of bolometers on focal plane V, with color-scale indicating the polarization angle α measured from the HWP template 4th harmonic. (b) Polarization angle α of the HWP template 4th harmonic for all bolometers, plotted against the bolometer polar angle ρ on the focal plane, showing strong 1:1 linear correlation between α and ρ (the negative slopes comes from using different conventions for α and ρ).
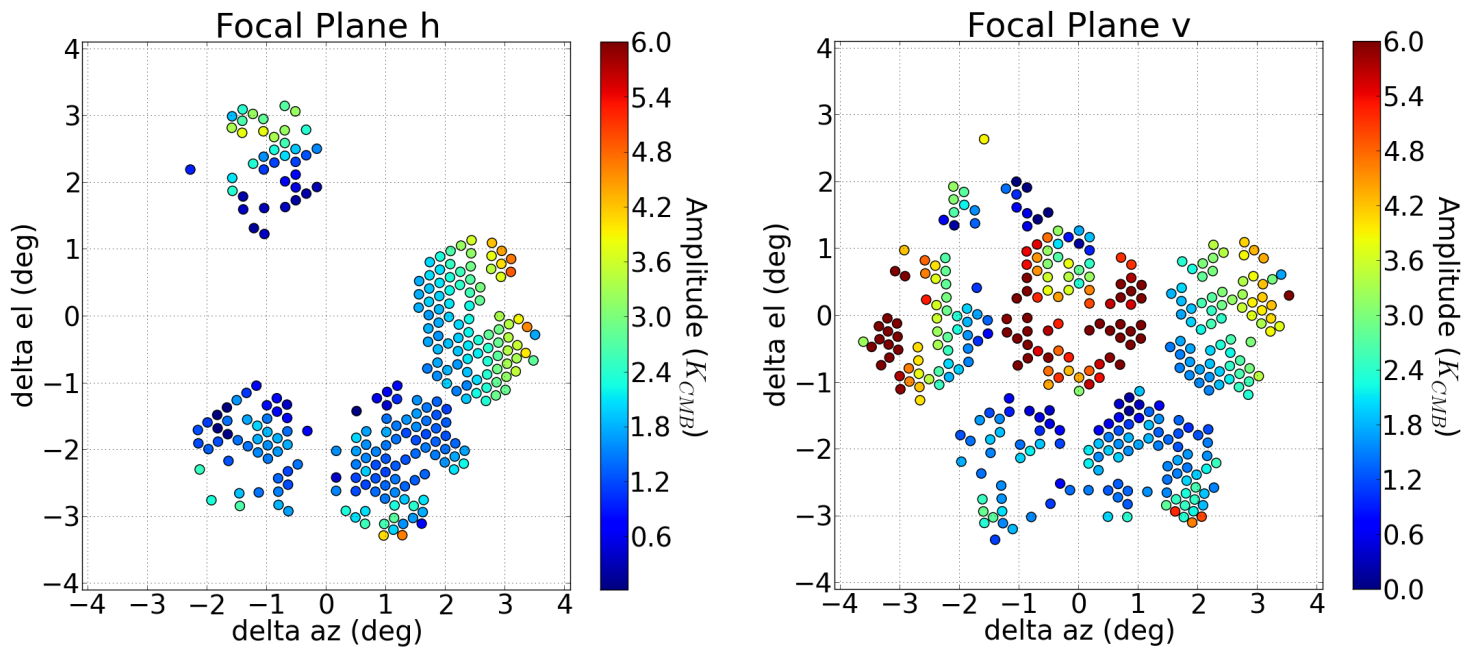
Figure 9.6: Plot of bolometers on focal planes H and V, with the color-scale indicating the amplitude (in K_{CMB}) of the HWP template 4th harmonic. With the exception of the 410 GHz bolometers in the center, the amplitude of the template increases with bolometer radius.

a hyperbolic tangent with response curve plotted in Figure 9.7 a. Figure 9.8 contains six panels showing the simulated and extracted temperature, polarization and HWP signals against time. Panel (a) shows the input sky signal I^{sky} (red), the non-linear response after template subtraction (blue) and the I time-stream extracted from $s_{out}^{NL}(t)$ (cyan). Panel (c) shows the input HWP template composed solely of the 4th harmonic (green). Panel (b), (d) and (f) on the right side show the input sky Q, U and polarization power P (red) and the Q, U and P time-stream extracted from $s_{out}^{NL}(t)$ (cyan). Panel (e) shows the HWP 4th harmonic polarization angle (green) and the polarization angle extracted from $s_{out}^{NL}(t)$ (cyan). Note that the sky polarization angle is not plotted because it is not defined, as the input sky power is unpolarized in our simulation.
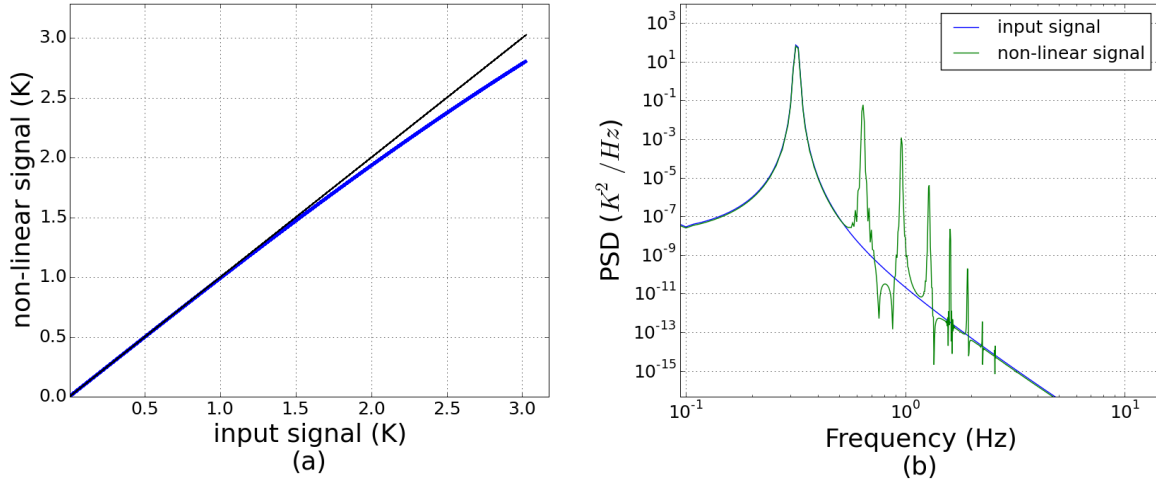
Figure 9.7: Hyperbolic tangent non-linear response function used in the simple simulation of Figure 9.8. (a) Non linear response plotted against the input signal (blue). (b) PSD of the input signal (blue) and the non-linear response (green). In this simulation, the input HWP template only has power at the 4th harmonic. The non-linear response exhibits power at a multitude of higher harmonics.

It is apparent from the non-linear response curve that the input I^{sky} signal will be maximally compressed when the HWP template is maximum, and minimally compressed when the HWP template is minimum, as the signal incident on the detectors (the "input signal") is the sum of I^{sky} and the HWP template. Once template removal has been applied to s_{out}^{NL}, the

template subtracted signal (blue line in Figure 9.8 a) shows a $4f_{hwp}$ component modulated by I^{sky} even though the input I^{sky} signal is unpolarized. Moreover, this $\sim 4f_{hwp}$ component is exactly out of phase with the template 4th harmonic, because the compression is maximum (and the signal minimum) when the template 4th harmonic is maximum. The plots shows in cyan the resulting I, Q and U extracted from the template subtracted time-stream using the procedure described in the previous chapter. The two following effects are apparent from Figure 9.8:

1. Reconstructed I (cyan) is compressed compared to I^{sky} (red)
2. Excess Q and U (cyan) get generated from "I leakage", with polarization angle α (cyan) offset by 90° from the HWP 4th harmonic α angle (green). This corresponds to a 180° offset in phases since $2\alpha = \phi$.

In the case of incoming polarized sky radiation, the Q and U time-stream extracted will show a mix of the input polarization and the leakage polarization, and the polarizations will add up constructively or destructively depending on the relation between the HWP template and the sky polarization angles.

The non-linear model is summarized as follows:

- IP from the field lens creates a HWP template with a strong 4th harmonic component
- The magnitude of the HWP template induces a non-linear response of the detectors synchronous with the HWP template, pushing part of the I signal to the $4f_{hwp}$ bandwidth and inducing a "I to polarization" leakage.
- The polarization angle α of the leakage is offset by 90° from the HWP 4th harmonic polarization angle α.

A good test to separate the non-linear model from the pure field lens model is to compare the polarization angle α measured when scanning an unpolarized sky source with the HWP template polarization angle. If the angles are in-phase, then the excess polarization is dominated by the field lens IP. If the angles are offset by 90°, the excess polarization is dominated

140
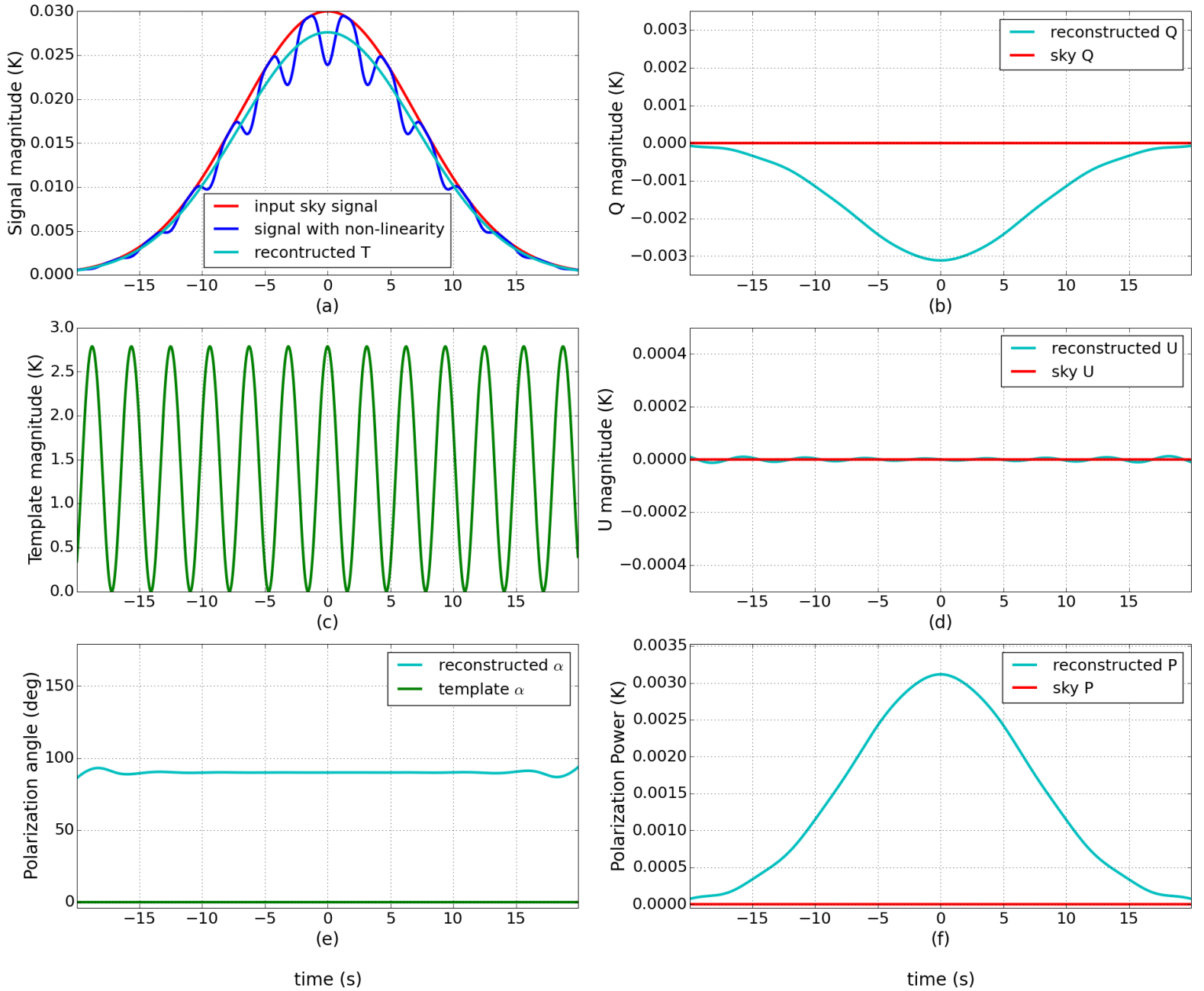
Figure 9.8: Simple simulation of extracted I, Q and U time-streams resulting from scanning an unpolarized source in the presence of a HWP template and detector non-linearity. All time-streams are plotted versus time. (a) Plot of the input sky signal I^{sky} (red), the non-linear response after template subtraction (blue) and the reconstructed I time-stream (cyan). (c) Plot of the input HWP template composed solely of the 4th harmonic (green). (b), (d) and (f) Plots of the input sky Q, U and polarization power P (red) and the reconstructed Q, U and P time-streams (cyan). (e) Polarization angle of the HWP 4th harmonic (green) and the reconstructed polarization time-stream (cyan). Note that the sky polarization angle is not plotted because it is not defined, as the input sky power is unpolarized in our simulation.

141

by detector non-linearity. We perform this test in the next section.

9.3 Characterisation and Removal of the Excess Polarization

9.3.1 Method

General Treatment

To characterize and subtract the excess polarization, we model it as optical IP in the detector time-stream:

$$s^{TOTAL}(t) = s^{det}(t) + s^{IP}(t) \tag{9.3}$$

where $s^{det}(t)$ is the nominal detector model from Equation 8.12 and $s^{IP}(t)$ is described by Equation 9.1. $s^{IP}(t)$ depends on two parameters per detector: the IP fraction ε and the IP angle α^{IP}. Note that if the mechanism creating excess polarization in the time-stream is detector non-linearity, the model used is an approximation, first because we are neglecting the I compression and also because f_{nl} doesn't create polarization with exact shape $I_{in} \cos(4\gamma + 2\alpha^{IP})$. We show by simulations in the following sections that this is a valid approximation.

If we can measure for each detector ε and α^{IP}, we can correct the time-streams from the excess polarization:

$$s^{CORRECTED}(t) = s^{TOTAL}(t) - \frac{1}{2}I^{sky}\left(1 + \varepsilon_{measured}\cos(4\psi - 2\alpha^{IP}_{measured})\right) \tag{9.4}$$

$$\sim s^{det}(t) \tag{9.5}$$

To measure ε and α^{IP} for each detector, we rely on a useful property of $s^{IP}(t)$: it is

coherent in the instrument frame, i.e. the argument in the sinewave does not depend on the telescope Galactic roll ψ. This is in contrast with the polarization from the sky $I^{sky}P^{sky}\cos(4\gamma - 2\alpha^{sky} + 2\psi)$ which averages out when reconstructing the polarization in the instrument frame. We make single bolometer I, Q an U maps of s^{TOTAL} in the instrument frame. Each pixel holds, after demodulation and filtering:

$$I = \frac{\sum_i w_i I_i^{sky}}{\sum_i w_i} = I^{sky} \tag{9.6}$$

$$Q = \frac{\sum_i w_i Q_i^{sky}\cos(2\psi_i)}{\sum_i w_i} + \varepsilon\cos(2\alpha^{IP})\frac{\sum_i w_i I_i^{sky}}{\sum_i w_i}$$

$$\sim \varepsilon\cos(2\alpha^{IP})I^{sky} \tag{9.7}$$

$$U = \frac{\sum_i w_i U_i^{sky}\sin(2\psi_i)}{\sum_i w_i} + \varepsilon\sin(2\alpha^{IP})\frac{\sum_i w_i I_i^{sky}}{\sum_i w_i}$$

$$\sim \varepsilon\cos(2\alpha^{IP})I^{sky} \tag{9.8}$$

where the summation is over all time samples i pertaining to a given pixel and w_i are the map-making weights. For Q and U, the approximate result uses the averaging out of $\sum\cos(2\psi_i)$ for repeated hits with random Galactic roll ψ. The IP parameters are then estimated from the maps using:

$$\varepsilon = \frac{\sqrt{Q^2 + U^2}}{I} \tag{9.9}$$

$$\alpha^{IP} = \frac{1}{2}\arctan\left(\frac{U}{Q}\right)$$

Implementation for EBEX LD2013

To apply the previously described method, it is necessary to find a source with enough signal to noise to be visible by a single bolometer, and enough repeated passes to average out the $\cos(2\psi_i)$ term. Note that for an extended source, it is possible to sum all the pixels within the source, similarly to what is done for the CMB stacked maps. This will increase the signal to noise and the sampling of ψ_i. Alternatively, if one has access to a well sampled unpolarized source, this removes the need to sample the source with many Galactic rolls.

For EBEX, the three possible sources are the CMB, RCW38 and the Galactic plane. Even using stacked maps, our detectors don't have enough sensitivity to measure the CMB individually. RCW38 is sampled with enough signal to noise but poor coverage. This leaves the Galaxy. For every bolometer, we produce instrument frame I, Q and U maps of the Galactic plane following the map making procedure described in Section 8.9, with Healpix NSIDE 256. We define as valid the pixels located within $\pm 3°$ of the Galaxy, and with Stokes I value greater or equal than 3 (15) mK for 150 (250) GHz bolometers. We calculate for each bolometer a single I, Q and U value by averaging all the valid pixels. Using those values and Equation 9.9 we calculate for each bolometer ε and α^{IP}, and plot the results in Figure 9.9.

It is very interesting to note in Figure 9.9 that the measured polarization angle α^{IP} varies linearly with the bolometer polar angle ρ, which is a strong indicator in favor of either direct instrumental polarization in the field lens, or non-linear detector response. To separate between the two models, we plotted in red on the same figure the HWP 4th harmonic polarization angle α. The plot clearly shows α and α^{IP} are offset by 90°, ruling out direct IP in the field lens as the dominant source, and strongly suggesting that detector non-linearity is the dominant source of excess polarization in the signal bandwidth.

9.3.2 Results from Applying the Excess Polarization Removal Method

In the previous section, we developed a method to measure excess polarization and to remove it. We then measured the excess polarization in EBEX LD2013 and concluded that
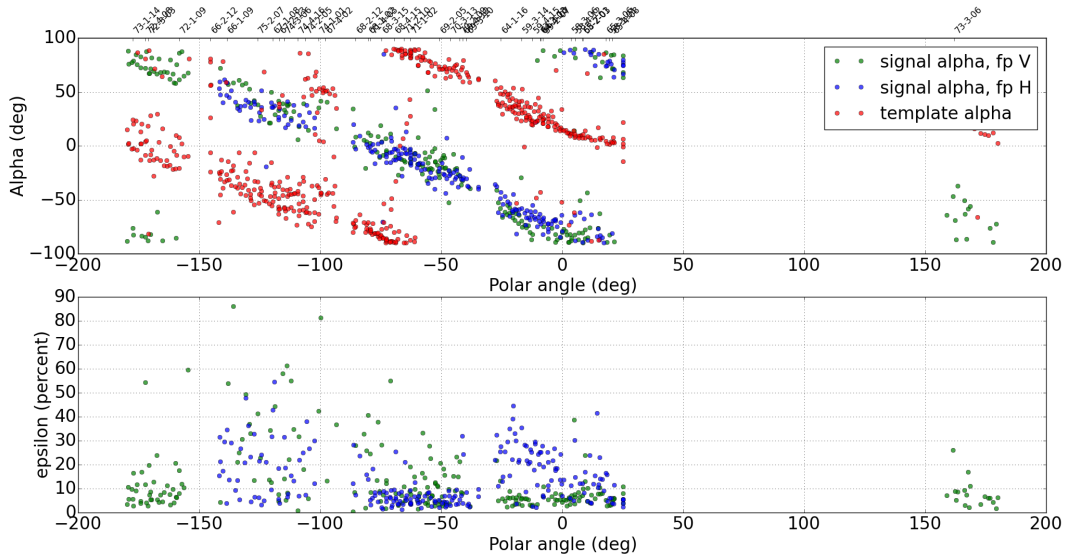
Figure 9.9: Measurement of polarization leakage parameters using the Galaxy. For each bolometer, the measured parameters are plotted against the bolometer polar angle ρ. *Top:* Polarization angle α^{IP} for H focal plane (blue) and V focal plane (green) bolometers. In red is plotted the polarization angle α of the HWP template 4th harmonic, for reference. *Bottom:* IP leakage ε for H focal plane (blue) and V focal plane (green) bolometers

non-linearity in the detectors was the most likely candidate explaining the observed excess polarization. We now describe making maps with the excess polarization removed using Equation 9.4. We first demonstrate the validity of the removal method using simulations of non-linear detector time-streams, after which we make maps of EBEX LD2013 data with the excess polarization removed.

Simulation

The goal of the simulations is to use non-linear time-streams to evaluate the excess polarization removal method by comparing the input maps, the non-linear maps, and the maps with non-linearity removed. We simulate bolometer time-streams using the app described in Section 8.5, and use the app option to simulate non-linear response. Simulations for 150 and 250 GHz bolometers were produced, but only results for the 250 GHz bolometers are presented here for brevity. The non-linear function used is a polynomial of order 3 matching

the non-linear response estimated from real data [62]. Note that before applying a non-linear response, we simulate and add to the bolometer sky signal a HWP template using LD2013 measured coefficients (harmonics 1, 2 and 4), ensuring the template has similar amplitude and focal plane dependence as the real template. The simulations are noiseless.

We use the time-streams to generate instrument frame I, Q and U Galaxy maps and measure the IP parameters using Equation 9.9. We then subtract the measured IP from the time-streams using Equation 9.4, and finally we make sky-frame maps of the cleaned time-stream. We present in Figures 9.10, 9.12 and 9.13 Galaxy maps and CMB stacked maps (sky and instrument frame) comparing three datasets made from the following three simulated time-streams:

- NO non-linearity (the reference)
- non-linearity
- non-linearity removed using measured IP parameters.

Galaxy maps Figure 9.10 shows maps of the Galaxy Q and U using the three datasets. It is interesting to note that for the non-linear dataset, the excess polarization on the galaxy shows a similar pattern (negative Q, positive U) to that of real 250 GHz data in Figure 9.15. This is because we used a realistic HWP template simulation where the polarization angle α varies linearly with the focal plane polar angle ρ. To evaluate the quality of the removal, we construct difference maps between the non-linear and non-linearity removed datasets with the reference, NO non-linearity dataset. Figure 9.11 shows those difference maps and their associated histograms for Q and U. Though the majority of the excess polarization is removed (the standard deviation of the difference maps are reduced by an order of magnitude for both Q and U, as shown in the legend of the histograms), it is apparent that non-linearity removed maps exhibit a lack of power compared to the reference maps. This is likely due to the fact that the method we developed removes the excess polarization, but doesn't account for the fact that non-linearity also compresses the polarization signal, in addition to compressing I

146

and inducing I to P leakage. We are currently investigating how to address this issue.

CMB stacked maps (sky frame and instrument frame)   Figures 9.12 and 9.13 show CMB stacked maps made in the sky and instrument frame for the three datasets. In the sky frame (Figure 9.12), we see that non-linearity creates additional noise and generates Q and U at the center of the spot, distorting completely the CMB E-mode signal. The E-mode pattern re-appears in the non-linearity removed dataset, though with a decreased amplitude. This is again likely due to the fact that the method doesn't account for the fact that non-linearity also compresses the polarization signal. In the instrument frame (Figure 9.13), the central Q and U spots leaked from the I spot are clearly apparent in the non-linear dataset. Note also that the magnitude and angle of the polarization spot created by the non-linear simulation is very similar to that observed in real stacked maps for 250 GHz (see Figure 9.4), again as a consequence of using a realistic HWP template simulation. The disappearance of the polarization spot, created by I to P leakage from non-linearity, is very apparent in the non-linearity removed dataset (Figure 9.13 c). We quantify the excess polarization removal by performing a 2D Gaussian fit of the polarization power spots ($P = \sqrt{Q^2 + U^2}$). The fit for the non-linear dataset produces amplitudes of 4.2 (5.1) µK for hot (cold) spots. A similar fit on the non-linearity removed dataset shows amplitudes of 0.6 (0.6) µK for hot (cold) spots. This shows 86% (89%) of the excess polarization has been removed in the hot (cold) spots. The remaining polarization is likely caused by the error on the fitted ε and α^{IP} parameters.

We conclude that the IP removal method is successful at removing a large portion of the excessive polarization created from I leakage. As anticipated, it doesn't account for the compression of I and Q/U from the non-linear response.

No non-linearity

mK
-1   1

Non-linearity

mK
-1   1

Non-linearity removed

mK
-1   1

(a) Q Maps (sky frame)

No non-linearity

mK
-1   1

Non-linearity

mK
-1   1

Non-linearity removed

mK
-1   1

(b) U maps (sky frame)
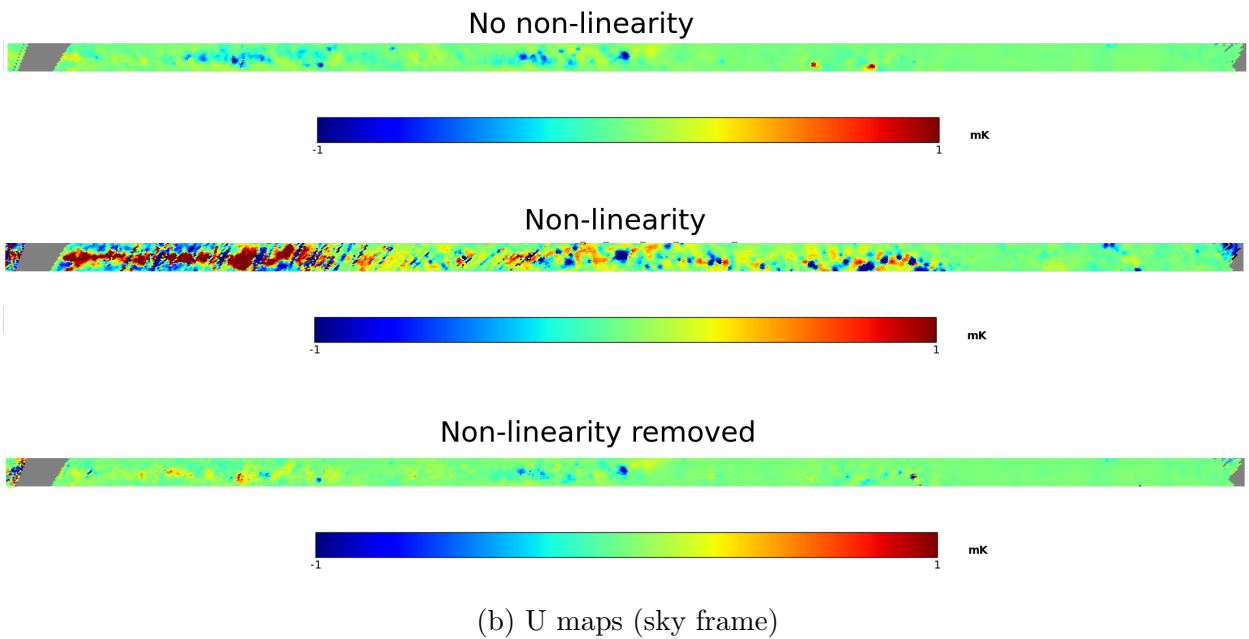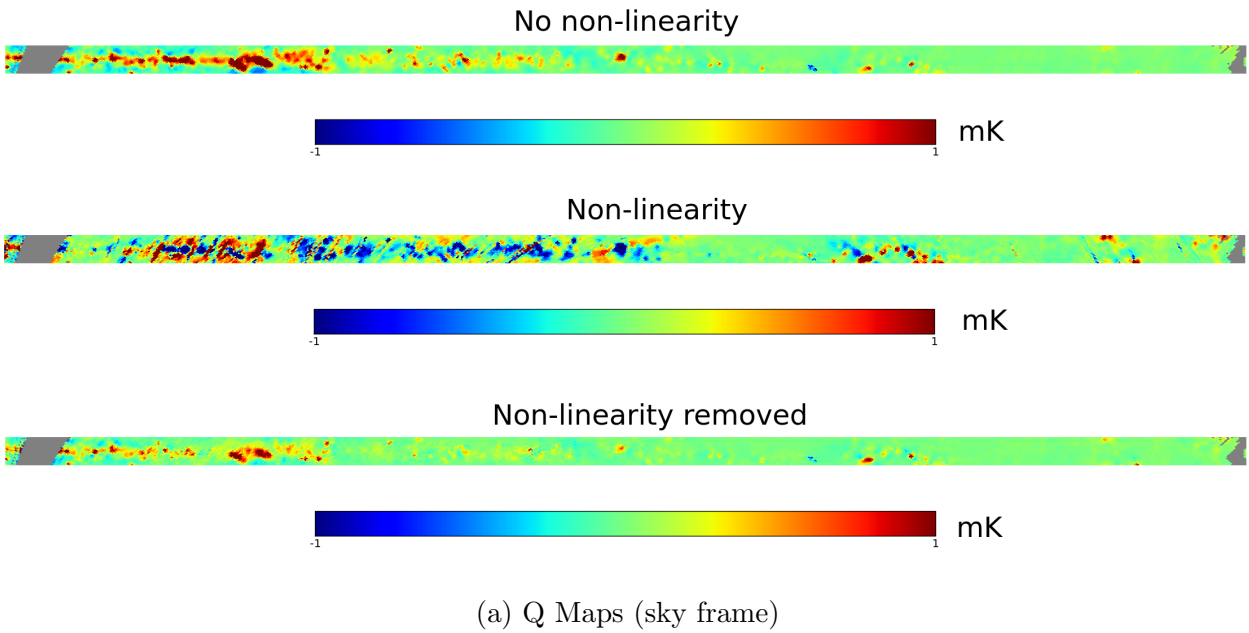
Figure 9.10: Simulated Q (a) and U (b) maps of the Galaxy reconstructed in the sky frame. In each sub-figure, the top and reference map is generated with the NO non-linearity dataset, the middle map is generated using the non-linear time-streams, and the bottom map is generated from non-linearity time-streams with the non-linearity measured and removed.
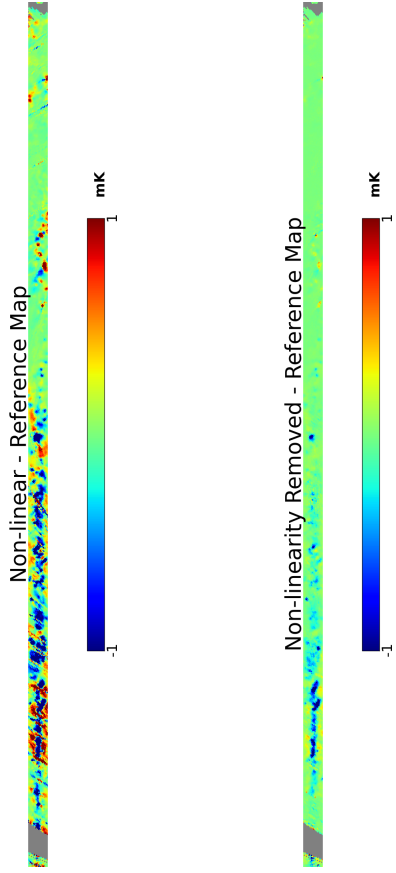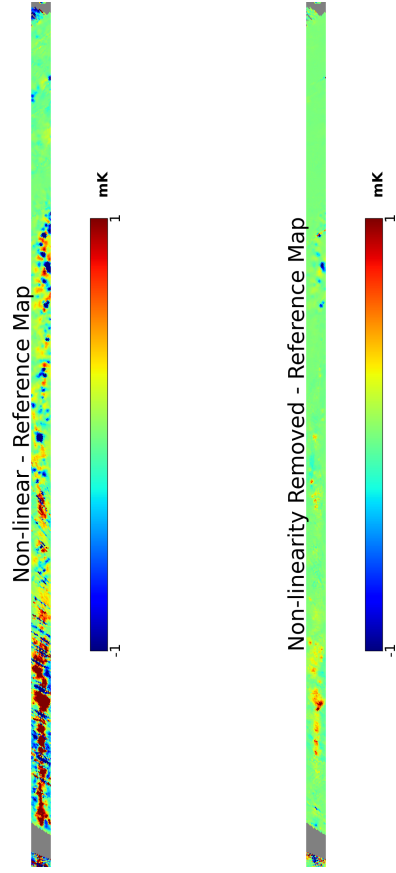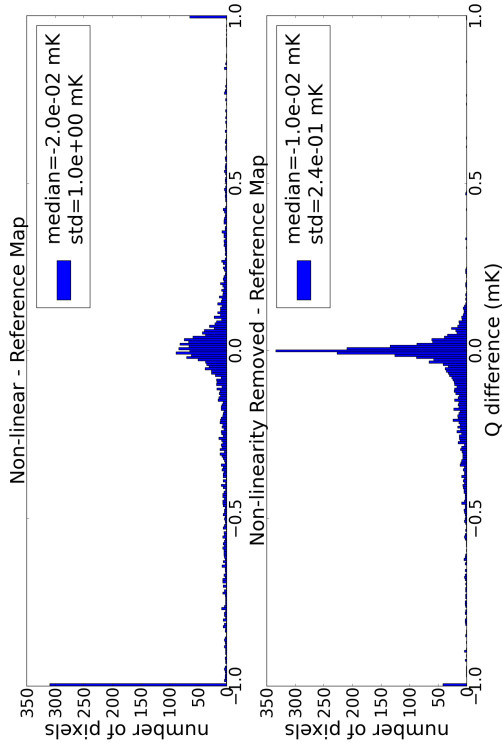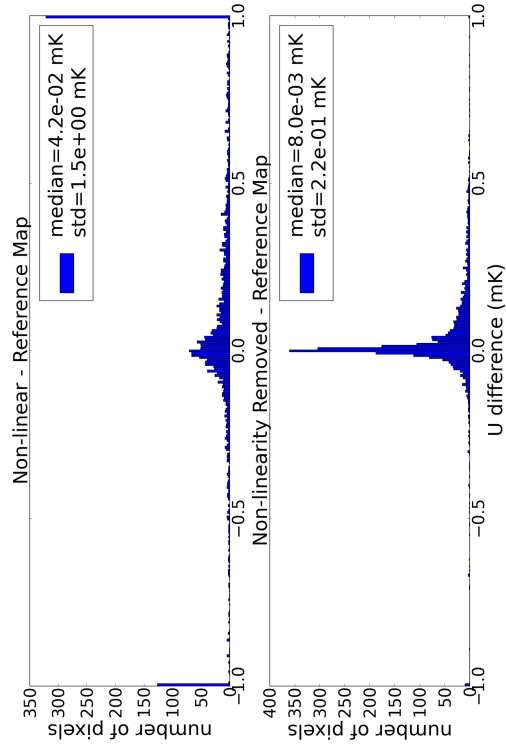
Figure 9.11: *Left:* (a) Q difference maps between the reference dataset and the non-linear (top) and non-linearity removed (bottom) dataset. (c) U difference maps between the reference dataset and the non-linear (top) and non-linearity removed (bottom) dataset. *Right:* Histograms of the corresponding difference maps on the left.
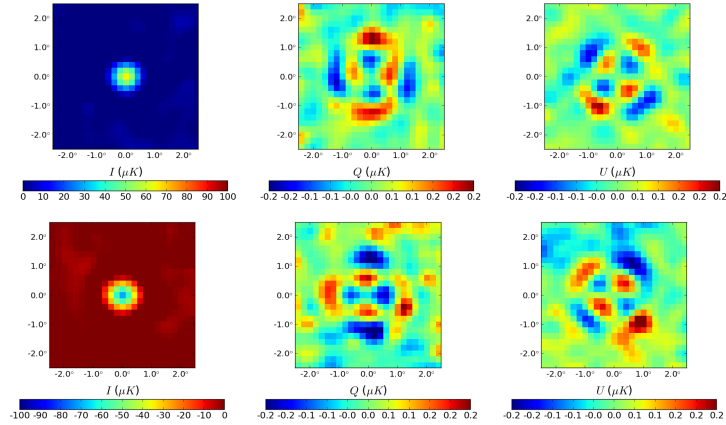
(a) NO non-linearity
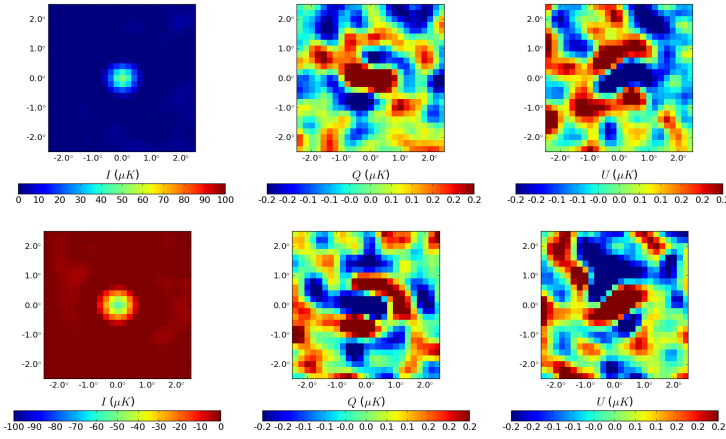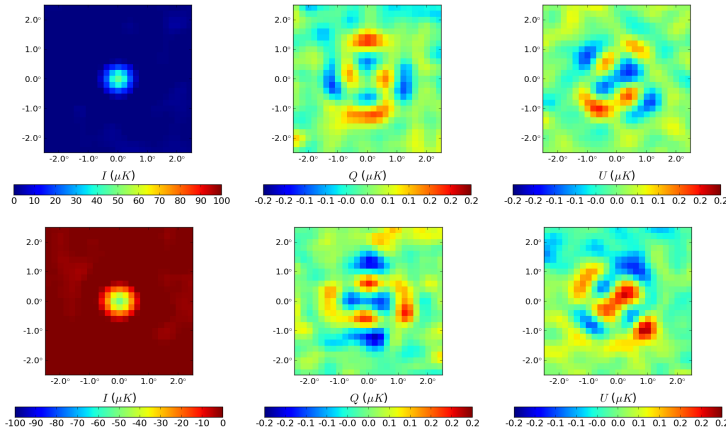
(b) Non-linearity

(c) Non-linearity removed

Figure 9.12: Simulated Stacked CMB cold and hot spots in the sky frame for the three datasets: NO non-linearity (a) non-linearity (b) and non-linearity removed (c).
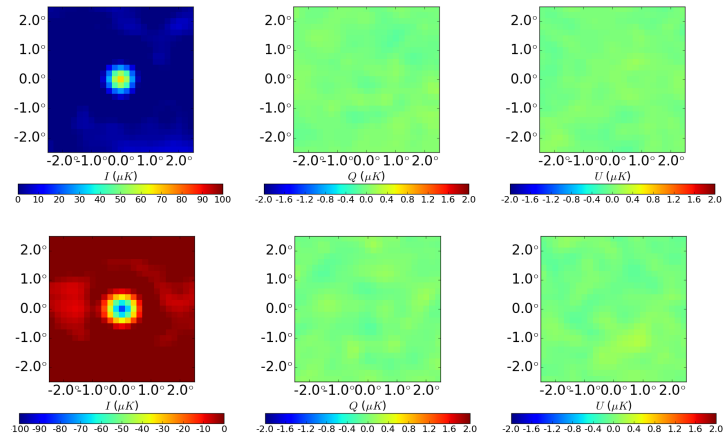
(a) NO non-linearity
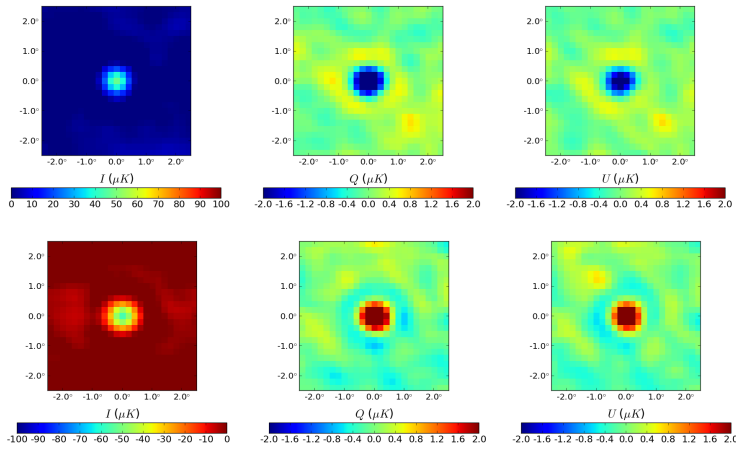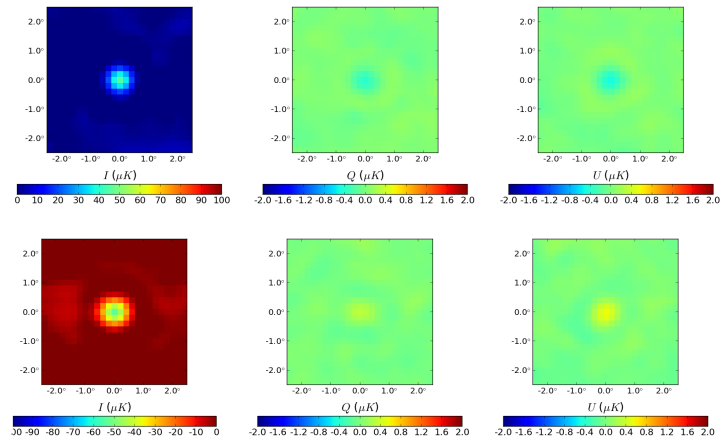
(b) Non-linearity

(c) Non-linearity removed

Figure 9.13: Simulated stacked CMB cold and hot spots in the instrument frame for the three datasets: NO non-linearity (a) non-linearity(b) and non-linearity removed (c).

LD2013 data

The IP removal procedure is applied to EBEX LD2013 data, for both 150 and 250 GHz bolometers. For each detector, the ε and α^{IP} parameter measured is plotted in Figure 9.9. Note that we tried variations around using those parameters, like interpolating the α^{IP} as a function of the polar angle ρ and using the interpolation rather than the individual measurements. We also considered using $\alpha^{IP} = \alpha_{hwp} + 90°$, which is the origin of α^{IP} in the non-linear model. All those methods give similar results. The latter method has the added advantage that if the template phase varies with time (for example from temperature variations in the instrument), the α^{IP} parameter will also vary and this will be reflected by using $\alpha^{IP} = \alpha_{hwp} + 90°$.

We present Galaxy maps generated before and after removal for 150 GHz (Figure 9.14) and 250 GHz (Figure 9.15) bolometers. A large portion of the excess polarization (especially apparent in U) is removed. We are currently investigating why the Galaxy still show some excess polarization after removal.

In Figure 9.16, we show the CMB stacked maps in the instrument frame, for 150 and 250 GHz, after excess polarization removal. These stacked maps should be compared to Figures 9.3 and 9.4 containing the stacked maps before polarization removal. This is a good test of the quality of the removal as it uses a separate dataset (CMB) than is used to compute the IP parameters (Galaxy). To quantify the amount of excess polarization removed, we fit a 2D Gaussian to the polarization power stacked maps, before and after removal, and use the ratio of the fitted amplitudes. The 150 GHz data shows 58% (67%) of the polarization is removed for the cold (hot) spots. The 250 GHz data shows 87% (99%) of the polarization is removed for the cold (hot) spots. To visualize those results, we plot the polarization power P as a function of the distance from the center of the spots (i.e. we use the stacked maps and average all P measurements at a given radius r). We do this for datasets before and after polarization removal, and show the data in Figure 9.17. It is not yet understood why the removal method is less successful on 150 GHz data. One possible explanation is

that the Galaxy being less strong at 150 GHz, the estimated IP parameters have a larger uncertainty. In addition, the 150 GHz bolometers exhibit less non-linearity initially. We are currently working on improving the removal method, and in particular on uncompressing the polarization power after the I leakage has been removed. We do not present the CMB stacked maps in the sky frame as the CMB polarization is not apparent in them, for reasons currently being investigated.

Conclusion and Next Steps

We presented a novel method to measure and remove excess polarization in the data, whether it is generated by optical IP or detector non-linearity. If the origin of the excess polarization is non-linearity, the I and Q/U compression still need to be accounted for after the excess polarization has been removed. We are currently investigating how to do this for EBEX LD2013 data.
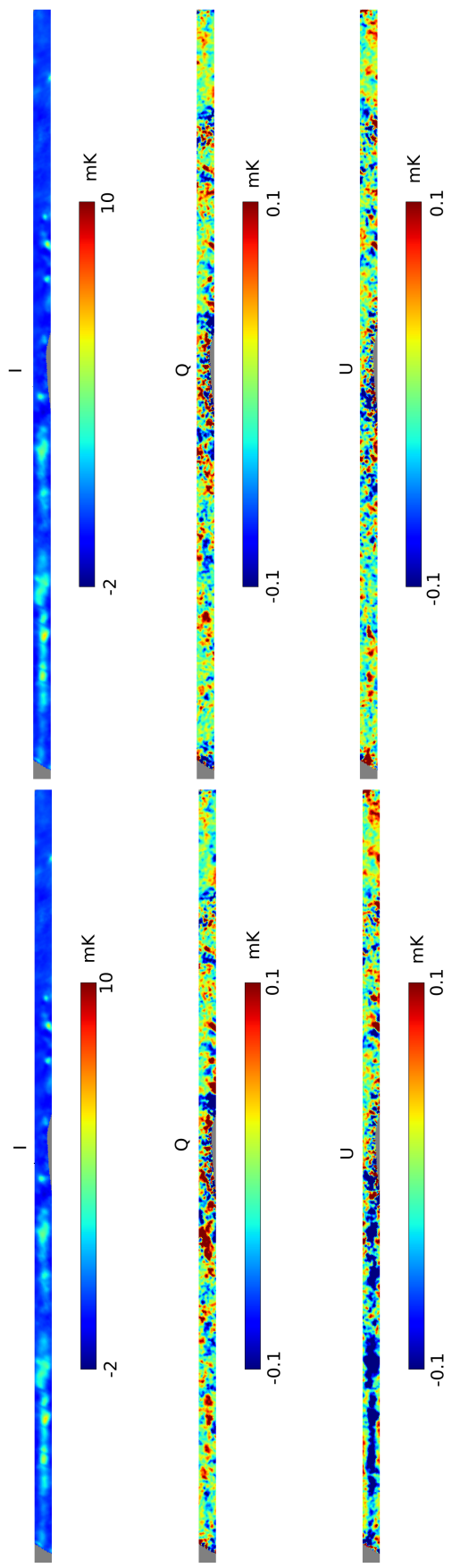
Figure 9.14: I, Q and U Galaxy maps in the sky frame for LD2013 150 GHz bolometers, before (*left*) and after (*right*) removal of the excess polarization. The maps are generated for NSIDE 512 and smoothed to 16'.
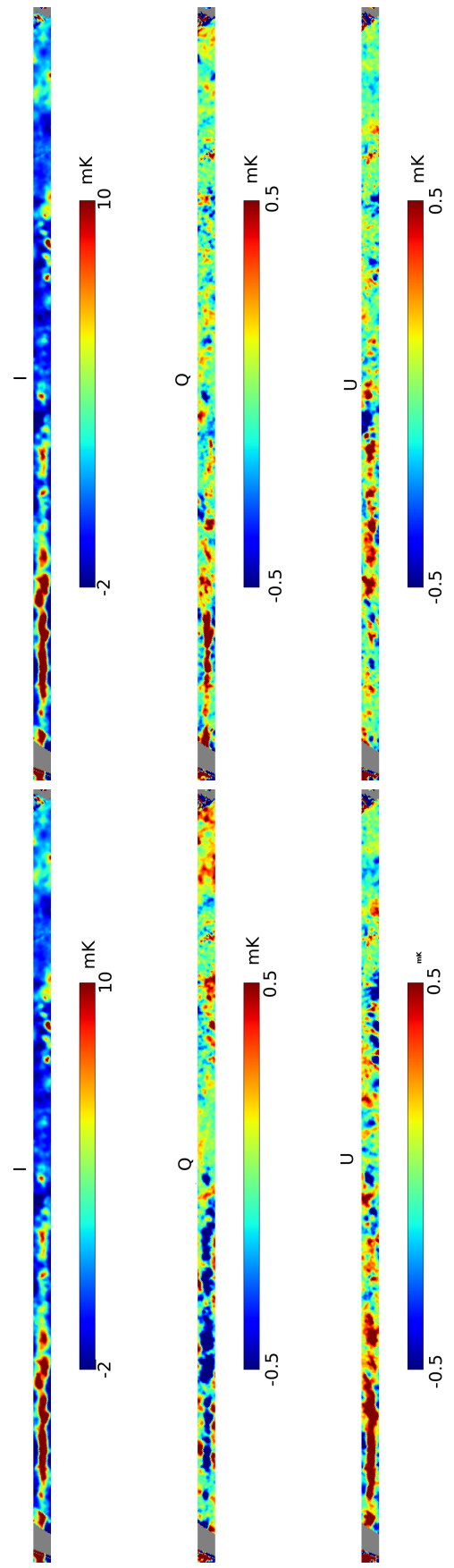
Figure 9.15: I, Q and U Galaxy maps in the sky frame for LD2013 250 GHz bolometers, before (*left*) and after (*right*) removal of the excess polarization. The maps are generated for NSIDE 512 and smoothed to 16′.
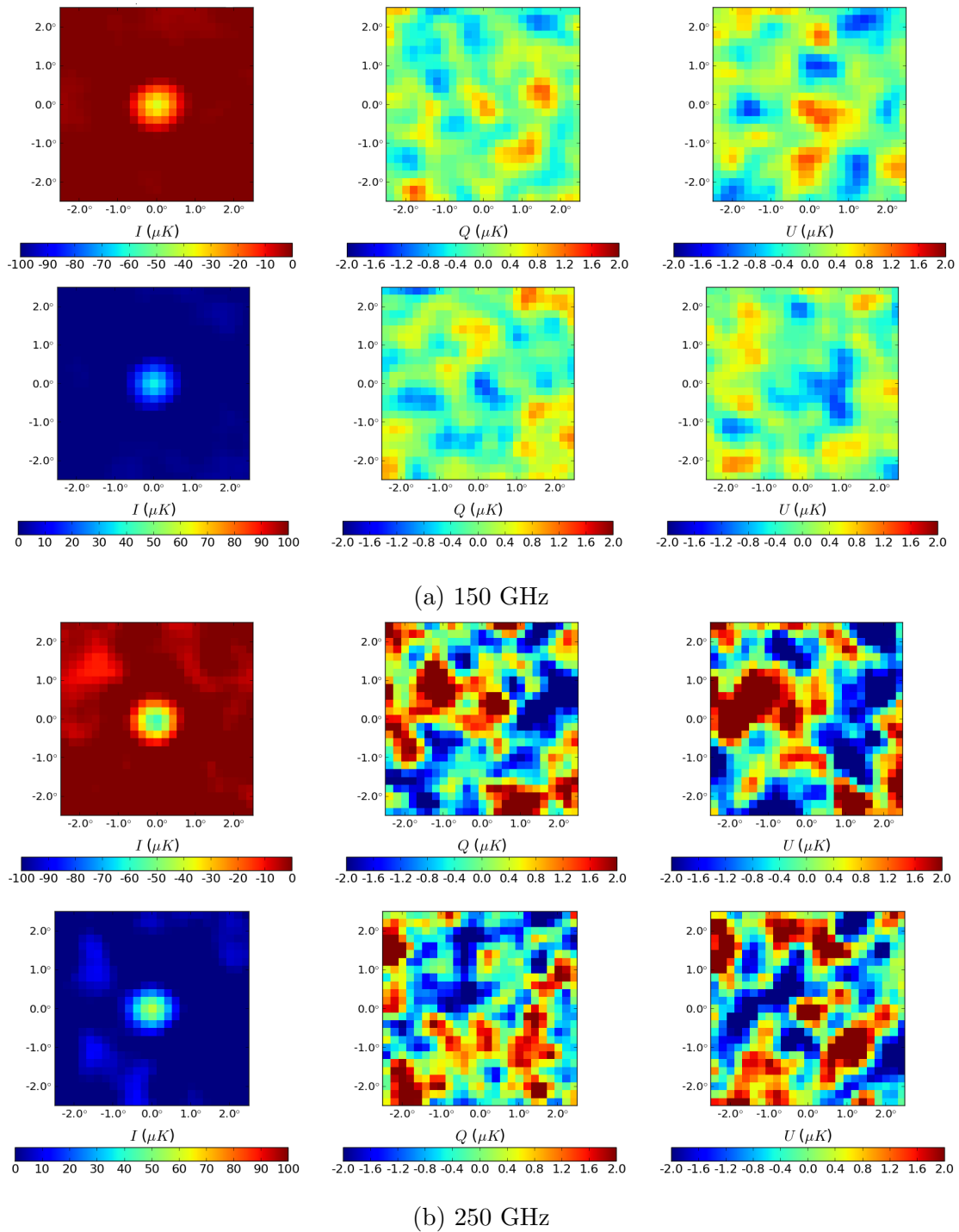
Figure 9.16: LD2013 stacked CMB cold and hot spots in the instrument frame for 150 (a) and 250 (b) GHz bolometers, after removal of the excess polarization. These maps should be compared to their equivalent before excess polarization removal, shown in Figures 9.3 and 9.4.
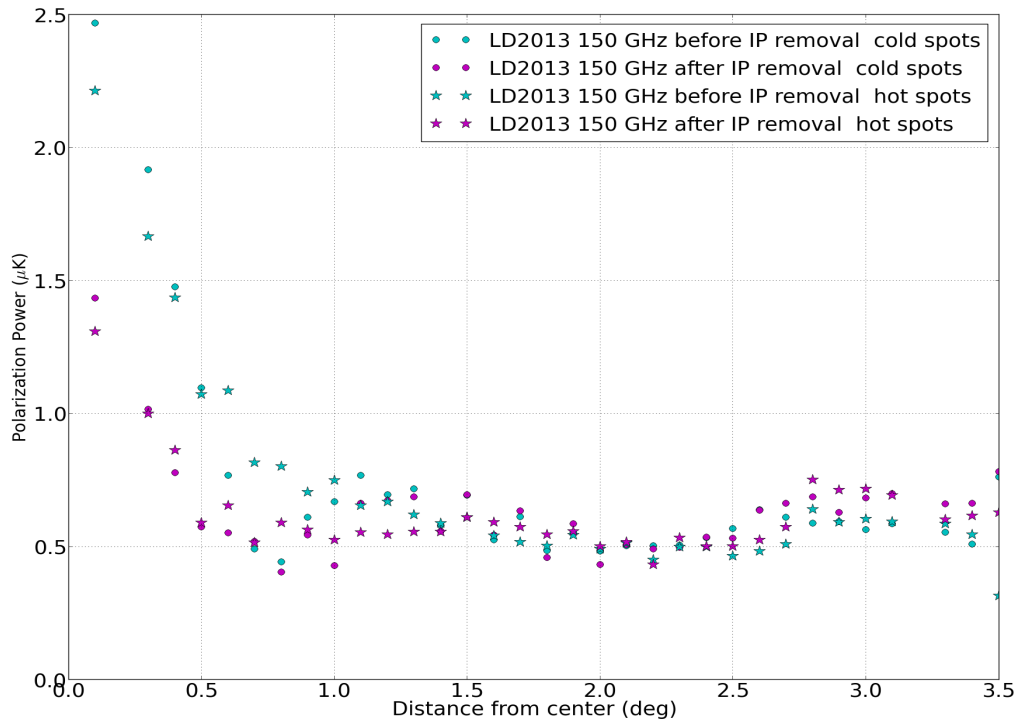
(a) 150 GHz
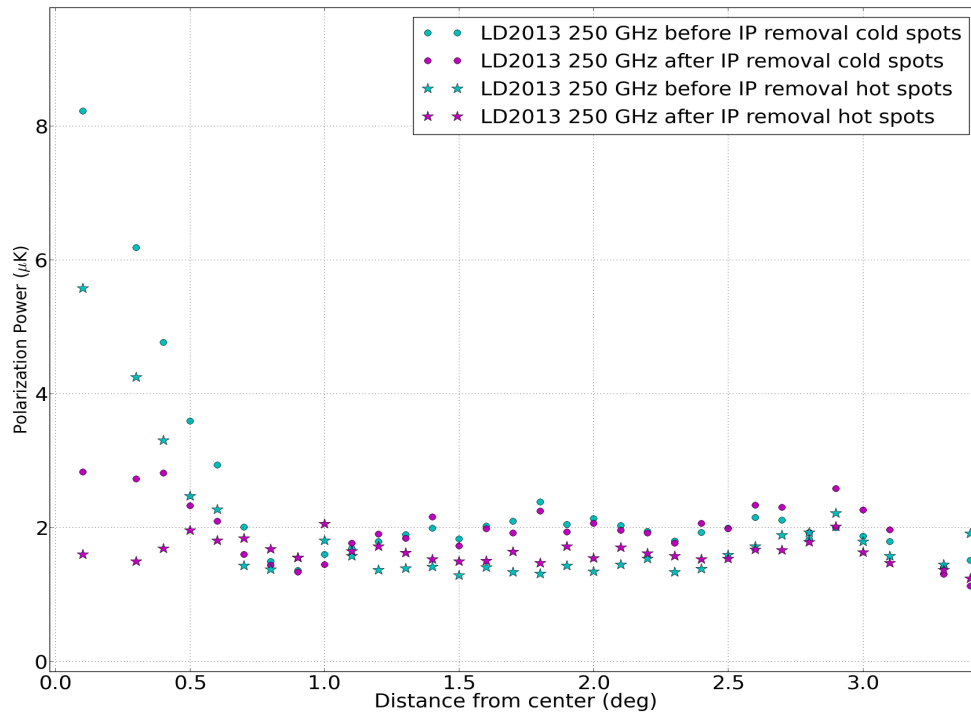
(b) 250 GHz

Figure 9.17: Polarization power in the stacked maps, as a function of the distance from the center of the stacked map. Results for 150 GHz (a) and 250 GHz (b) are presented. The cyan points represent maps generated without any IP removal. The magenta points represent maps generated after IP removal. Cold and hot spots are plotted separately using circles and stars, respectively.

157

Bibliography

[1] P.A.R. Ade et al. Joint Analysis of BICEP2/*KeckArray* and *Planck* Data. *Phys.Rev.Lett.*, 114:101301, 2015.

[2] Hubble E. A relation between distance and radial velocity among extra-galactic nebulae. *Proceedings of the National Academy of Sciences*, 1929.

[3] W. L. Freedman, B. F. Madore, B. K. Gibson, L. Ferrarese, D. D. Kelson, S. Sakai, J. R. Mould, R. C. Kennicutt Jr., H. C. Ford, J. A. Graham, J. P. Huchra, S. M. G. Hughes, G. D. Illingworth, L. M. Macri, and P. B. Stetson. Final results from the hubble space telescope key project to measure the hubble constant. *Ap. J.*, 553:47, 2000. astro-ph/0012376.

[4] C. L. Bennett, A. J. Banday, K. M. Gorski, G. Hinshaw, P. Jackson, P. Keegstra, A. Kogut, G. F. Smoot, D. T. Wilkinson, and E. L. Wright. Four-year cobe dmr cosmic microwave background observations: Maps and basic results. *Ap. J. Lett.*, 464:L1, June 1996.

[5] S. Perlmutter, G. Aldering, G. Goldhaber, R. A. Knop, P. Nugent, P. G. Castro, S. Deustua, S. Fabbro, A. Goobar, D. E. Groom, I. M. Hook, A. G. Kim, M. Y. Kim, J. C. Lee, N. J. Nunes, R. Pain, C. R. Pennypacker, R. Quimby, C. Lidman, R. S. Ellis, M. Irwin, R. G. McMahon, P. Ruiz-Lapuente, N. Walton, B. Schaefer, B. J. Boyle, A. V. Filippenko, T. Matheson, A. S. Fruchter, N. Panagia, H. J. M. Newberg, W. J. Couch,

and The Supernova Cosmology Project. Measurements of omega and lambda from 42 high-redshift supernovae. *Ap. J.*, 517:565–586, June 1999.

[6] B. P. Schmidt, N. B. Suntzeff, M. M. Phillips, R. A. Schommer, A. Clocchiatti, R. P. Kirshner, P. Garnavich, P. Challis, B. Leibundgut, J. Spyromilio, A. G. Riess, A. V. Filippenko, M. Hamuy, R. C. Smith, C. Hogan, C. Stubbs, A. Diercks, D. Reiss, R. Gilliland, J. Tonry, J. Eeacute; Maza, A. Dressler, J. Walsh, and R. Ciardullo. The high-z supernova search: Measuring cosmic deceleration and global curvature of the universe using type ia supernovae. *Ap. J.*, 507:46, November 1998.

[7] Planck Collaboration et al. Planck 2015 results. XI. CMB power spectra, likelihoods, and robustness of parameters. 2015.

[8] Will J. Percival et al. Baryon acoustic oscillations in the sloan digital sky survey data release 7 galaxy sample. *Mon.Not.Roy.Astron.Soc.*, 401:2148–2168, 2010.

[9] Erik Aver, Keith A. Olive, and Evan D. Skillman. An mcmc determination of the primordial helium abundance. *Journal of Cosmology and Astroparticle Physics*, 2012(04):004, 2012.

[10] D. J. Fixsen, E. S. Cheng, J. M. Gales, J. C. Mather, R. A. Shafer, and E. L. Wright. The Cosmic Microwave Background Spectrum from the Full COBE FIRAS Data Set. *Ap. J.*, 473:576–587, December 1996.

[11] E. Komatsu, K. M. Smith, J. Dunkley, C. L. Bennett, B. Gold, G. Hinshaw, N. Jarosik, D. Larson, M. R. Nolta, L. Page, D. N. Spergel, M. Halpern, R. S. Hill, A. Kogut, M. Limon, S. S. Meyer, N. Odegard, G. S. Tucker, J. L. Weiland, E. Wollack, and E. L. Wright. Seven-year Wilkinson Microwave Anisotropy Probe (WMAP) Observations: Cosmological Interpretation. *Ap. J. Suppl.*, 192:18–+, February 2011.

[12] R. K. Sachs and A. M. Wolfe. Perturbations of a Cosmological Model and Angular Variations of the Microwave Background. *Ap. J.*, 147:73, January 1967.

[13] Planck Collaboration, P. A. R. Ade, N. Aghanim, C. Armitage-Caplan, M. Arnaud, M. Ashdown, F. Atrio-Barandela, J. Aumont, C. Baccigalupi, A. J. Banday, and et al. Planck 2013 results. XV. CMB power spectra and likelihood. *Astron. Astrophys.*, 571:A15, November 2014.

[14] K. Ganga, E. Cheng, S. Meyer, and L. Page. Cross-correlation between the 170 GHz survey map and the COBE differential microwave radiometer first-year maps. *Ap. J. Lett.*, 410:L57–L60, June 1993.

[15] B. Gold, N. Odegard, J. L. Weiland, R. S. Hill, A. Kogut, C. L. Bennett, G. Hinshaw, X. Chen, J. Dunkley, M. Halpern, N. Jarosik, E. Komatsu, D. Larson, M. Limon, S. S. Meyer, M. R. Nolta, L. Page, K. M. Smith, D. N. Spergel, G. S. Tucker, E. Wollack, and E. L. Wright. Seven-year Wilkinson Microwave Anisotropy Probe (WMAP) Observations: Galactic Foreground Emission. *Ap. J. Suppl.*, 192:15–+, February 2011.

[16] D. Baumann, M. G. Jackson, P. Adshead, A. Amblard, A. Ashoorioon, N. Bartolo, R. Bean, M. Beltrán, F. de Bernardis, S. Bird, X. Chen, D. J. H. Chung, L. Colombo, A. Cooray, P. Creminelli, S. Dodelson, J. Dunkley, C. Dvorkin, R. Easther, F. Finelli, R. Flauger, M. P. Hertzberg, K. Jones-Smith, S. Kachru, K. Kadota, J. Khoury, W. H. Kinney, E. Komatsu, L. M. Krauss, J. Lesgourgues, A. Liddle, M. Liguori, E. Lim, A. Linde, S. Matarrese, H. Mathur, L. McAllister, A. Melchiorri, A. Nicolis, L. Pagano, H. V. Peiris, M. Peloso, L. Pogosian, E. Pierpaoli, A. Riotto, U. Seljak, L. Senatore, S. Shandera, E. Silverstein, T. Smith, P. Vaudrevange, L. Verde, B. Wandelt, D. Wands, S. Watson, M. Wyman, A. Yadav, W. Valkenburg, and M. Zaldarriaga. Probing Inflation with CMB Polarization. In S. Dodelson, D. Baumann, A. Cooray, J. Dunkley, A. Fraisse, M. G. Jackson, A. Kogut, L. Krauss, M. Zaldarriaga, and K. Smith, editors, *American Institute of Physics Conference Series*, volume 1141 of *American Institute of Physics Conference Series*, pages 10–120, June 2009.

[17] Planck Collaboration, P. A. R. Ade, N. Aghanim, C. Armitage-Caplan, M. Arnaud, M. Ashdown, F. Atrio-Barandela, J. Aumont, C. Baccigalupi, A. J. Banday, and et al. Planck 2013 results. XVI. Cosmological parameters. *ArXiv e-prints*, March 2013.

[18] W Hu and M. White. A cmb polarization primer. *New Astronomy*, 2:323–344, 1997.

[19] J. M. Kovac, E. M. Leitch, C. Pryke, J. E. Carlstrom, N. W. Halverson, and W. L. Holzapfel. Detection of polarization in the cosmic microwave background using DASI. *Nature*, 420:772, December 2002. astro-ph/0209478.

[20] H. C. Chiang, P. A. R. Ade, D. Barkats, J. O. Battle, E. M. Bierman, J. J. Bock, C. D. Dowell, L. Duband, E. F. Hivon, W. L. Holzapfel, V. V. Hristov, W. C. Jones, B. G. Keating, J. M. Kovac, C. L. Kuo, A. E. Lange, E. M. Leitch, P. V. Mason, T. Matsumura, H. T. Nguyen, N. Ponthieu, C. Pryke, S. Richter, G. Rocha, C. Sheehy, Y. D. Takahashi, J. E. Tolan, and K. W. Yoon. Measurement of Cosmic Microwave Background Polarization Power Spectra from Two Years of BICEP Data. *Ap. J.*, 711:1123–1140, March 2010.

[21] M. L. Brown, P. Ade, J. Bock, M. Bowden, G. Cahill, P. G. Castro, S. Church, T. Culverhouse, R. B. Friedman, K. Ganga, W. K. Gear, S. Gupta, J. Hinderks, J. Kovac, A. E. Lange, E. Leitch, S. J. Melhuish, Y. Memari, J. A. Murphy, A. Orlando, C. O'Sullivan, L. Piccirillo, C. Pryke, N. Rajguru, B. Rusholme, R. Schwarz, A. N. Taylor, K. L. Thompson, A. H. Turner, E. Y. S. Wu, M. Zemcov, and The QUa D collaboration. Improved Measurements of the Temperature and Polarization of the Cosmic Microwave Background from QUaD. *Ap. J.*, 705:978–999, November 2009.

[22] C. Bischoff, L. Hyatt, J. J. McMahon, G. W. Nixon, D. Samtleben, K. M. Smith, K. Vanderlinde, D. Barkats, P. Farese, T. Gaier, J. O. Gundersen, M. M. Hedman, S. T. Staggs, B. Winstein, and CAPMAP Collaboration. New Measurements of Fine-

Scale CMB Polarization Power Spectra from CAPMAP at Both 40 and 90 GHz. *Ap. J.*, 684:771–789, September 2008.

[23] QUIET Collaboration, D. Araujo, C. Bischoff, A. Brizius, I. Buder, Y. Chinone, K. Cleary, R. N. Dumoulin, A. Kusaka, R. Monsalve, S. K. Næss, L. B. Newburgh, R. Reeves, I. K. Wehus, J. T. L. Zwart, L. Bronfman, R. Bustos, S. E. Church, C. Dickinson, H. K. Eriksen, T. Gaier, J. O. Gundersen, M. Hasegawa, M. Hazumi, K. M. Huffenberger, K. Ishidoshiro, M. E. Jones, P. Kangaslahti, D. J. Kapner, D. Kubik, C. R. Lawrence, M. Limon, J. J. McMahon, A. D. Miller, M. Nagai, H. Nguyen, G. Nixon, T. J. Pearson, L. Piccirillo, S. J. E. Radford, A. C. S. Readhead, J. L. Richards, D. Samtleben, M. Seiffert, M. C. Shepherd, K. M. Smith, S. T. Staggs, O. Tajima, K. L. Thompson, K. Vanderlinde, and R. Williamson. Second Season QUIET Observations: Measurements of the Cosmic Microwave Background Polarization Power Spectrum at 95 GHz. *Ap. J.*, 760:145, December 2012.

[24] J. L. Sievers, C. Achermann, J. R. Bond, L. Bronfman, R. Bustos, C. R. Contaldi, C. Dickinson, P. G. Ferreira, M. E. Jones, A. M. Lewis, B. S. Mason, J. May, S. T. Myers, N. Oyarce, S. Padin, T. J. Pearson, M. Pospieszalski, A. C. S. Readhead, R. Reeves, A. C. Taylor, and S. Torres. Implications of the Cosmic Background Imager Polarization Data. *Ap. J.*, 660:976–987, May 2007.

[25] T. E. Montroy, P. A. R. Ade, J. J. Bock, J. R. Bond, J. Borrill, A. Boscaleri, P. Cabella, C. R. Contaldi, B. P. Crill, P. de Bernardis, G. De Gasperis, A. de Oliveira-Costa, G. De Troia, G. di Stefano, E. Hivon, A. H. Jaffe, T. S. Kisner, W. C. Jones, A. E. Lange, S. Masi, P. D. Mauskopf, C. J. MacTavish, A. Melchiorri, P. Natoli, C. B. Netterfield, E. Pascale, F. Piacentini, D. Pogosyan, G. Polenta, S. Prunet, S. Ricciardi, G. Romeo, J. E. Ruhl, P. Santini, M. Tegmark, M. Veneziani, and N. Vittorio. A Measurement of the CMB <EE>Spectrum from the 2003 Flight of BOOMERANG. *Ap. J.*, 647:813–822, August 2006.

[26] M. Lueker, C. L. Reichardt, K. K. Schaffer, O. Zahn, P. A. R. Ade, K. A. Aird, B. A. Benson, L. E. Bleem, J. E. Carlstrom, C. L. Chang, H.-M. Cho, T. M. Crawford, A. T. Crites, T. de Haan, M. A. Dobbs, E. M. George, N. R. Hall, N. W. Halverson, G. P. Holder, W. L. Holzapfel, J. D. Hrubes, M. Joy, R. Keisler, L. Knox, A. T. Lee, E. M. Leitch, J. J. McMahon, J. Mehl, S. S. Meyer, J. J. Mohr, T. E. Montroy, S. Padin, T. Plagge, C. Pryke, J. E. Ruhl, L. Shaw, E. Shirokoff, H. G. Spieler, B. Stalder, Z. Staniszewski, A. A. Stark, K. Vanderlinde, J. D. Vieira, and R. Williamson. Measurements of Secondary Cosmic Microwave Background Anisotropies with the South Pole Telescope. *Ap. J.*, 719:1045–1066, August 2010.

[27] J. W. Fowler, V. Acquaviva, P. A. R. Ade, P. Aguirre, M. Amiri, J. W. Appel, L. F. Barrientos, E. S. Battistelli, J. R. Bond, B. Brown, B. Burger, J. Chervenak, S. Das, M. J. Devlin, S. R. Dicker, W. B. Doriese, J. Dunkley, R. Dünner, T. Essinger-Hileman, R. P. Fisher, A. Hajian, M. Halpern, M. Hasselfield, C. Hernández-Monteagudo, G. C. Hilton, M. Hilton, A. D. Hincks, R. Hlozek, K. M. Huffenberger, D. H. Hughes, J. P. Hughes, L. Infante, K. D. Irwin, R. Jimenez, J. B. Juin, M. Kaul, J. Klein, A. Kosowsky, J. M. Lau, M. Limon, Y.-T. Lin, R. H. Lupton, T. A. Marriage, D. Marsden, K. Martocci, P. Mauskopf, F. Menanteau, K. Moodley, H. Moseley, C. B. Netterfield, M. D. Niemack, M. R. Nolta, L. A. Page, L. Parker, B. Partridge, H. Quintana, B. Reid, N. Sehgal, J. Sievers, D. N. Spergel, S. T. Staggs, D. S. Swetz, E. R. Switzer, R. Thornton, H. Trac, C. Tucker, L. Verde, R. Warne, G. Wilson, E. Wollack, and Y. Zhao. The Atacama Cosmology Telescope: A Measurement of the 600 <ell <8000 Cosmic Microwave Background Power Spectrum at 148 GHz. *Ap. J.*, 722:1148–1161, October 2010.

[28] D. Hanson, S. Hoover, A. Crites, P. A. R. Ade, K. A. Aird, J. E. Austermann, J. A. Beall, A. N. Bender, B. A. Benson, L. E. Bleem, J. J. Bock, J. E. Carlstrom, C. L. Chang, H. C. Chiang, H.-M. Cho, A. Conley, T. M. Crawford, T. de Haan, M. A. Dobbs, W. Everett, J. Gallicchio, J. Gao, E. M. George, N. W. Halverson, N. Harrington,

J. W. Henning, G. C. Hilton, G. P. Holder, W. L. Holzapfel, J. D. Hrubes, N. Huang, J. Hubmayr, K. D. Irwin, R. Keisler, L. Knox, A. T. Lee, E. Leitch, D. Li, C. Liang, D. Luong-Van, G. Marsden, J. J. McMahon, J. Mehl, S. S. Meyer, L. Mocanu, T. E. Montroy, T. Natoli, J. P. Nibarger, V. Novosad, S. Padin, C. Pryke, C. L. Reichardt, J. E. Ruhl, B. R. Saliwanchik, J. T. Sayre, K. K. Schaffer, B. Schulz, G. Smecher, A. A. Stark, K. T. Story, C. Tucker, K. Vanderlinde, J. D. Vieira, M. P. Viero, G. Wang, V. Yefremenko, O. Zahn, and M. Zemcov. Detection of B-Mode Polarization in the Cosmic Microwave Background with Data from the South Pole Telescope. *Physical Review Letters*, 111(14):141301, October 2013.

[29] Sudeep Das, Thibaut Louis, Michael R. Nolta, Graeme E. Addison, Elia S. Battistelli, J Richard Bond, Erminia Calabrese, Devin Crichton, Mark J. Devlin, Simon Dicker, Joanna Dunkley, Rolando Dünner, Joseph W. Fowler, Megan Gralla, Amir Hajian, Mark Halpern, Matthew Hasselfield, Matt Hilton, Adam D. Hincks, Renée Hlozek, Kevin M. Huffenberger, John P. Hughes, Kent D. Irwin, Arthur Kosowsky, Robert H. Lupton, Tobias A. Marriage, Danica Marsden, Felipe Menanteau, Kavilan Moodley, Michael D. Niemack, Lyman A. Page, Bruce Partridge, Erik D. Reese, Benjamin L. Schmitt, Neelima Sehgal, Blake D. Sherwin, Jonathan L. Sievers, David N. Spergel, Suzanne T. Staggs, Daniel S. Swetz, Eric R. Switzer, Robert Thornton, Hy Trac, and Ed Wollack. The atacama cosmology telescope: temperature and gravitational lensing power spectrum measurements from three seasons of data. *Journal of Cosmology and Astroparticle Physics*, 2014(04):014, 2014.

[30] The Polarbear Collaboration: P. A. R. Ade, Y. Akiba, A. E. Anthony, K. Arnold, M. Atlas, D. Barron, D. Boettger, J. Borrill, S. Chapman, Y. Chinone, M. Dobbs, T. Elleflot, J. Errard, G. Fabbian, C. Feng, D. Flanigan, A. Gilbert, W. Grainger, N. W. Halverson, M. Hasegawa, K. Hattori, M. Hazumi, W. L. Holzapfel, Y. Hori, J. Howard, P. Hyland, Y. Inoue, G. C. Jaehnig, A. H. Jaffe, B. Keating, Z. Kermish,

R. Keskitalo, T. Kisner, M. Le Jeune, A. T. Lee, E. M. Leitch, E. Linder, M. Lungu, F. Matsuda, T. Matsumura, X. Meng, N. J. Miller, H. Morii, S. Moyerman, M. J. Myers, M. Navaroli, H. Nishino, A. Orlando, H. Paar, J. Peloton, D. Poletti, E. Quealy, G. Rebeiz, C. L. Reichardt, P. L. Richards, C. Ross, I. Schanning, D. E. Schenck, B. D. Sherwin, A. Shimizu, C. Shimmin, M. Shimon, P. Siritanasak, G. Smecher, H. Spieler, N. Stebor, B. Steinbach, R. Stompor, A. Suzuki, S. Takakura, T. Tomaru, B. Wilson, A. Yadav, and O. Zahn. A measurement of the cosmic microwave background b-mode polarization power spectrum at sub-degree scales with polarbear. *The Astrophysical Journal*, 794(2):171, 2014.

[31] BICEP2 Collaboration, P. A. R Ade, R. W. Aikin, D. Barkats, S. J. Benton, C. A. Bischoff, J. J. Bock, J. A. Brevik, I. Buder, E. Bullock, C. D. Dowell, L. Duband, J. P. Filippini, S. Fliescher, S. R. Golwala, M. Halpern, M. Hasselfield, S. R. Hildebrandt, G. C. Hilton, V. V. Hristov, K. D. Irwin, K. S. Karkare, J. P. Kaufman, B. G. Keating, S. A. Kernasovskiy, J. M. Kovac, C. L. Kuo, E. M. Leitch, M. Lueker, P. Mason, C. B. Netterfield, H. T. Nguyen, R. O'Brient, R. W. Ogburn, IV, A. Orlando, C. Pryke, C. D. Reintsema, S. Richter, R. Schwarz, C. D. Sheehy, Z. K. Staniszewski, R. V. Sudiwala, G. P. Teply, J. E. Tolan, A. D. Turner, A. G. Vieregg, C. L. Wong, and K. W. Yoon. BICEP2 I: Detection Of B-mode Polarization at Degree Angular Scales. *ArXiv e-prints*, March 2014.

[32] http://polar-array.stanford.edu/graphics/Bmode2016.png.

[33] Britt Reichborn-Kjennerud et al. EBEX: A balloon-borne CMB polarization experiment. *Millimeter, Submillimeter, and Far-Infrared Detectors and Instrumentation for Astronomy V*, 7741, 2010.

[34] B. Reichborn-Kjennerud. *Building and Flying the E and B Experiment to Measure the Polarization of the Cosmic Microwave Background*. PhD thesis, Columbia University, 2010.

[35] E. Pascale et al. The Balloon-borne Large Aperture Submillimeter Telescope: BLAST. *ApJ*, 2008.

[36] S. Hillbrand. *The E and B EXperiment: A balloon-borne cosmic microwave background anisotropy probe.* PhD thesis, Columbia University, 2014.

[37] M. Milligan. *The E and B EXperiment: implementation and analysis of the 2009 engineering flight.* PhD thesis, University of Minnesota, 2011.

[38] K. Zylic. *Calibration and Design of the E and B EXperiment (EBEX) Cryogenic Receiver.* PhD thesis, University of Minnesota, 2014.

[39] J. Klein. *Design, implementation, and calibration of physics Half-Wave Plate polarimetry for the E and B Experiment .* PhD thesis, University of Minnesota, 2014.

[40] F. Aubin. *Detector readout electronics for EBEX : a balloon-borne cosmic microwave background polarimeter.* PhD thesis, McGill University, 2012.

[41] K. McDermid. *Development and Performance of the Detectors and Readout of the EBEX Balloon-Borne CMB Polarimeter.* PhD thesis, McGill University, 2014.

[42] D. Chapman et al. STARS: A software application for the EBEX autonomous daytime star cameras. *Proc. of SPIE conference*, 2014.

[43] D. Chapman et al. Star Camera System and New Software for Autonomous and Robust Operation in Long Duration Flights. *Proc. of IEEE Aerospace Conference*, 2015.

[44] Rudolph Emil Kalman. A new approach to linear filtering and prediction problems. *Transactions of the ASME–Journal of Basic Engineering*, 82(series d):35–45, 1960.

[45] K. M. Górski, E. Hivon, A. J. Banday, B. D. Wandelt, F. K. Hansen, M. Reinecke, and M. Bartelmann. HEALPix: A Framework for High-Resolution Discretization and Fast Analysis of Data Distributed on the Sphere. *Ap. J.*, 622:759–771, April 2005.

[46] M. Rex. *The Balloon-borne Large Aperture Submillimeter Telescope (BLAST)*. PhD thesis, university of pennsylvania, 2007.

[47] IEEE Standard Specification Format Guide and Test Procedure for Single-Axis Interferometric Fiber Optic Gyros. *IEEE Std. 952-1997*, 1998.

[48] Eric A. Wan and Rudolph van der Merwe. The unscented kalman filter for nonlinear estimation. In *Proceedings of Symposium 2000 on Adaptive Systems for Signal Processing, Communication and Control (AS-SPCC)*, Lake Louise, Alberta, Canada, October 2000. IEEE.

[49] James R. Wertz. *Spacecraft Attitude Determination and Control*. D. Reidel, 1980.

[50] Simon J. Julier, Jeffrey, and K. Uhlmann. Unscented filtering and nonlinear estimation. In *Proceedings of the IEEE*, pages 401–422, 2004.

[51] D. Chapman. *EBEX: A Balloon-Borne Telescope for Measuring Cosmic Microwave Background Polarization*. PhD thesis, Columbia University, 2015.

[52] J. et al. Didier. A High-resolution Pointing System for Fast Scanning Platforms: the EBEX Example. *2015 IEEE Aerospace Conference*, 2015.

[53] W. Hu, M. M. Hedman, and M. Zaldarriaga. Benchmark parameters for CMB polarization experiments. *Phys. Rev. D.*, 67:043004–+, February 2003. astro-ph/0210096.

[54] J. Didier. Pointing error of off-axis detectors induced by uncertainties in roll. *Unpublished internal memorandum*, April 2012.

[55] C. Geach. Searching for a consistent overall polarization calibration. *Unpublished internal memorandum*, June 2015.

[56] D. V. Wiebe, C. B. Netterfield, and T. S. Kisner. GetData: A filesystem-based, column-oriented database format for time-ordered binary data. Astrophysics Source Code Library, December 2015.

[57] F. Aubin and et al. Temperature Calibration of the E and B Experiment. *WSPC Proceedings*, 2016.

[58] Planck Collaboration et al. Planck 2015 Results. X. Diffuse Component Separation: Foreground maps. 2015.

[59] The EBEX Collaboration. The ebex balloon borne experiment - detectors and readout. *In preparation*, 2016.

[60] M. Zaldarriaga. Cross pol: simple estimates. *Unpublished internal memorandum*, September 2006.

[61] M. Kamionkowski, A. Kosowsky, and A. Stebbins. Statistics of Cosmic Microwave Background Polarization. *Phys. Rev. D.*, 55:7368–7388, June 1997.

[62] J. Didier. Method to measure non-linearity using the template. *Unpublished internal memorandum*, 2016.

Appendix A

Transforming the Attitude Requirements from Map Domain to Error on a Single Azimuth Throw

The requirements for the attitude reconstruction on EBEX are set in the map domain. The error on the mean of all attitudes within a pixel must be smaller than $\sim$10". We want to map this average error in a pixel to an error on the RMS of a throw. The RMS on a throw is defined as the root mean square of the difference between estimated attitude and true attitude for all samples within a throw:

$$RMS^2 = \frac{1}{M} \sum_{t=0}^{t=M} \sigma_{\theta_t}^2 \tag{A.1}$$

where M is the number of samples in the throw and σ_{θ_t} is the error on the attitude at time t. We now consider the sum of the attitudes in a pixel. If a pixel is visited P times from independent scans, the variance of this sum σ_{sum}^2 is:

$$\sigma_{sum}^2 = \sum_{i=1}^{i=P} \sigma_{\theta_i}^2 \tag{A.2}$$

where we made the reasonable assumption that the errors in between scans are uncorrelated. σ_{θ_i} is the error on the attitude the $i - th$ time the pixel is hit. Each time the pixel is hit, it is from a random position in the throw, and so we can compare the previous equation to the RMS Equation A.1 to deduce that σ_{sum} is in fact related to the RMS by $\sigma_{sum} = \sqrt{P} \cdot RMS$. Finally we compute the error on the mean of all attitudes in the pixel, which we call σ_P^2:

$$\sigma_P = \frac{\sigma_{sum}}{P} \tag{A.3}$$

$$= \frac{\sqrt{P} RMS}{P} \tag{A.4}$$

$$= \frac{RMS}{\sqrt{P}} \tag{A.5}$$

The next task is to estimate P, the number of hits per pixel coming from independent scans. The LD flight hit map is shown in Figure 4.2b for pixels of size $\sim$6.9' (nside=516 in the HEALPix pixelization scheme). For pixels of size $\sim$1.7' (nside=2048), we can extrapolate from this figure that most pixels have between 500 and 7000 hits, with 1600 hits on average. We do not want to count hits within a given throw because consecutive attitude errors are extremely correlated and do not average down. Because of our scan patterns, we assume that a pixel is either hit consecutively within a single throw, or from different revisits from independent scans. Let's estimate the number of consecutive hits of a pixel within a throw. The median velocity of the telescope is 0.1 $^\circ$s^{-1}, and so it takes $\sim$0.28 seconds to traverse the 1.7' pixel. The detectors are sampled at 191 Hz, and so they hit the pixel 53 times during the 0.28 seconds. So we estimate P by making the approximation that all pixels have the same number of hits (1600) and then calculate that the number of hits with uncorrelated attitude errors is P = 1600/53 $\sim$30. Since for EBEX the requirements are that $\sigma_P \sim$10", the requirements on the RMS over a throw are RMS = $\sigma_P \sqrt{P} \sim$54".

Appendix B

Estimating the error on a single throw from gyroscope noise

To assess the quality of the attitude reconstruction, we use the RMS error over a throw. It is interesting to estimate what is the expected RMS on a throw given a simple scenario with gyroscope rate white noise only. Let us first consider the one dimension case, where the gyroscope noise is white and the gyroscope is perfectly aligned with the direction of motion. The gyroscope measures a rate ω, and the equation of motion is:

$$\dot{\theta} = \omega \Delta t \tag{B.1}$$

The variance on the integrated angle from a single time step is :

$$\sigma_{\theta_{k+1}}^2 = \sigma_{\theta_k}^2 + \sigma_\omega^2 \Delta t^2 \tag{B.2}$$

$$= \sigma_{\theta_k}^2 + \sigma_{\theta_0}^2 \tag{B.3}$$

The gyroscopes have a rate white noise of $\sigma_\omega = 40.0"/s$, and the time step is ~ 0.01 seconds, so the uncertainty on the angle from a single step of integration is $\sigma_{\theta_0} = 0.4"$. N time steps

after a star camera, the integrated attitude in a given time direction has a variance:

$$\sigma_{\theta_N}^2 = N\sigma_{\theta_0}^2 + \sigma_{sc}^2 \tag{B.4}$$

where σ_{sc} is the uncertainty on the star camera solution. At any point in the scan, the reconstruction is the weighted average of the forward and backward solutions. If M is the total number of samples between two star camera readings, the variance of the attitude at time step N is:

$$\frac{1}{\sigma_{\theta_N}^2} = \frac{1}{\sigma_{\theta_N}^{2forward}} + \frac{1}{\sigma_{\theta_{M-N}}^{2backrward}} \tag{B.5}$$

$$= \frac{1}{N\sigma_{\theta_0}^2 + \sigma_{sc}^2} + \frac{1}{(M-N)\sigma_{\theta_0}^2 + \sigma_{sc}^2} \tag{B.6}$$

$$= \frac{M\sigma_{\theta_0}^2 + 2\sigma_{sc}^2}{N(M-N)\sigma_{\theta_0}^4 + M\sigma_{\theta_0}^2\sigma_{sc}^2 + \sigma_{sc}^4} \tag{B.7}$$

The RMS on the throw can be expressed as the average of all the variances across the throw:

$$RMS = \sqrt{\frac{1}{M}\sum_{N=0}^{N=M}\sigma_{\theta_N}^2} \tag{B.8}$$

$$= \sqrt{\frac{1}{M}\sum_{N=0}^{N=M}\frac{N(M-N)\sigma_{\theta_0}^4 + M\sigma_{\theta_0}^2\sigma_{sc}^2 + \sigma_{sc}^4}{M\sigma_{\theta_0}^2 + 2\sigma_{sc}^2}} \tag{B.9}$$

$$= \sqrt{\frac{\frac{1}{6}M^2\sigma_{\theta_0}^4 + M\sigma_{\theta_0}^2\sigma_{sc}^2 + \sigma_{sc}^4}{M\sigma_{\theta_0}^2 + 2\sigma_{sc}^2}} \tag{B.10}$$

$$\sim \sigma_{\theta_0}\sqrt{\frac{M}{6}} \tag{B.11}$$

where we neglected the star camera errors σ_{sc} as they are small compared to gyroscope error. On a 40 second throw, M$\sim$4000, and thus RMS$\sim$11".

For the three dimension case, the Equation of motion B.1 needs to be replaced with

Equation 6.1, and the uncertainty of each integrated Euler angle after N steps now depends on the specific motion and values of all the angles across the throw. However with our typical velocities and uncertainties, the 1-D calculation is a good approximation.

Appendix C

Conventions for the R and O matrices

This appendix reviews how to compute the matrices R and O used to transform the star camera frame into the frame defined by the three gyroscopes. The matrices R and O are defined in Equation 6.6.

C.1 Orthogonalisation Matrix O

The matrix O depends on three "misalignment" angles δ, ϵ and η. It transforms the orthogonal gyroscope basis, that we name (O_1, O_2, O_3), into the true gyroscope frame defined by the three gyroscopes: $(1, 2, 3)$. The conventions used to defined the three misalignment angles are shown in Figure C.1.

In this diagram, one can see that δ, ϵ and η are small since the gyroscope form an almost orthogonal basis. Let the total rotation of the telescope be given by $\vec{\omega}$. Because (O_1, O_2, O_3) is an orthogonal basis, $\vec{\omega}$ can be expressed as:

$$\vec{\omega} = \omega_{1_O} \hat{o}_1 + \omega_{2_O} \hat{o}_2 + \omega_{3_O} \hat{o}_3 \tag{C.1}$$

We want to express $\vec{\omega}$ in the gyroscope basis: ω_1, ω_2 and ω_3 as a function of $\omega_{1_O}, \omega_{2_O}$ and ω_{3_O}. We have:
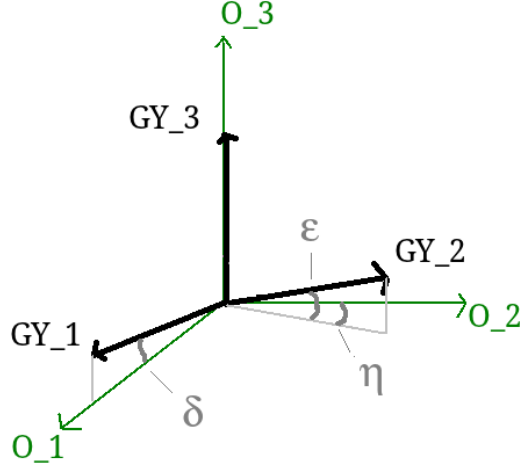
Figure C.1: Conventions used to define the three misalignment angles. Note that we can chose O_3 aligned with gyroscope 3 without any loss of generality.

$$
\begin{aligned}
\omega_1 &= \vec{\omega} \cdot \hat{g}_1 \\
&= \omega_{1_O} \hat{o}_1 \cdot \hat{g}_1 + \omega_{2_O} \hat{o}_2 \cdot \hat{g}_1 + \omega_{3_O} \hat{o}_3 \cdot \hat{g}_1
\end{aligned}
$$

$$(\text{C.2})$$

Doing the same with ω_2 and ω_3 we have:

$$
\begin{pmatrix} \omega_1 \\ \omega_2 \\ \omega_3 \end{pmatrix} = \begin{pmatrix} \hat{o}_1 \cdot \hat{g}_1 & \hat{o}_2 \cdot \hat{g}_1 & \hat{o}_3 \cdot \hat{g}_1 \\ \hat{o}_1 \cdot \hat{g}_2 & \hat{o}_2 \cdot \hat{g}_2 & \hat{o}_3 \cdot \hat{g}_2 \\ \hat{o}_1 \cdot \hat{g}_3 & \hat{o}_2 \cdot \hat{g}_3 & \hat{o}_3 \cdot \hat{g}_3 \end{pmatrix} \begin{pmatrix} \omega_{1_O} \\ \omega_{3_O} \\ \omega_{3_O} \end{pmatrix}
$$

$$(\text{C.3})$$

which can be re-written as:

$$
\begin{pmatrix} \omega_1 \\ \omega_2 \\ \omega_3 \end{pmatrix} = \begin{pmatrix} \cos(\delta) & 0 & \sin(\delta) \\ \cos(\epsilon)\sin(\eta) & \cos(\epsilon)\cos(\eta) & \sin(\epsilon) \\ 0 & 0 & 1 \end{pmatrix} \begin{pmatrix} \omega_{1_O} \\ \omega_{2_O} \\ \omega_{3_O} \end{pmatrix}
$$

$$(\text{C.4})$$

the inverse of which is:

$$
\begin{pmatrix} \omega_{1_O} \\ \omega_{2_O} \\ \omega_{3_O} \end{pmatrix} = \begin{pmatrix} \frac{1}{\cos(\delta)} & 0 & -\tan(\delta) \\ -\frac{\tan(\eta)}{\cos(\delta)} & \frac{1}{\cos(\epsilon)\cos(\eta)} & \frac{\cos(\epsilon)\sin(\delta)\sin(\eta)-\cos(\delta)\sin(\epsilon)}{\cos(\delta)\cos(\epsilon)\cos(\eta)} \\ 0 & 0 & 1 \end{pmatrix} \begin{pmatrix} \omega_1 \\ \omega_2 \\ \omega_3 \end{pmatrix} \quad \text{(C.5)}
$$

C.2 Rotation Matrix R

The rotation matrix R rotates the star camera frame (X_{sc}, Y_{sc}, Z_{sc}) in the orthogonalized gyroscope frame (O_1, O_2, O_3) defined in the previous section. We adopt the Tait-Bryan angle convention X-Y-Z, with α, β, γ the angles of the rotations around the axis X, Y and Z respectively. The conventions used to define the star camera frame are shown in Figure C.2. The resulting rotation matrix is:

$$
\begin{pmatrix} \omega_{1_o} \\ \omega_{2_o} \\ \omega_{3_o} \end{pmatrix} = \begin{pmatrix} c_\gamma & s_\gamma & 0 \\ -s_\gamma & c_\gamma & 0 \\ 0 & 0 & 1 \end{pmatrix} \begin{pmatrix} c_\beta & 0 & -s_\beta \\ 0 & 1 & 0 \\ s_\beta & 0 & c_\beta \end{pmatrix} \begin{pmatrix} 1 & 0 & 0 \\ 0 & c_\alpha & -s_\alpha \\ 0 & s_\alpha & c_\alpha \end{pmatrix} \begin{pmatrix} \omega_{X_{sc}} \\ \omega_{Y_{sc}} \\ \omega_{Z_{sc}} \end{pmatrix} \quad \text{(C.6)}
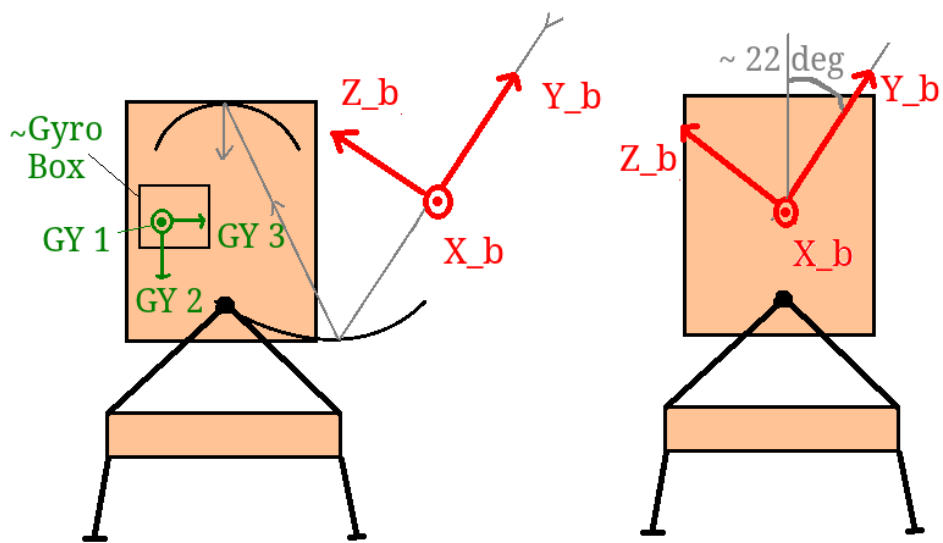$$

Figure C.2: Conventions for the star camera body frame. Note that the star camera is closely aligned with the microwave beam.